Graphene with Platinum Nanoparticles for Neural Recording and Stimulation

Samantha June Rice
Master of Science in BioMedical Engineering
Delft University of Technology
January 2023

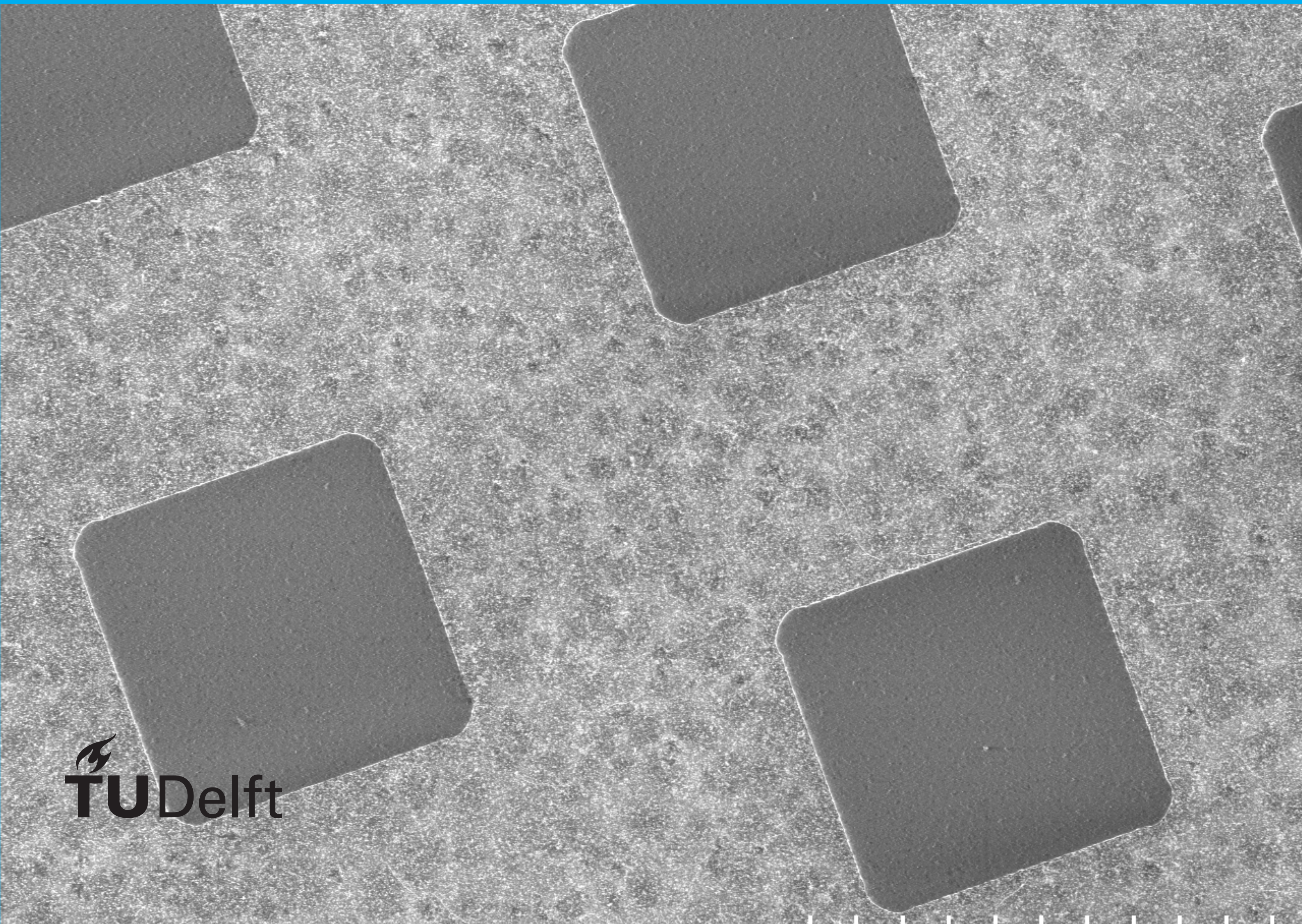

Graphene with Platinum Nanoparticles

for

Neural Recording and Stimulation

by

Samantha June Rice

to obtain the degree of Master of Science
at the Delft University of Technology,
to be defended publicly on Friday January 13, 2023 at 10:30 AM.

Student number:	5302242	
Project duration:	November 2021 – January 2023	
Thesis committee:	Dr. ir. S. Vollebregt,	TU Delft, supervisor
	Dr. V. Giagka,	TU Delft, supervisor
	N. Bakhshaee Babaroud,	TU Delft, supervisor
	Dr. J. G. Buijnsters,	TU Delft

This thesis is confidential and cannot be made public until January 13, 2024.

Abstract

Numerous advancements have been made in transparent electrode technologies that can complement optogenetics and imaging modalities. However, several obstacles restrict the design and material of electrode devices, including the required flexibility, transparency, low impedance, high charge storage capacity (CSC), and high charge injection capacity (CIC), among others. The impedance of transparent graphene arrays is higher, and its CIC is significantly lower than platinum, a metal typically employed for electrophysiological recording and stimulation. It is possible to enhance the electrochemical properties of planar, transparent graphene electrodes by functionalizing their surfaces with platinum nanoparticles (Pt NPs), effectively increasing the electrode surface area. Existing research on platinum nanoparticles on transparent graphene electrodes has solely focused on simultaneous electrical recording and optical imaging of neuronal activity. There is currently no quantitative evidence of the extent to which platinum nanoparticles can impact the stimulating properties of transparent graphene electrodes and any indication of the stability of the coating. Therefore, material and electrochemical device characterizations were conducted to compare the recording and stimulating properties of graphene versus graphene with Pt NPs of varying surface densities.

Acknowledgements

First and foremost, I am grateful to my supervisors, Sten, Vasso, and Nasim, for their invaluable counsel, continuous support, and patience during my study. I also want to thank Nasim for her technical and practical assistance with sample preparation, experiment setup, and everything in between. I want to express my gratitude to the ECTM and EKL team for all the module training I had to complete. I am also thankful for the opportunity to be a part of EKL as a process engineer during this time, as I learned many more beyond the scope of this research. In addition, I would like to express my appreciation to Esad, Hanxing, and Joost for their generous support throughout my nanoparticle printing struggles. I am also grateful for my family and Reno, whose confidence in me has kept me motivated. And lastly, I wish to dedicate this thesis to my mother.

List of Figures

List of Tables

Contents

1

Introduction

The brain is composed of tens of thousands of distinct cell types called neurons, which are organized into densely interconnected networks that interact with each other. Each of those neurons communicates with another using an electrical impulse in the form of an action potential. An action potential is a fast and propagating change in the resting membrane potential. As ions move through ion channels and cross from one side of the cell membrane to the other, they cause the cell's membrane potential to move away from its resting potential. When the stimulation is large enough to bring the membrane potential in the neuron body up from -70 mV to the threshold of -55 mV, this triggers an action potential. The cell depolarizes, followed by repolarization and, in some instances, a brief hyperpolarization phase [1]. This process is presented in Figure 1.1. At the neuron's axon terminal, the influx of Ca^{2+} ions causes synaptic vesicles to release neurotransmitters. Depending on the neurotransmitter, they may bind to the next neuron's ion channels and subsequently open, causing another neuron to depolarize from its resting potential, creating a cascading network of activated neurons. This leads to one of neuroscience's most complex challenges: understanding the network of neurons that influences a person's behavior, emotion, and motor control in health and sickness.

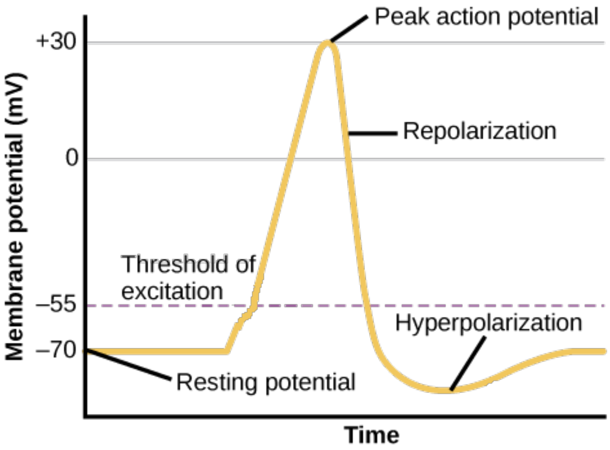

Figure 1.1: A graph of an action potential [2]

Electrophysiology is a method that investigates the electrical properties of cells by recording and stimulating living neurons. The conventional method activates neurons (by injecting currents or potentials) or records their signal (by measuring the impedance of nearby tissues to infer cell physiology). However, these current neural monitoring and controlling technologies provide insufficient spatiotemporal resolution to unravel neural circuit functions. Electrical stimulation makes it difficult to ensure that just a local brain region or a specific pathway is impacted. Multimodal neurotechnologies combining electrical, optical, and chemical sensing and stimulation modalities have been proposed to overcome these resolution limits [3], [4]. Promising ways to achieve this is through optogenetics, a neuromodulation technique that can activate specific neurons using light, and calcium imaging, a microscopy technique that visualizes calcium ion flow.

1.1. Optogenetics

A recording of the electrical pathways of neurons and optogenetic control has high ramifications on advancing behavioral experiments attempting to establish causality and further understand neural circuit dynamics. The ability to activate or deactivate a set of cells can contribute to understanding the behaviors they affect or initiate on a cellular level, influencing the psychology and physiology of the person. Neurons can be sensitive to light by introducing light-sensitive proteins or opsins into the cell membrane. Specific wavelengths stimulate these proteins, modulating neuronal activity with high specificity. Target neurons can either depolarize or hyperpolarize when illuminated. Cation-conducting channelrhodopsins (e.g. ChR-2) expressed in the cell membranes can activate neurons, eliciting action potentials [5]. They are originally isolated from the green alga *Chlamydomonas reinhardtii* and are activated by blue light (λ= 473 nm) at power densities of 8- 12 mWmm^{-2} [5].

Conversely, the expression of halorhodopsin or anion- conducting channelrhodopsins (e.g., NpHR) can inhibit neuronal activation. These proteins were isolated from an aerobic archaeon called *Natronomonas pharaonis*. When triggered, they pump chloride ions into the cell and are most active when exposed to amber light(λ= 590 nm), hyperpolarizing the neurons [6]. Additionally, redshifted activation wavelength opsins (e.g., C1V1 variants) are sensitive to light at 560 nm but depolarize the neuron [6].

1.2. Fluorescent Calcium Imaging

Modern genetic technology and microscopy can be combined to modulate and visualize cellular interactions. Fluorescent calcium imaging, for example, can detect neural activity and connect behavioral characteristics with physiological conditions. A genetically engineered calcium indicator, or GCaMP, is necessary to monitor the movement of calcium ions during neural signaling. GCaMP is a hybrid calcium sensor by enhanced green fluorescent protein (GFP), encoded by the calcium-binding protein called calmodulin and the calmodulin-binding peptide M13 enzyme. In the presence of calcium, calmodulin conformationally changes and becomes free to bind the M13 domain, causing the GFP to emit more light at a peak of 509 nm [7], [8]

Calcium signaling is a critical element of neuronal signal transmission. It establishes a causal link between neuronal activity and resulting physiology, offering quantitative information on neural activity. Calcium concentration increases within the cell when stimulated, activating the calcium sensor. As a result, the relative changes in calcium levels inside an organism's cells over time can be observed through a fluorescent microscope (eg., confocal laser scanning microscope and two-photon microscope). This technique has been used in zebrafish, mice, and C. elegans [8], [9] to study their motor cortex behavior. Additionally, several illnesses, like Alzheimer's and schizophrenia, have also been associated with intracellular calcium imaging, providing greater knowledge of the pathophysiology of these diseases [10], [11].

1.3. Transparent Electrode Devices

Integrating optogenetics, electrophysiology, and calcium imaging might yield new insights into the functioning of brain circuits. Once neurons have been sensitized to light, fiber-optic cables, LEDs, or lasers provide photostimulation to the neurons in a temporally precise way. *Ex vivo* or *in vivo* experimental conditions can examine the efficacy of the photostimulus, whose effects on the cells can be assessed using electrode devices. In addition, simultaneous neuroimaging and electrophysiology provide precise information on the identification, spatial location, and activation patterns of neurons, decoding the functions of individual circuit elements. Consequently, there are several opportunities for advancing brain recording and stimulating electrodes and incorporating compatibility for optogenetics and imaging modalities. A promising technological complement is transparent electrode devices.

Transparent electrode devices allow direct illumination of the neurons below the site. Opaque metal microelectrode arrays, like platinum or gold, are ineffective for this purpose. They limit the field of vision, produce optical shadows, are prone to introducing light-induced artifacts into the recordings, and the light stimuli can only activate cells around the opaque electrodes, negatively impacting high-resolution optogenetic tests [12]. For these reasons, engineers have considered using ultrathin metals for transparent neural interfaces (e.g., 3nm thick palladium, 5nm thick aluminum, and 9nm thick gold). However, their optical transmittance (≈60-65%) still pales compared to ITO's (≈80%) and graphene's (≈90%) as shown in Figure 1.2[3].

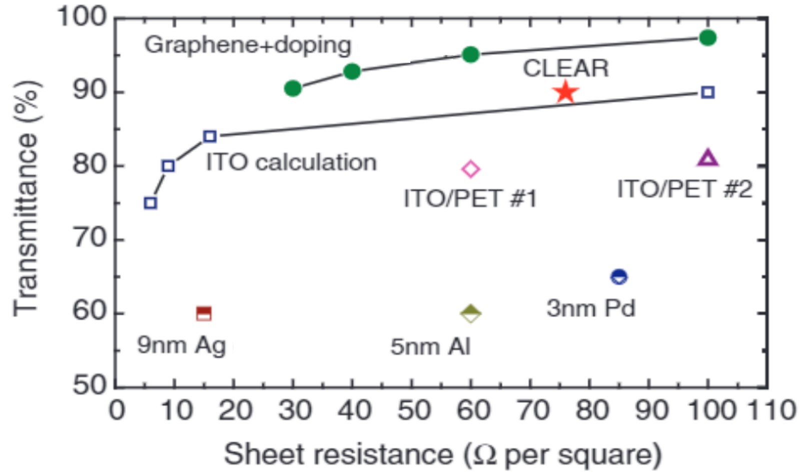

Figure 1.2: Graph on transmittance versus sheet resistance of conductive materials. CLEAR is a four-layered graphene-based electrode array device by Park et al. [3]

Researchers have attempted to fabricate transparent electrodes using indium tin oxide (ITO). Due to its high optical transmittance (≈80%) and low sheet resistance, ITO is the most widely used transparent electrode material in optoelectronic devices such as organic light-emitting diodes (LEDs), organic solar cells, and touch panels. However, ITO is inherently stiff and brittle, limiting its prolonged use on curved biological surfaces. As seen in Figure 1.3, ITO cracked under ≈ 2-3% tensile strain, while graphene resisted the strain up to 6%. Since ITO's electrical resistance increased with higher tensile strain, it renders it unsuitable for flexible electrode arrays since its electrical conductivity will be unstable for this application [13]. Additionally, a thin brittle film under compression leads to buckling to mitigate the stress, resulting in delamination from the flexible substrate [14].

Researchers have also attempted to investigate the effectiveness of graphene and PEDOT:PSS for multimodal recording with calcium imaging and achieved artifact-free recording. Investigations compared graphene electrodes with gold and platinum for multimodal recording. Their results indicate observable light-induced artifacts on gold and platinum, but hardly any on graphene electrodes [3], [15], [16]. However, there is also interest in using poly(3,4-ethylenedioxythiophene) polystyrene sulfonate (PEDOT:PSS), a conductive polymer, for this purpose. Its high transparency was useful for recording artifact-free signals, but its electrochemical impedance is relatively higher than current metal-based electrodes [17]. Conversely, a recent publication has shown that the fabrication parameters control the electrical performance of PEDOT:PSS thin films, achieving improved electrochemical performance compared to thin gold electrodes [18]. However, PEDOT:PSS thin film electrodes have been largely active in the ohmic regime, which is undesirable for neural electrode applications as this leads to damage to the cells and tissue [18]. Therefore, graphene is a more promising material for optogenetic and calcium imaging applications because it has a high light transmittance over a wide spectrum from the ultra-violet (λ= 300nm) to the infrared (λ= 1500nm) spectrum and stable electrical properties even under tensile and compressive stress, suggesting that graphene can wrinkle coherently with the underlying flexible substrate without compromising its electrical properties.

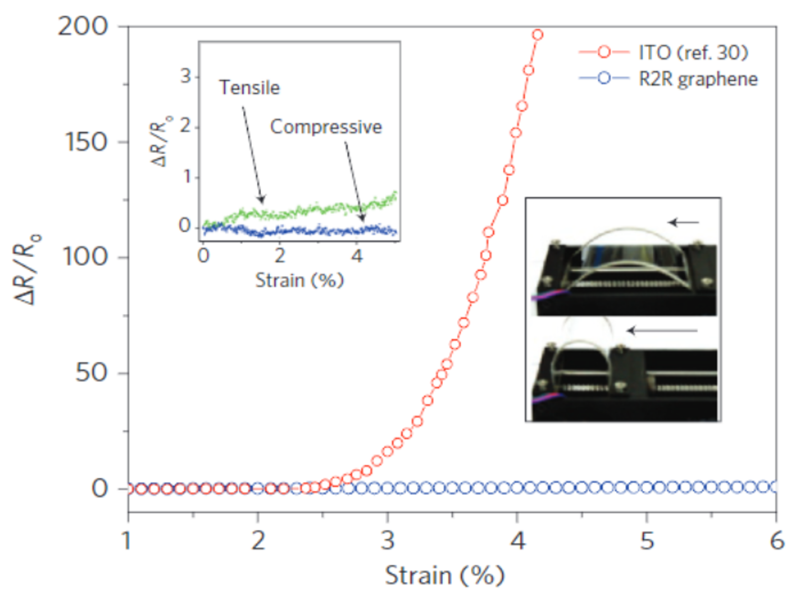

Figure 1.3: Electromechanical properties of graphene-based touch-screen devices versus with ITO/polyethylene terephthalate (PET) electrodes under tensile strain. The inset presents the resistance change with compressive and tensile stress of graphene/PET panels [13]

1.4. Graphene for Neural Devices

Graphene is a single-atom-thick layer of sp^2-bonded carbon atoms organized in a hexagonal pattern. This two-dimensional (2D) compound is the thinnest known material, making it transparent. It also has a large surface area (theoretically 2630 m^{2}g^{-1} for single-layer graphene), excellent thermal and electric conductivity and high mechanical strength [19]. Because of these unique physiochemical features, graphene has significant promise in various applications in biomedical technology, including neural interfacing for simultaneous electrophysiology, optogenetics, and imaging.

One example involves experiments on graphene electrodes, specifically a 4-monolayered electrode array on parylene C substrate with gold and chromium (Au/Cr) interconnection lines. These electrodes were tested on the somatosensory cortex of mouse models, where a blue laser delivered optogenetic stimulation to neurons directly below the electrode. The experiments with graphene electrodes recorded evoked neural responses to light stimulation (at λ= 473nm with 1.24 mWmm^{-2}) [3]. Additionally, fluorescence imaging was integrated into the study, demonstrating the graphene electrode's high transparency within the visible spectrum. Other studies have demonstrated electrophysiological recording using graphene electrodes on ultrathin polyimide substrates (thickness 12.5 nm) [4] and graphene arrays on PET [20] using two-photon calcium imaging, and also a 16-channel graphene electrode array on parylene C substrate using fluorescence microscopy [21]. Integrating microscopy and imaging technologies with graphene-based neural electrodes may facilitate the recognition of abnormal changes in blood flow, vascular diameter, collagen formation, microglial activation, and astrocyte reactions, among others, as symptoms of underlying conditions [22]. Therefore, researchers could gain insights into the brain's complexity by studying physiological and morphological responses to light while recording the neural response through a transparent graphene electrode. Figure 1.4 illustrates a schematic of simultaneous optical imaging and optical stimulation with a transparent graphene electrode.

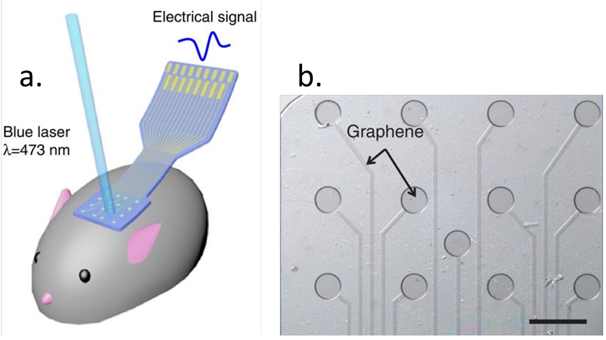

Figure 1.4: (a) Schematic image of a blue light stimulus delivered via an optical fibre, through a transparent graphene device on the cortex of a mouse, (b) Transparent graphene electrode traces and sites on a parylene C substrate. Scale bar is 500 μm

The electrode's impedance is an important parameter to consider for the further development of neural devices. The device's impedance affects signal quality because high impedance increases the noise level, resulting in a lower signal-to-noise (S/N) ratio [23]. In the studies previously mentioned, the researchers have demonstrated the integration of graphene electrodes with optogenetic stimulation and fluorescence microscopy techniques. However, studies show that the impedance of graphene is still much higher than conventional metal electrodes like platinum and gold used in most neuroprosthetic applications. The 4-monolayered graphene electrode array by Park et al. has an impedance of 243.5 ± 5.9 kΩ at 1 kHz, higher than Pt electrodes (188.8 ± 92.9 kΩ at 1kHz) with similar geometric surface area[3]. Bakhshaee Babaroud et al. also reported higher impedance on their multilayer graphene (27.4 ± 7.5 kΩ at 1kHz) compared to gold (7.5 kΩ) and platinum(8.7 kΩ) with the same geometric surface area [15].

Moreover, electrodes with suitable charge injection capabilities for stimulation applications are another critical technological challenge. Electrical stimulation requires a minimum charge-injection capacity (CIC) to elicit a tissue response at the stimulation site, which must not trigger irreversible reactions. Such reactions are water electrolysis (oxygen or hydrogen evolution), metal-ion oxidation, and electrode corrosion or dissolution, which result in soluble metal–ion complexes [24], [25] These unfavorable interactions can cause a variety of local and systemic biological responses, such as fibrous tissue encapsulation, ultimately leading to the device's failure because the signal quality has degraded [24], [25]. Hence, these are critical limitations to consider for the effective and safe use of these brain activity measurement and stimulation systems on living patients, especially for invasive procedures. Bakhshaee Babaroud et al. also reported that graphene can safely inject charge at 44 μCcm^{-2}, gold at 11.7 μCcm^{-2}, and platinum at 67.33 μCcm^{-2} [15]. Although the graphene electrode performed better than gold, it is still much lower than platinum, despite graphene being able to store more charge than platinum.

The selection of electrode material determines the effectiveness, performance, reliability, and lifetime of neural interfaces. The benefits of one material can outweigh the disadvantages of another. Metal electrodes can be made into thin fiber structures for stimulating applications. Wang et al. demonstrated a synergistic effect between graphene and platinum, leading to a hybrid material with better performance than graphene or platinum fiber electrodes [26]. The fabricated graphene fiber-based microelectrode arrays with a thin platinum coating (GF-PT) and insulated with parylene-C were found to have a charge storage capacity of 946 140 ± mCcm^{-2}, two orders of magnitude higher than the unmodified graphene fibers. Additionally, the charge injection capacity of the GF-PT microfiber at 10.34 ± 1.5 mCcm^{-2} was found to be approximately two times larger than its unmodified graphene counterpart [26]. The fiber-like structure cannot be combined with simultaneous electrophysiology, optogenetics, and imaging approaches, even though these graphene-platinum electrodes offer promising findings for stimulating capabilities. Consequently, there is logical interest to investigate this effect for multimodal neural recording and stimulation.

1.5. Objectives of the Project

Graphene electrodes can achieve simultaneous electrophysiological recording, optical imaging, and optogenetic stimulation. However, its impedance is higher, and charge injection capacity is much lower than platinum, a metal used for conventional electrophysiological recording and stimulation. Yet, a synergistic interaction between graphene and platinum improved its electrochemical performance compared to a graphene-based electrode when characterized for neural recording, and stimulation applications [26]. Conversely, platinum is an opaque metal and cannot be utilized simultaneously for electrophysiological recording, optical imaging, and optogenetic stimulation for the reasons outlined in Section 1.3. Tuning the material down into nanoparticles can exhibit different physical and chemical properties. Dao et al. demonstrated the high transparency of Pt nanoparticles on graphene with a transmittance of at least 80% from 500 nm to 1000 nm wavelengths, but this was developed for solar cell applications [27]. Lu et al. fabricated platinum nanoparticles on graphene neural electrodes and showed improved impedance, but its stimulating capabilities and coating stability were left unanswered [28]. Hence, there is reasonable interest in improving the electrochemical performance of graphene with a platinum nanoparticle coating for optogenetic applications by integrating the physical and chemical characteristics of graphene and platinum. Several objectives summarize the approach of this research, specifically to:

1. Fabricate graphene electrodes
2. Characterize the platinum nanoparticle deposition
3. Functionalize the surface of graphene electrodes with platinum nanoparticles
4. Compare the electrochemical performance of graphene electrodes versus graphene electrodes with platinum nanoparticles for recording and stimulating applications
5. Evaluate the optical transmittance of graphene and platinum nanoparticles
6. Evaluate the stability of the metal nanoparticles on graphene and investigate its effect on its electrochemical performance

1.6. Outline of the Report

This report consists of six chapters, of which Chapter 1 provides a brief introduction and motivation for the project. The review of related literature is in Chapter 2, where information on graphene and platinum nanoparticles are found, including the current-state-of-the-art graphene neural electrodes and the functionalization of electrodes with nanoparticles. It also details characterization techniques used in other research relevant to this, such as the electrochemical characterization methods for biomedical electrodes. Chapter 3 presents the materials and methodology used to complete this research. It details the device fabrication process and presents the test setup and optimization approaches for these setups. The results and discussion are found in both Chapter 4 and Chapter 5, where the former presents results of the material characteristics, which includes nanoparticle density, optical transmittance, and roughness. In contrast, the latter shows the results from the electrochemical tests. Lastly, Chapter 6 concludes the research with recommendations for future research to improve the methodologies, experimental setups, and to investigate more capabilities of the graphene electrodes with nanoparticles.

2

Literature Review

2.1. Electrodes and the Electrode-Tissue Interface

The vital component in the electrical sensing of the brain is the electrode. This device is the interface between the electronic components and living tissues or cells. An electrode is a transducer that converts ionic currents from the human body into electrical currents that conventional electronics can then measure. Electrodes stimulate neurons (by injecting currents or potentials) or record their signal (by measuring the impedance of nearby tissues to infer cell physiology) [29]. The recorded signals are usually small, from tens of microvolts to an amplitude of about 80 mV for intracellular potentials. Conversely, neural stimulation requires higher electrode voltages and current densities to trigger chemical reactions [30]. Regardless of the application, electrodes interact with the ions in the human body since these ions serve as charge carriers and are the mechanism for the body's electrical activity.

The electrode-tissue interface of a recording or stimulating electrode is the interface between the electrode and the surrounding tissue, which can be described as an electrolyte or an ionic solution. When an electrode is placed into an electrolyte, a local rearrangement of charges occurs across the electrode-electrolyte interface, forming a capacitive double layer and a potential difference between the electrolyte around the metal and the rest of the solution, called the half-cell potential [23]. When an external voltage is applied between two electrodes in an electrolyte, current starts to flow from one electrode through the electrolyte to another electrode. The charge can move from the electrode to the electrolyte in two ways: Faradaic and non-Faradaic reactions. Faradaic reactions are caused by the exchange of electrons between metal atoms on the electrode and species in the electrolyte, resulting in some reduction or oxidation processes. In contrast, non-faradaic reactions are capacitive since there is no transfer of electrons across the interface [31].

Figure 2.1 illustrates a simple circuit model of the electrode-electrolyte interface. It typically consists of a faradaic impedance (Z_{el}) and a capacitor representing the non-faradaic impedance (C_d). It also presents the half-cell potential (E_{hc}) and the R_s, which is the resistance of the electrolyte. Additionally, Faradaic charge injection is often described as irreversible because it forms products in the solution that cannot be recovered by reversing the direction of the current if the products diffuse away from the electrode. There is a net change in the chemical environment due to the irreversible Faradaic reactions, which may produce chemical species harmful to tissue or the electrode [31]. Thus, avoiding irreversible Faradaic reactions is an important objective of electrical stimulation design.

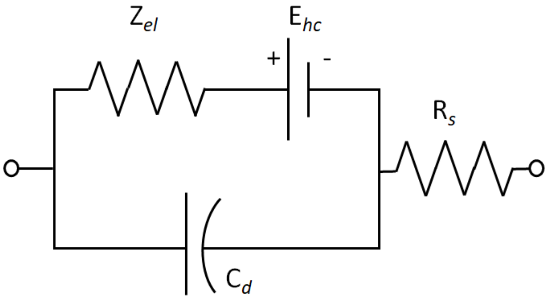

Figure 2.1: Electrical circuit model of an electrode-electrolyte interface. Modified from [31]

2.2. Characterization Methods for Neural Electrodes

Impedance spectroscopy, cyclic voltammetry, and voltage transients are standard electrochemical electrode characterization methods. This subsection describes how each method can provide distinct information on electrode performance.

2.2.1. Electrochemical Impedance Spectroscopy

Electrochemical impedance spectroscopy (EIS) is a method that characterizes electrode processes and complex interfaces. This approach investigates the system's reaction to applying a periodic AC signal with a small amplitude. The measurements are performed at various AC frequencies; hence, it is aptly called a spectroscopy method [23]. EIS is done by applying a sinusoidal excitation voltage between the working and counter electrodes with a given small-amplitude frequency (0.01–0.2 V). The circuit's current and the working electrode's voltage relative to the reference electrode are then measured. The electrochemical impedance spectrum is then constructed by sweeping the excitation frequency throughout a range, generally between 0.01 Hz and 1 MHz, allowing for the analysis of fast and slow kinetic transport processes [29].

Since the sinusoidal perturbation amplitude is kept low, the electrode is believed to function under linear conditions. Hence, Ohm's law may be used to compute the electrode impedance at a particular frequency. Shown in Equation 2.1 is Ohm's law, where *U* is the potential (V), *I* is the current (A), and *R* is the resistance (Ω).

$$E = IR \tag{2.1}$$

Electrochemical impedance is measured in Ohms (Ω) and indicates how much an electrode resists charge transfer from an ionic medium. Low-impedance electrodes have better contact with tissue or ionic fluid and may easily transduce charges. Both the voltage and current are sinusoidal, time-dependent functions in EIS. A single-frequency potential input with amplitude (E_o) and radial frequency (ω=2πf) is expressed in Equation 2.2. A sinusoidal potential produces a sinusoidal current response with the same frequency but shifted in phase. This output has a phase shift (φ), and amplitude (I$_o$), shown in Equation 2.3.

$$E(t) = E_o sin(\omega t) \tag{2.2}$$

$$I(t) = I_o sin(\omega t + \varphi) \tag{2.3}$$

The physical phenomena of the electrode in the electrochemical system can be linked to the behavior of common circuit elements, which have different responses to alternating electrical signals [29]. The impedance of the electrode can then be expressed through Ohm's Law, in terms of a magnitude Z$_o$ and a phase shift. Equation 2.4 simplifies to Ohm's Law if the system has no phase shift (φ=0), representing a resistor. A capacitor, however, can be expressed in Equation 2.5, where *C* is the capacitance and *j* is the imaginary component.

$$Z = \frac{E}{I} = \frac{E_o sin(\omega t)}{I_o sin(\omega t + \varphi)} = Z_o \frac{sin(\omega t)}{sin(\omega t + \varphi)} \tag{2.4}$$

$$Z_{capacitor} = \frac{1}{j\omega C} \tag{2.5}$$

EIS measurements can be represented in two different ways through the Bode plot and Nyquist plot. The Bode plot represents the magnitude of impedance and phase shift against frequency expressed in Equation 2.6 and Equation 2.7, which is the vector sum of the real (Z') and imaginary impedance (Z") [23]. On the other hand, the Nyquist plot shows the negative imaginary impedance versus the real impedance. Both plots are shown in Figure 2.2.

$$|Z| = \sqrt{Z'^2 + Z''^2} \tag{2.6}$$

$$\varphi = \arctan\left(\frac{Z''}{Z'}\right) \tag{2.7}$$

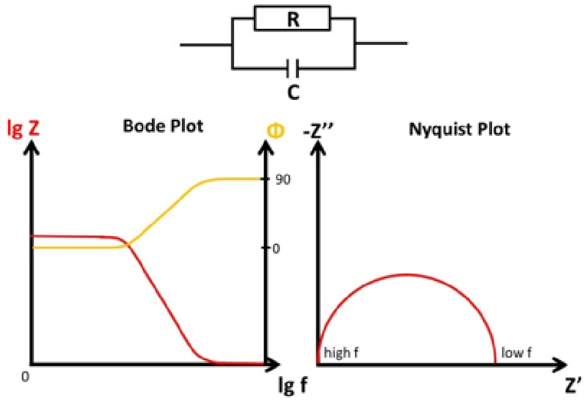

Figure 2.2: (a) Bode plot and (b) Nyquist plot of a resistor and capacitor in parallel [32]

The three-electrode configuration is commonly used to take EIS measurements. The current flow between the working electrode and a counter electrode in a three-electrode cell. A third electrode, the reference electrode, is used to estimate the working electrode's interfacial potential. Since current only flows between the working electrode and the counter electrode, there will be no change in the interfacial potential of the reference electrode that would affect the impedance measurements [29], [33]. Figure 2.3 presents the three-electrode setup.

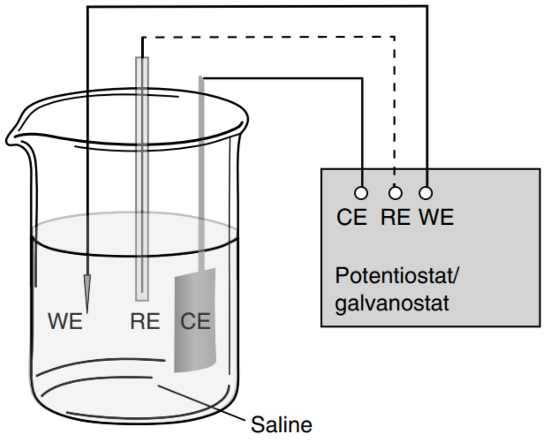

Figure 2.3: Three-electrode setup with the working electrode (WE), reference electrode (RE) and counter electrode (CE) [23]

2.2.2. Cyclic Voltammetry and Charge Storage Capacity

Cyclic voltammetry (CV) is a three-electrode measurement similar to the electrode setup used for impedance measurements. CV identifies electrochemical reactions and offers information on reversibility, electroactive material, and electrode stability [29]. The working or test electrode's potential is swept cyclically at a constant rate between two potential limits while current flows between the working electrode and a counter electrode. The data from CV are typically plotted as the measured current versus the applied voltage. The water window is often utilized during measurements, which is the voltage range between the oxidation and reduction potentials measured against the reference electrode. During CV testing, the rate of charge transfer reactions and capacitive charging at the electrode-electrolyte interface is measured by how much current flows through the system [29]. However, this measurement depends on multiple factors, such as the scan rate, the electrode's geometric area, and surface roughness. The experiment's scan rate determines how rapidly the applied potential is scanned. A high scan rate inhibits the contribution to charge transduction of transport-limited electrode areas, providing information only on the exposed electrode regions [29], [34].

Stimulating electrodes can be characterized using CV by calculating the charge storage capacity (CSC) from the current measured. CSC is the total charge available for a stimulation pulse. The charge storage capacitance is determined by taking the time integral of the current observed across a potential range slightly within the water window [29], [34]. In that way, the CSC represents the charge stored in reversible processes, including that of charging the double-layer capacitance, adsorption, and those in which the solution-phase product remains close to the electrode due to mass transport constraints [33].

2.2.3. Voltage Transient and Charge Injection Capacity

In the same three-electrode setup, polarization can be characterized through voltage transient (VT) measurements. VT measures the polarization of the electrode system in response to charge injection. It estimates the maximum charge injected in a current-controlled stimulation pulse. Therefore, stimulating neural electrode devices are also characterized by the maximum charge injection capacity (CIC), denoted as Q_{inj}.

Charge injection for neurostimulation is typically a biphasic charge-balanced signal, meaning the charge injected in the first half-phase is compensated for by reversing polarity in the second half, maintaining the net charge transfer to zero [29], [34]. Figure 2.4 shows a microelectrode's voltage transient in response to a biphasic-charge balanced stimulation where the phase of charge is determined by the current amplitude and pulse width and then an interphase delay before the start of the next current pulse. At the start of the cathodic current pulse, the potential across the electrode system drops due to the resistive components of the circuit (cables, electrolyte, and conducting tracks) [29]. This is referred to as the access voltage (V_a), which instantaneously occurs at the start and end of a current pulse. The most negative (E_{mc}) and most positive (E_{ma}) polarization is determined by the change in polarization across the electrode-electrolyte interface relative to the electrode's potential at the start of the current pulse. Thus, the cathodal current pulse is then described in Equation 2.8. VT measurements start with a small current amplitude and steadily increase until E_{mc} or E_{ma} are slightly below the water window. That maximum current amplitude (I_{max}) within the water window defines the maximum CIC [23]. CIC is the maximum charge per pulse (t_c) that may be injected over a unit area before any onset of anodic or cathodic water electrolysis (See Equation 2.9).

$$E_{mc} = E_{ipp} + \Delta E_p = E_{ipp} + (\Delta V - V_a) \tag{2.8}$$

$$Q_{inj} = \frac{I_{max} t_c}{Area} \tag{2.9}$$

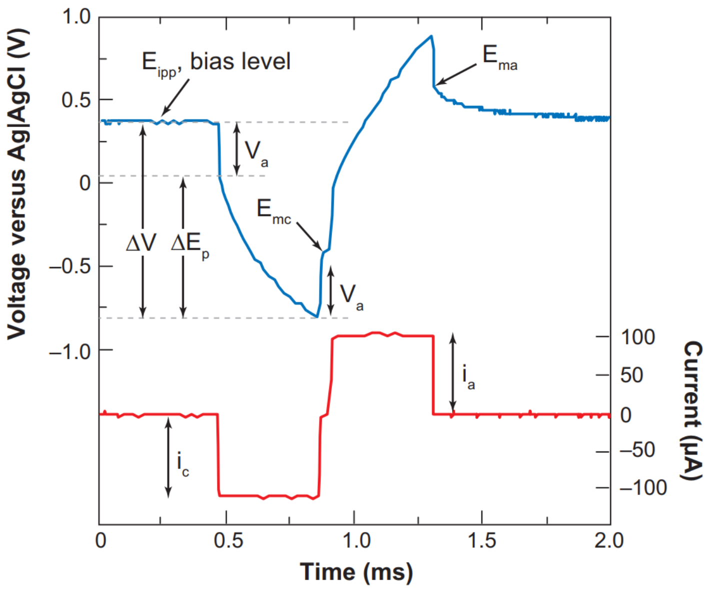

Figure 2.4: Voltage transient of a microelectrode in respose to a biphasic pulse [34]

2.3. Challenges and Limitations of Neural Electrode Material and Designs

For neural interfaces to reach their full potential, many challenges must be overcome with the current systems and devices. In particular, the limitations for advancing next-generation neural interfaces are selectivity, spatial and temporal resolution, stability, and safely managing host-interface responses [35]. Selectivity is the capacity of an interface to record or activate specific neurons, nerves, or motor units. The spatial resolution measures how precisely the recording or stimulating signal can be localized. Temporal resolution relates to how closely the recorded activity matches the actual time of the neural activity. Lastly, any neural interface intended for implantation should be as non-invasive as possible, allow for a simple surgical procedure, and deliver efficient and constant activity for its useful life, which corresponds to the stability and safety of the devices.

Metals like platinum (Pt), gold (Au), iridium (Ir), titanium (Ti), and their alloys are common electrodes for neural interfaces due to their chemically inert properties, excellent biocompatibility, and good electrical characteristics [33], [34]. However, the functionality of these materials as an electrode is limited by their rigidity, creating a mechanical mismatch between the implantable device and the nervous tissues. Moreover, soft and conformable materials provide long-term stability and biocompatibility of the implant. Stiff implants can function for a limited time before the sensor substrate develops cracks or the interfacial layer delaminates [36], [37]. There has also been extensive research on developing electrode arrays with polymer-based substrates like polyimide, parylene C, and polydimethylsiloxane (PDMS) and poly(3,4-ethylenedioxythiophene) (PEDOT) [38]. These flexible and soft materials can dynamically conform to the shape of the irregular soft tissue surfaces, providing a better mechanical match between the implant and biological tissue and reducing inflammation [38]. Further, micromotions between the neural tissue and the implant can also trigger an inflammatory response, forming an insulating sheath or glial scar tissue around the device, ultimately leading to its failure because the signal quality has degraded [25]. Hence, these are critical limitations for the effective and safe use of neural recording and stimulating electrodes on living patients, especially for invasive procedures.

Despite these limitations, various opportunities exist to advance brain recording and stimulating electrodes. Efforts to create and incorporate new materials that can offer as many alternatives as possible for designing neural interface devices with different capacities and functionalities are critical to developing next-generation brain interfaces. As discussed in Chapter 1, multiple modalities can overcome selectivity and resolution limits. Combining optogenetics, calcium imaging, and transparent electrode devices allows simultaneous electrophysiological recording, optical stimulation, and microscopic visualization of specific genetically modified cells. Furthermore, shrinking electrode sizes decreases the invasive footprint of the device on the host. It also improves the device's selectivity; electrodes as small as 40 to 400 μm^2 can record a neuron's soma which is approximately 4-100 μm in diameter [39]. However, miniaturization increases electrode impedance. By decreasing the geometrical surface area of electrodes, the charge injection capacity must increase to compensate and deliver the same amount of charge for a successful stimulation, which increases the risk of irreversible faradaic reaction and tissue damage. Hence, microelectrodes can be coated with a conductive functional layer to provide a sizeable surface area.

Solving the circuit shown in Figure 2.1, the real and imaginary impedance is expressed as a function of the area. When the area increases, the real and imaginary impedance will decrease. Equation 2.10 and Equation 2.11 represent real and imaginary impedance. Equation 2.12 models the capacitive double layer as a parallel plate capacitor. In that equation, capacitance is proportional to surface area (A), and dielectric constant (ε_r) and permittivity of vacuum (ε_0, 8.85 × 10^{-12} F/m), whereas the thickness of the double layer (d) is inversely linked. The double layer thickness is commonly estimated as the Debeye length denoted as $K_D{}^{-1}$ [40]. In Equation 2.13, *k* is Boltzmann's constant, *T* is the absolute temperature, *e* is the electron charge, Z_i is the charge of ion species *i* and n_i^B is the bulk concentration of that species. Lastly, the summation includes all the ion species in the electrolyte. Moreover, the impedance can be rewritten to demonstrate their inverse relationship to the area (see Equation 2.14 and Equation 2.15).

$$Z' = R_s + \frac{R_{el}}{1 + \omega^2 R_{el}^2 C_d^2} \tag{2.10}$$

$$Z" = -\frac{j\omega R_{el}^2 C_d}{1 + \omega^2 R_{el}^2 C_d^2} \tag{2.11}$$

$$C_d = \varepsilon_0 \varepsilon_r \frac{A}{d} \tag{2.12}$$

$$K_D^{-1} = \sqrt{\frac{\varepsilon_0 \varepsilon_r k T}{e^2 \Sigma_{i=1}^{j} Z_i^2 n_i^B}} \tag{2.13}$$

$$Z' = R_s + \frac{R_{el} d^2}{d^2 + (\omega R_{el} \varepsilon_0 \varepsilon_r A)^2} \tag{2.14}$$

$$Z" = -\frac{j\omega R_{el}^2 \varepsilon_0 \varepsilon_r A d}{d^2 + (\omega R_{el} \varepsilon_0 \varepsilon_r A)^2} \tag{2.15}$$

2.4. Graphene as a Neural Electrode

2.4.1. Properties of Graphene

Graphene is a unique material in numerous aspects. Graphene's molecular structure resembles a honeycomb made of two-dimensional arrangements of carbon atoms. Each atom has three sp^2-orbitals, interacting with neighboring atoms to form covalent σ-bonds. The fourth orbital maintains a weaker van de Waals bond, which controls the link between layers to create multi-layer graphene and can form graphite when there are more layers. These π-bonds contribute to the electron conduction of graphene, where the valence and conduction bands intersect, resulting in a zero band gap [41]. Graphene's electron mobility at room temperature is reported to reach 15,000 cm$^2 V^{-1} s^{-1}$, offering significant advantages for electronic applications [41]. Figure 2.5 shows three σ-bonds in one plane and π-orbitals perpendicular to the plane σ-bonds [42].

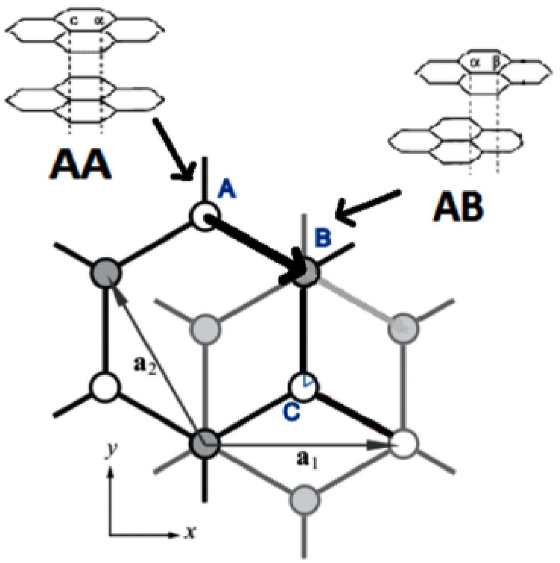

Figure 2.6: Stacking patterns of graphene bi-layer [43]

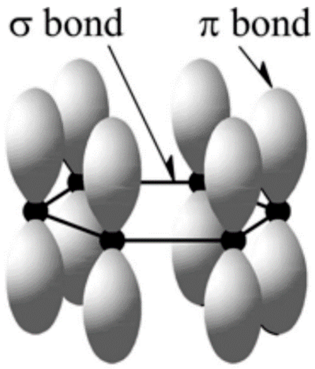

Figure 2.5: Schematic of the σ-bonds and the π-orbitals of graphene[43]

The reactivity and electronic properties of graphene depend on the number of layers and the relative position of atoms in adjacent layers. Because of graphene's 2-dimensionality, each atom in a single layer is exposed to chemical reactions from two sides. Bi-layer graphene can be stacked in one of two ways: with one atom sitting above the next in an AA-type arrangement or with the atoms of the second layer sitting atop the vacant center of the hexagon in the first layer (AB-type) [43], [44]. Consequently, adding layers complicates the stacking order. The forces that bond these layers are caused by weak van der Waals forces where the bond is spaced at a distance of approximately 0.335 nm [43]. However, the misalignment of the atoms between the layers (AB-type) leads to dangling bonds created when the valence state is not fully satisfied. Hence, carbon atoms of monolayer graphene and the first layer of AA structures do not create dangling bonds. However, in bi-layer or few-layer graphene, van der Waals forces are absent at the top carbon atoms, creating dangling bonds [44]. Carbon atoms at the edge also form chemical reactivity and will contain hydrogen atoms to stabilize its four valence electrons [19]. As a result, electron interaction with the top layer and edges of the graphene behaves differently from the bulk, promoting temporary chemical reactions or functionalization of the graphene's surface.

2.4.2. Synthesis of Graphene

Graphene was initially mechanically exfoliated from graphite using the Scotch tape method. Few-layer graphene samples are extracted from graphite by repeatedly peeling using adhesive tape [41]. A transfer on a substrate then follows this. However, this technique is uncontrolled as individual thicknesses vary [44]. Since then, numerous techniques for preparing graphene have been developed, including liquid phase exfoliation, reduction of graphene oxide, thermal aqueous phase exfoliation, epitaxial growth on silicon carbide, and chemical vapor deposition.

Liquid Phase Exfoliation (LPE) involves dissolving graphite or graphite oxide in a solvent, then agitation through sonication separates layers into two-dimensional sheets [42]. This results in graphene oxide. The presence of functional groups on the graphene decreases its conductivity, requiring reduction methods to restore it. There are various reduction methods of GO, namely thermal reduction, hydrothermal reduction, and electrochemical reduction, to name a few. However, these techniques have low scalability and yield and damage the graphene structure [44]. On the other hand, thermal aqueous phase exfoliation involves the treatment of graphene oxide with an oxidizing solution under rapid heating to separate the layers. This process takes long, and it is challenging to determine at which point to stop the heating process [44]. Another method to synthesize graphene is through the epitaxial growth on silicon carbide. Silicon carbide is used as a substrate, and the graphene is grown at high temperatures above 1100°C. Aside from the high-temperature requirement, graphene is often grown in small quantities using this method [42], [44].

Lastly, the chemical vapor deposition (CVD) method is a bottom-up approach for directly synthesizing graphene from a carbon precursor (i.e., methane). The CVD method achieves large single graphene sheets as they are grown on metal foil substrates or thin-films on wafers (i.e., copper). However, this process is limited by its post-production methods, where transferring graphene from the metal surface to a dielectric surface or another substrate of interest often rips or tears the sheet [19], [42]. Hence, a transfer-free process has been developed where graphene is grown on a molybdenum (Mo) substrate [45]. The metal substrate is deposited on SiO_2, the graphene is deposited after, and the molybdenum is wet-etched, resulting in graphene sticking on the now exposed oxide layer. Thus, allowing the exact patterning of graphene by pre-patterning the molybdenum catalyst.

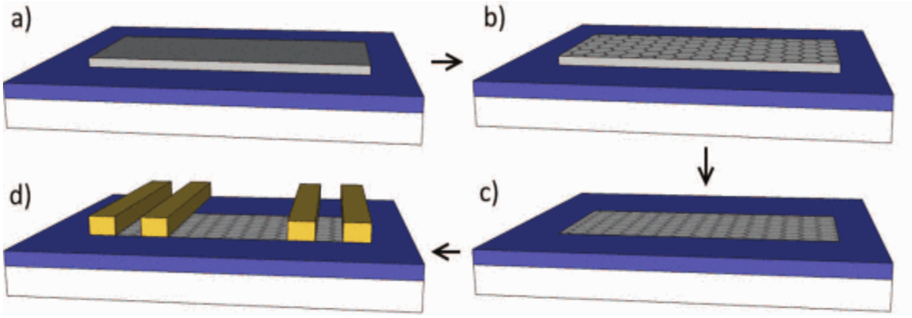

Figure 2.7: Schematic overview of the transfer-free process: (a) deposition and patterning of the Mo layer on silicon substrate with 90 nm SiO_2, (b) CVD deposition of graphene on Mo,(c) wet-etching of the mo layer (d) deposition of Chromium/Gold electrodes by a lift-off process [45]

2.4.3. Current State-of-the-Art Graphene Neural Electrodes

Graphene has shown significant promise for neural interfacing because of its unique physiochemical features. It has been utilized for neural electrodes with different designs owing to its material properties. Graphene-based electrodes are a versatile material that could assist to overcome many of the challenges in neural interface design due to their electrical properties and versatility for integrating into transparent flexible devices. Section 1.4, Graphene for Neural Devices, briefly describes some literature on graphene electrodes used for simultaneous electrophysiology and imaging. Table 2.1 summarizes these devices and other published work on transparent graphene's recording and stimulating capabilities.

Table 2.1: Properties of State-of-the-art Transparent Graphene Electrodes

Electrodes	**CSC (μCcm^{-2})**					**Electrode surface area (μm^2)**	**Water window (V)**	**CIC (μCcm^{-2})**	**Impedance at 1 kHz (kΩ)**	**Area-normalized impedance (Ω.cm^2)**	**Optical Transmittance at 550 nm**	**Reference**
	Type	**1 Vs^{-1}**	**0.6 Vs^{-1}**	**0.2 Vs^{-1}**	**0.1 Vs^{-1}**							
Graphene (20 min growth time)	Total	972	1298	2425	3549	68320	−0.8 to 0.6	44	27.4 ± 7.5	18.72 ± 5.1	83.5	Babaroud[15]
	Cathodic	631	812	1453	2151							
Graphene	Total			735		2500	−0.8 to 0.8				>80% (on polyimide)	Kuzum[4]
2-layer Graphene	Cathodic		15.9 at 0.5Vs^{-1}			2500	−0.8 to 0.8		2160 ± 230	54 ± 5.75	≈90% (with parylene both sides)	Driscoll[46]
Few layers Graphene	Total	910				707	−1.6 to 1.4	150	2650 ± ± 260	18.73 ± 1.84	>85% (on glass)	Korbitzer[47]
Four stacked monolayer graphene	Cathodic	87.8				31416	−0.6 to 0.8	57.13	215.7 ± 120.4	67.76 ± 37.8		Park[21]
Four stacked monolayer Graphene						unclear	−0.6 to 0.8		243.5 ± 5.9		≈90%	Park[3]
Graphene						2500			1400	35	>80% (on PET)	Liu[16]
Monolayer Graphene						10000	−0.6 to 1.1		872.9	87.29	>90%	Lu[28]
Graphene						10000			963	96.3	>80% (on PET)	Kuzum[20]
Monolayer Graphene						15394			200	30.79	≈90% (on SU-8/PET)	Park[48]
Monolayer Graphene						10000			200	20		Lyu[49]
Monolayer Graphene						707			3000	21.21	>85%	Kshirsagar[50]

Many researchers in Table 2.1 also compared their transparent graphene electrodes with other conventional metals for recording and stimulating neural activity. Babaroud et al. reported higher impedance on their multilayer graphene (27.4 ± 7.5 kΩ at 1 kHz) compared to gold (7.5 kΩ), and platinum(8.7 kΩ) with the same electrode surface area [15]. The CIC of the graphene was 44 μCcm^{-2}, gold at 11.7 μCcm^{-2}, and platinum at 67.33 μCcm^{-2} [15]. Although the graphene electrode performed better than gold, it is still much lower than platinum. Additionally, the stacked monolayer graphene by Park et al. exhibited a lower CIC (57.13 μCcm^{-2}) than Babaroud's platinum despite measuring the same negative polarization threshold potential of −0.6 V [15], [21]. Figure 2.8 presents the CV and VT results of Babaroud[15].

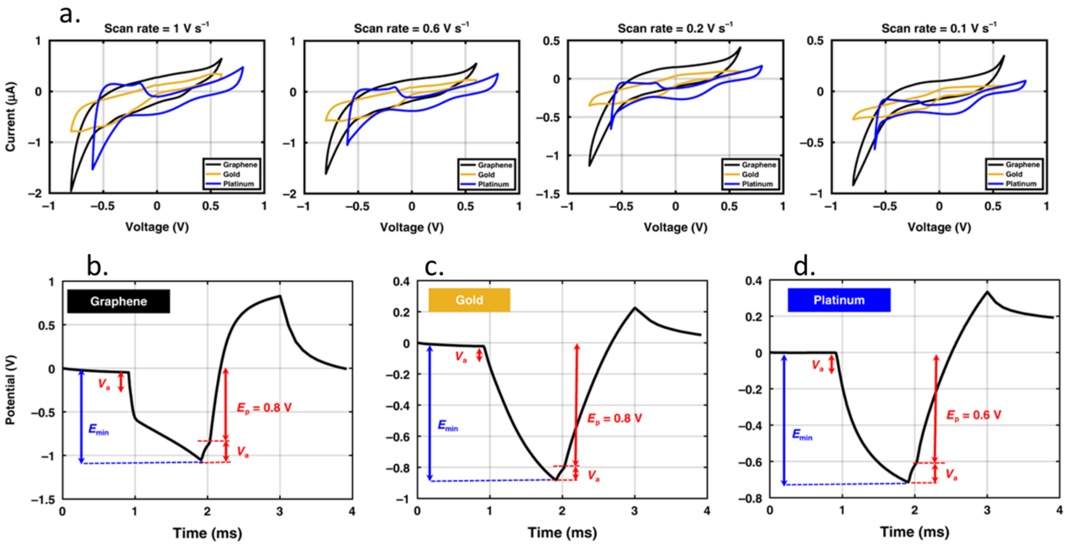

Figure 2.8: (a) Cyclic voltammograms of graphene, Pt, and Au electrodes with scan rates 1, 0.6, 0.2, and 0.1 Vs−1 from left to right, respectively, (b-d) VT measurements for graphene, Au, and Pt electrodes, respectively. [15]

In the previous work by Park et al., when they initially fabricated their four-stacked monolayer graphene electrodes, they also compared it with platinum and gold. The impedance was measured against platinum and found that graphene's impedance was slightly higher (243.5±5.9 kΩ at 1 kHz for graphene versus 188.8±92.9 kΩ for platinum) [3]. The cyclic voltammograms of platinum also showed a significant difference between graphene and gold (shown in a-b of Figure 2.9). The graphene's voltammogram was slightly larger than gold's [3]. This suggests that platinum has the largest charge-carrying capacity out of the three. However, a larger CSC does not typically reflect a better CIC. Table 2.1 shows that the four stacked monolayer graphene has a larger CIC (57.13 μCcm^{-2}) than the graphene grown for 20 minutes (44 μCcm^{-2}), despite the latter having a larger reported CSC.

Korbitzer et al. also compared graphene with gold, with similar surface areas (700 μm^2). Cyclic voltammetry tests showed higher charge storage capacity for graphene than gold, with 0.91 $\pm$ 0.13 $mCcm^{-2}$ and 0.73 $\pm$ 0.11 $mCcm^{-2}$, respectively [47]. However, graphene's CSC was slightly higher despite a much larger water window (−1.6 V to 1.4 V for graphene; -1.2 V to 0.7 V for gold), (see c-d of Figure 2.9). The charge injection capacity was comparable with only a one-point difference (0.15 $\pm$ 0.05 $mCcm^{-2}$ for graphene; 0.16 $\pm$ 0.04 $mCcm^{-2}$ for gold). Additionally, despite graphene's large safe stimulation window, its CIC still pales compared to titanium nitride (TiN; $\approx$ 0.87 $mCcm^{-2}$) and iridium oxide (IrOx; $\approx$ 4 $mCcm^{-2}$). All these research about transparent graphene electrodes (also see Section 1.4) suggests a trade-off between excellent transparency and subpar recording and stimulating capabilities compared to conventional metal electrodes.

Moreover, graphene can also be made into fibers, as demonstrated by Apollo et al. and Wang et al. These researchers examined graphene's potential as a closed-loop neural interface with recording and stimulating capabilities. Apollo et al. developed wet-spun liquid crystal graphene oxide (LCGO) fibers [51]. These fibers had parylene-C for insulation and lasered ends. Figure 2.10 shows the device fabrication with lasered ends at 250 mW to open the electrode while creating a roughened and porous surface [51]. The LCGO electrodes have a 62 $mCcm^{-2}$ CIC, much larger when compared to platinum electrodes of the same shape (0.26 $mCcm^{-2}$).

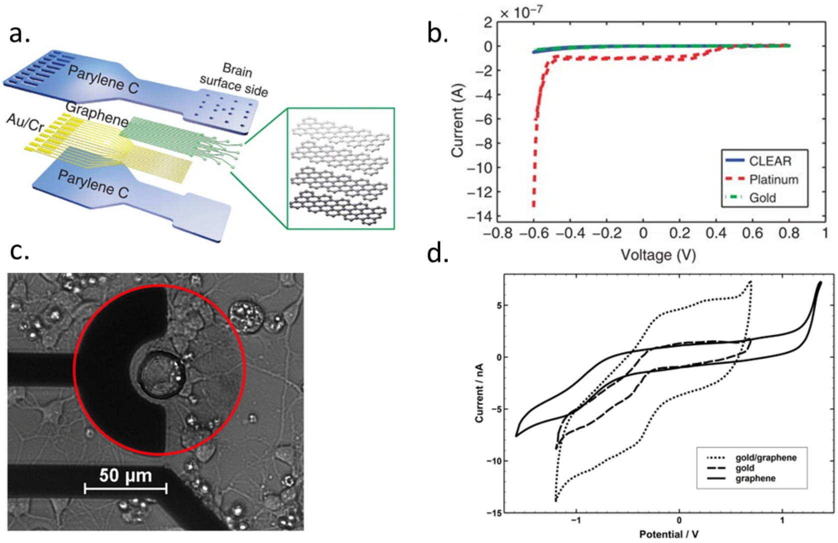

Figure 2.9: (a-b) Diagram of the four-layer graphene device (called CLEAR), and average CV results of CLEAR, gold and platinum micro-ECoG arrays (16 electrode sites) [3], (c-d) Transparent graphene electrodes with neuronal cells. The graphene is visible as a dark shadow around the black-appearing gold circuit path. The red circle indicates the area covered by graphene and CV results of gold, gold/graphene, and plain graphene electrodes. [47]

Wang et al. also fabricated graphene-fiber- (GF) based microelectrode arrays with a thin platinum coating and insulated them with parylene-C [26], illustrated in Figure 2.11. The combined impact of the two materials resulted in a more robust and better-performing device than graphene electrodes or platinum electrodes, differing by order of magnitude [26], [52], [53]. The fabricated graphene-fiber-based microelectrode arrays with a thin platinum coating (GF-PT) and insulated with parylene-C were found to have a CSC of 946 $\pm$ 140 $mCcm^{-2}$, two orders of magnitude higher than the unmodified graphene fibers, and a significant increase compared to platinum fibers. Additionally, the CIC of the GF-PT microfiber at 10.34 $\pm$ 1.5 $mCcm^{-2}$ was found to be approximately two times larger than its unmodified graphene counterpart [26].

In the subsequent research of these graphene-based fiber electrodes, Gonzalez-Gonzalez et al. used the platinum-coated porous graphene oxide (rGO) fiber to interface multiple splenic terminal

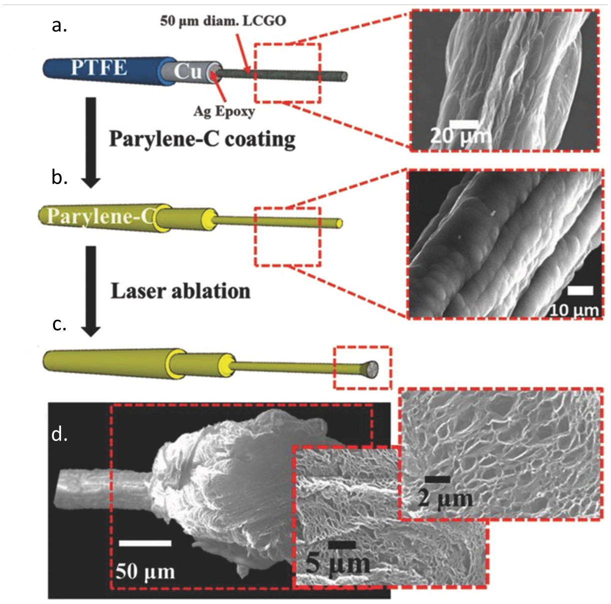

Figure 2.10: Fabrication and imaging of LCGO brush electrodes. (a) LCGOs are attached to PTFE (insulated) insulated copper wires (≈. 1 mm diameter) using conductive silver-based epoxy, followed by (b) parylene-C coating, (c) Laser ablation with 250 mW which opens the electrode end, creating a "brush" electrode, (d) Laser treatment leads to an amorphous electrode with extraordinary surface roughness and porosity. [51]

branches [54]. These electrodes were utilized as overhand knot suture electrodes over the small splenic neurovascular plexus, allowing sensitive recordings from these branches. A specific pattern of electric stimulation in the subdiaphragmatic vagus nerves increased the activity of the spleen, and another pattern reduced it, giving the possibility to neuromodulate the spleen directly [54]. Therefore graphene neural electrodes can be made into fiber-like structures surface-modified and interfaced with platinum to improve its stimulating and recording properties for a unique approach to neuromodulation techniques.

2.5. Surface Functionalization of Graphene for Neural Applications

The fiber-like devices described in Section 2.4.3 do not utilize the transparency of graphene for multi-modal imaging, recording, or stimulation. However, their strategies for enhancing graphene's recording and stimulating capabilities are founded by increasing the electrode's surface area by roughening it or interfacing it with another conductive material, such as platinum. Consequently, there is some interest in investigating these methods for transparent planar graphene electrodes. However, current research focuses heavily on doping transparent graphene electrodes with nitric acid (HNO_3) to lower their sheet resistance [4]. While other researchers have been focused on coating graphene with a conductive function polymer [50].

When the graphene surface is exposed to nitric acid, the adsorption of the electropositive NO_3^- groups leads to p-type doping. Kuzum et al. reported an improved electrochemical impedance from undoped graphene, although its value was not explicitly mentioned. Doped graphene and gold exhibited comparable impedance at 1 kHz, while graphene's impedance was significantly lower at lower frequencies, resulting in superior noise suppression when neural recording measurements were done *in vivo* (see a-c of Figure 2.12) [4].

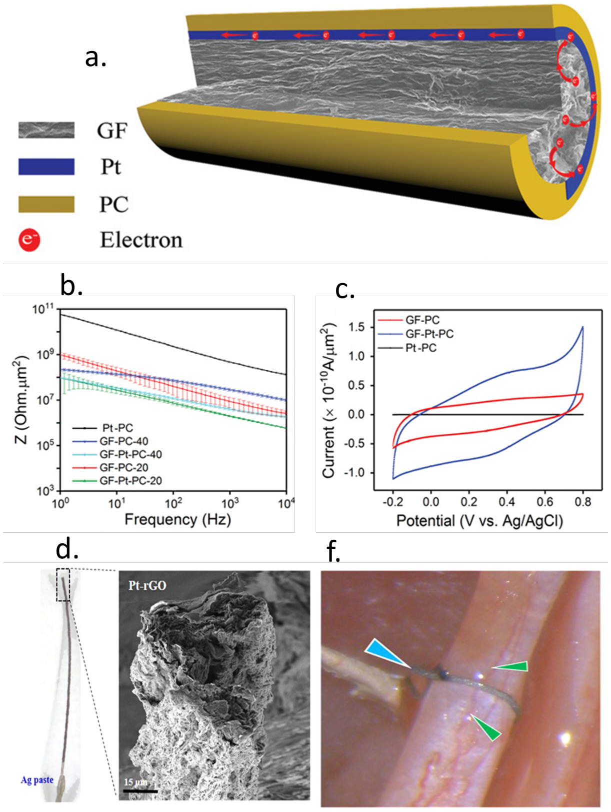

Figure 2.11: (a-c) Graphene fiber with platinum coating electrodes [26], (a) Schematic image of the GF-Pt microelectrode, (b) EIS results of various microelectrodes made from Pt, graphene microfibers, and Pt coated graphene microfibers (diam. = 20 and 40 μm), (c) Cyclic voltammograms of the microelectrodes at a scan rate of 10 mVs^{-1} in PBS solution [26], (c) Pt-rGO electrodes with SEM image (Pt coating ≈200 nm thick) (e) Pt-rGO electrodes wrapped around the sciatic nerve (blue arrow) [54]

Table 2.2: Properties of Functionalized Transparent Graphene Electrodes

Electrodes	**Type**	**CSC (μCcm^{-2})**	**Electrode surface area (μm^2)**	**Water window (V)**	**Impedance at 1 kHz (kΩ)**	**Area-normalized impedance (Ω.cm^2)**	**Optical Transmittance at 550 nm**	**Reference**
Monolayer graphene (Doped with HNO_3)	Total	1953 at 0.2Vs^{-1}	2500	−0.8 to 0.8	541	13.5		Kuzum[4]
2-layer Graphene (Doped with HNO_3)	Cathodic	22.4 at 0.5 Vs^{-1}	2500	−0.8 to 0.8	908 ± 488	22.7 ± 12.2	≈90% (with parylene both sides)	Driscoll[46]
Graphene (Doped with HNO_3)			2500		872	21.8		Liu[16]
Graphene (with Pt NPs; 30 s deposition)			10000	−0.9 to 1	≈10	1	>50%	Lu[28]
Monolayer Graphene (with 1 s PEDOT:PSS)			707		166± 13	1.17± 0.09	≈84%± 4%	Kshirsagar[50]

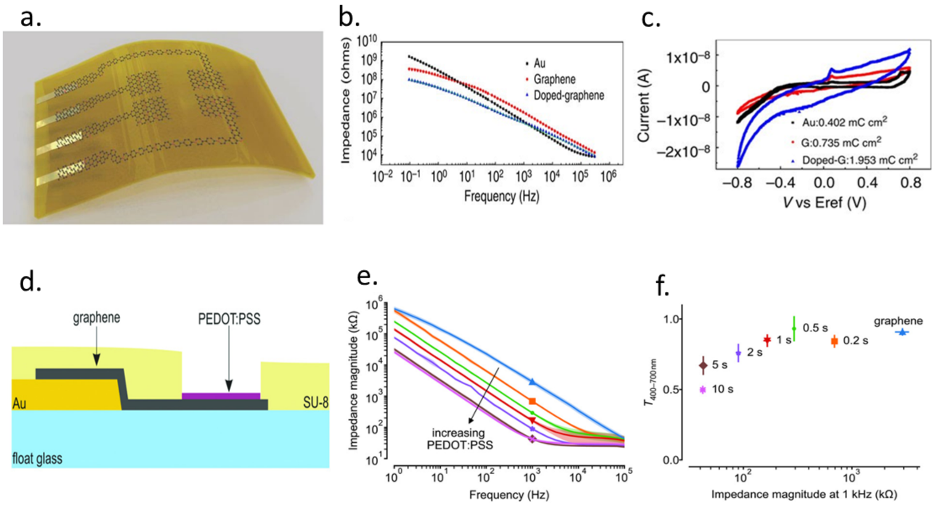

Figure 2.12: (a-c) Data on HNO3 doped-graphene [4], and (d-e) PEDOT:PSS coating on graphene. (a) Schematic illustration of a flexible graphene neural electrode array. Patterned graphene electrodes are in contact with Au contact pads to interface with the data acquisition system, (b) EIS results of Au, G, and doped-graphene samples (50 × 50 μm2), (c) Cyclic voltammogram showing improved total CSC for doped-graphene electrode. [4], (d) Schematic cross-sectional image of transparent graphene/PEDOT:PSS microelectrodes, (e) EIS results of bare and coated graphene electrodes (deposited for 0.2–10 s). The shaded areas correspond to the standard deviation on averaging. b) Transmittance versus impedance magnitude at 1 kHz for bare and coated electrodes. The transmittance values are averaged across the microelectrode (≈5–10 microelectrodes for every electrodeposition time) [50]

Driscoll et al. investigated the effects in impedance and CSC of 2-layer graphene doped with HNO_3 [46]. The doped graphene showed lower impedance at 1 kHz (908 ± 488 kΩ) compared to the undoped counterparts (2160 ± 230 kΩ). Its CSC was also higher at 22.4 μCcm^{-2} than the undoped graphene at 15.9 μCcm^{-2}. Their doped graphene device also showed >90% optical transparency across the visible spectrum (λ= 400 nm to 900 nm) [46]. Thus, this suggests the promising idea of improving graphene's recording and stimulating capabilities through such chemical treatment. However, an attempt to investigate this with similar multilayer graphene electrodes and fabrication processes as this research was unsuccessful in improving the impedance [55].

Conductive functional polymers such as PEDOT: PSS can also improve graphene's electrochemical properties. Monolayer graphene was fabricated with CVD and then coated with PEDOT: PSS for 1 second. The results showed a significant decrease in electrochemical impedance at 1 kHz (166 ± 13 kΩ) compared to the uncoated graphene samples of the same geometric size (Z ≈ 3000 kΩ) [50]. The transparency of the 1-second coated graphene was observed at 84%. Also, increasing the coating thickness by increasing the coating time further improved the impedance at the cost of transparency with observable differences between the time-sensitive deposition (see Figure 2.12) [50]. The CSC and CIC were not investigated for these samples.

Additionally, there is research that investigated the effects of platinum nanoparticles (Pt NPs) on graphene electrodes, taking advantage of the high surface-to-volume ratio of nanoparticles and the excellent electrochemical properties of platinum. A significant impedance decrease was observed from 872.9 kΩ at 1 kHz for monolayer graphene to approximately 10 kΩ for monolayer graphene with Pt NP coated for 30 seconds [28]. Different coating times also resulted in different nanoparticle surface densities, consequently showing other electrochemical properties, and transparency [28]. The cyclic voltammograms were presented, but the CSCs were not reported, and the CIC was not investigated. However, the increasing cyclic voltammograms of the research demonstrate improvements in the CSC (see Figure 2.13), and thus, it is promising to investigate the effects of the density of platinum nanoparticles on graphene's CSC and CIC.

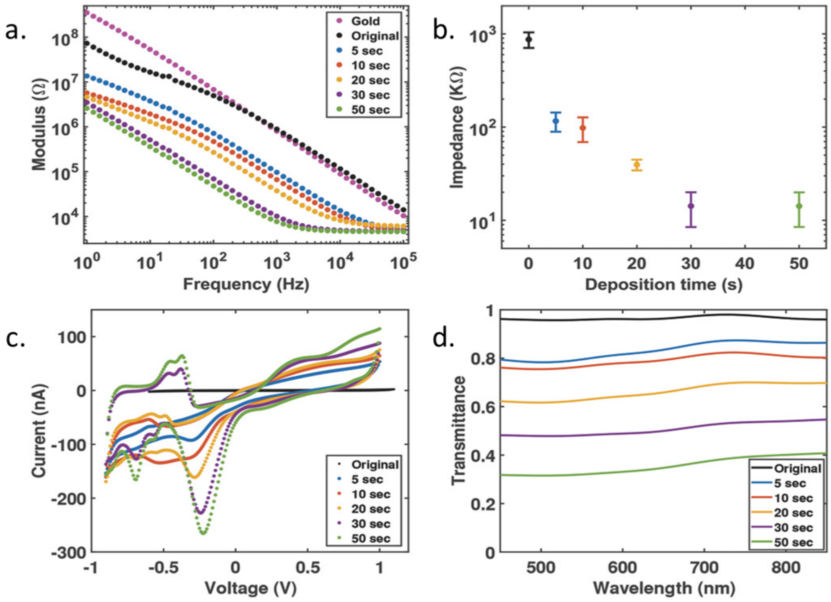

Figure 2.13: (a) EIS results of bare graphene electrode (black dots), gold electrode (magenta), and Pt NP/graphene electrodes from 1 Hz to 100 kHz, (b) The impedance versus deposition time at 1 kHz with decreasing trend with deposition time, (c) Cyclic voltammograms of bare graphene and Pt NP/graphene electrodes with a sweep rate of 200 mVs^{-1}. Bare graphene electrode without Pt NPs (black) has no faradaic peaks, and the current is very small, and hence the curve looks like a straight line, (d) Transmittance spectra of Pt-Np/graphene electrodes from 450 to 850 nm wavelength. [28]

Increasing the surface-to-volume ratio of the sensing element improves electrode performance. The effective surface area can be increased by roughening the electrode surface or adding a thin conductive porous coating. However, the stability of the additional layer then plays a role in the long-term functionality of the device. Poor film adhesion restricts the mechanical robustness of an implanted device, which compromises the sensor's electrochemical performance due to the possibility of early delamination, reducing electrode lifetime. Hence, the investigation of the stability of the coating layer is critical for a well-functioning neural electrode device. There are multiple ways to investigate this, such as aging tests for simulating stability over chronic implantation, continuous VT tests, or continuous charging and discharging cycles through CV to simulate chronic stimulation can be performed. At the same time, EIS, and CV with optical imaging before and after attempts can indicate changes in the electrode-electrolyte interface by visual inspection of induced defect or damage on the electrode and its coating.[23].

2.6. Nanoparticle Synthesis for Neural Devices

Nanoparticles (NPs) are solid colloidal particles that range from 10 to 1000 nm (1 μm). They have been utilized for biomedical devices for numerous applications, owing to their physical and chemical properties that differ from their bulk counterpart because of the Nps' high surface area-to-volume ratio. NPs are used for biomedical applications as drug carriers of targeted drug delivery, hyperthermia, cell labeling, magnetic resonance imaging contrast agents, and biosensors (including neural electrode devices) [56].

Platinum nanoparticles (Pt NPs) for neural electrode applications are produced by electrochemical reduction of commonly available platinum salts, known as precursors. Commercially available platinum salts are hexachloroplatinate ($[PtCl_6]^{2-}$) and tetrachloroplatinate ($[PtCl_4]^{2-}$). Whereas, electrodeposition is the process of depositing material on a conducting surface using electric current from a solution containing ionic species. During electrodeposition, platinum ions are converted to solid-state platinum, resulting in cathode deposition. The amount of the deposited film can be tuned by adjusting different parameters such as the temperature, applied current density, electrolyte content, etc.

In the work by Lu et al, platinum NPs on graphene electrodes were deposited from an electrolyte solution containing 5 mM H_2PtCl_6 and 10 mM K_2HPO_4 and deionized water. Current pulses between the graphene electrode and a platinum electrode led to the deposition of Pt NPs on the cathode (graphene). By varying the time period of the current pulse, the density of the NP coating was optimized, leading to a 14.65%, 67.27%, 88.22% coverage from 5, 20, 50 seconds current pulse, respectively (I = 500 nA). The deposition and coverage of the Pt NPs were validated through scanning electron microscopy (SEM) imaging [28].

Moreover, the platinum nanostructures can also be deposited passively. In the work by Boehler et al., platinum nanostructured grass (Pt-nanograss) was grown on a substrate through a diffusion process and then compared with electrodeposited Pt-nanograss [57]. For both the passive and active deposition methods, an aqueous solution of 2.5 mM H_2PtCl_6 and 1.5 mM formic acid (HCOOH) was prepared. For the passive deposition, the electrode was placed vertically in the solution, and the deposition was conducted at room temperature for 48 hours. The reduction reaction was complete when the solution changed color from yellow to clear. The electrode side showed a black coating, revealing a successful formation of the Pt-nanograss. However, the nanostructures were also observed on the insulating layer which may short circuit with another electrode, requiring further post-processing. Cleaning the undesired layer by wiping it off with a wet tissue or by sonication in a water bath for 30 minutes proved efficient in removing the excess.

Conversely, the active deposition process used a three-electrode cell configuration in the H_2PtCl_6 with a formic acid solution. The bare platinum electrode, the target surface for the nanostructures, was used as the working electrode, a stainless steel electrode as the counter, and Ag/AgCl as the reference. The deposition was achieved potentiostatically at -0.1 V vs Ag/AgCl for 300 s, resulting in the Pt-nanograss formation only on the electrode site. Although both processes successfully deposited the Pt-nanograss, SEM and Focused Ion Beam (FIB) imaging showed unique topography. The passive method resulted in a more significant aspect ratio than the electrodeposited Pt-nanograss (see Figure 2.14); however, this effect was not further investigated, but another study showed how Pt-nanowire growth could be controlled and made uniform through slow reduction rates [58].

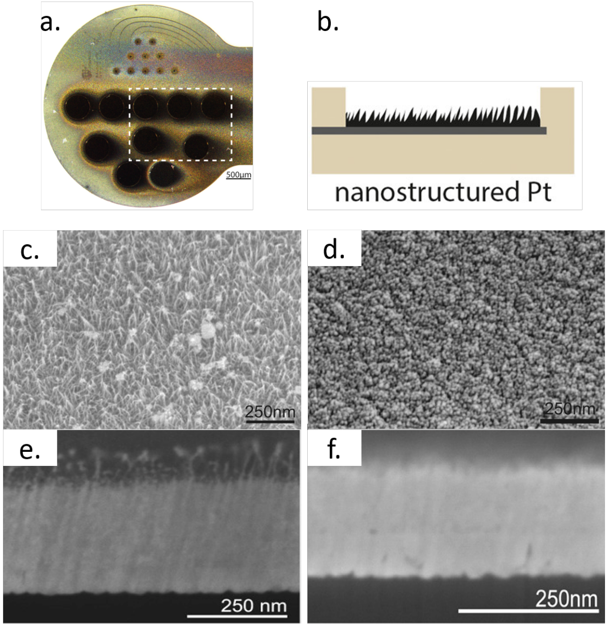

Figure 2.14: (a) Optical image of the passively deposited Pt-nanograss, (b) Cross-sectional schematic of the Pt-nanograss with polyimide sidewalls. And SEM images of the passively deposited Pt-nanograss (c,e) with higher aspect ratio than the actively deposited Pt-nanograss (d,f). [57]

Furthermore, pulse laser ablation in liquid (PLAL) can also synthesize nanoparticles, and an electrodeposition process facilitates the coating of the electrode surface. In the works of Angelov et al., and Koenen et al., Pt NPs were synthesized by PLAL through a self constructed chamber and then coated through electrodeposition [59], [60]. During their PLAL process, a laser beam (λ= 1064 nm) is focused on a bulk target (such as a plate) of the desired material, effectively ablating the material into the deionized water. This was further processed by centrifugation for particles approximately < 10 nm, creating a colloid solution and then later deposited through electrodeposition. However it was observed that this process induces nanoparticle assemblage when the electric field strength and colloid concentrations are >25 Vcm^{-1} and >250 μgmL^{-1}, respectively. Despite the promising pure Pt NP coating, the complete procedure is more complicated than direct coating from chemical reduction. Additionally, continuous laser ablation on a single spot depletes the bulk material. There will eventually be a need to reposition the laser to a different area in the bulk material to synthesize more Nps, disrupting the continuity of the process.

Regardless of how the nanoparticles are created, electrodeposition is a proven method of coating surfaces such as platinum and graphene with Pt NPs. However, the nature of the deposition process is contaminating because the electrode is also exposed to other ionic species. This process also produces waste by the solvent byproduct, thus environmentally harmful. Hence, there is a need for a dry NP deposition process such as spark ablation.

2.6.1. Spark Ablation

Spark ablation (SA) is a method to produce nanoparticles by abruptly creating electrical discharges between two electrodes. A spark of electricity generates plasma, which removes a small amount of material from the electrode of conductive or semiconductive material. When the material is ablated, a strong stream of nanoparticle aerosol is made, and the carrier gas flows through the electrode gap region. The atomic clusters combine to form larger particles while transported to an outlet. This is possible through a spark discharge generator (SDG), also called a spark ablation generator or spark generator [61].

The final step of the procedure is particle deposition using one of three deposition techniques: diffusion, filtration, or impact deposition. Diffusion deposition occurs when particles collide with and adhere to a substrate due to random motion. Filtration removes particles from a gas stream using a porous substrate. In impact deposition, particles are accelerated and fired onto a substrate [61]. Therefore, impact deposition was chosen for this study because it is the most easily controlled, needing simply modifications to the process parameters without the requirement for a filter or the randomness of diffusion.

SDG is a unique instrument for creating particles with controlled composition since short sparks allow the formation of internally mixed particles whose composition is defined by the electrodes. Additionally, short sparks produce particles smaller than 20 nm in diameter and atomic clusters. Each spark forms a millimeter-sized vapor cloud quickly mixed with an inert gas flow. Cooling from mixing causes vapor supersaturation and spontaneous condensation, producing atomic clusters that agglomerate into bigger particles. Changing the gas flow alters the time particles coagulate, regulating particle size . Additionally, sophisticated spark generators allow for the control of the spark energy which determines the amount of material that is evaporated from the electrode by each spark. This is achieved by adjusting the distance between the electrodes as the material depletes over time [61]. Figure 2.15 presents a schematic of a commercially available SDG.

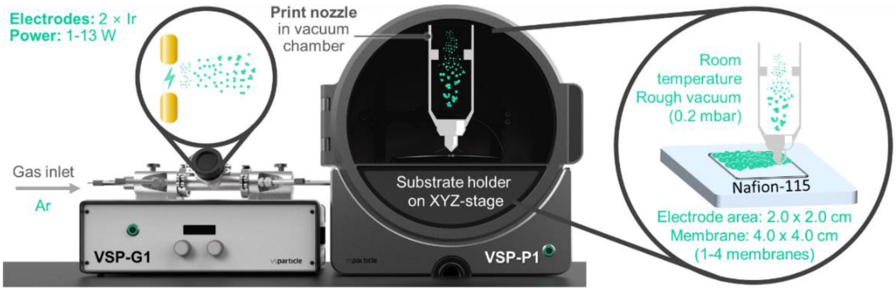

Figure 2.15: A schematic of the VSP-P1 Nanoprinter with the VSP-G1 Nanoparticle generator for the fabrication of spark-ablated catalyst coated membranes [62]

2.7. Summary of the Literature Review

Integrating optogenetics, electrophysiology, and calcium imaging might yield new insights into the functioning of brain circuits. There have been numerous advances in transparent electrode devices that can complement simultaneous optogenetics and imaging modalities. However, some challenges limit the electrode device's design and material, including flexibility, transparency, low impedance, high CSC, and high CIC, among others.

Transparent graphene arrays enable simultaneous electrophysiology and two-photon imaging of neural activity, providing high spatial and temporal resolution. However, its impedance is higher and CIC is much lower than platinum, a metal used for conventional electrophysiological recording and stimulation. There have been numerous attempts to improve the electrochemical characteristics of planar transparent graphene electrodes by chemical doping with nitric acid or surface functionalization with conductive coatings like platinum nanoparticles. An attempt to investigate nitric acid doping with similar multilayer graphene electrodes and fabrication processes as this research were unsuccessful in improving the electrode impedance [55].

Therefore, platinum nanoparticle coating by spark ablation is a promising surface functionalization technique for this research's transfer-free graphene microfabrication process. Moreover, the existing research platinum nanoparticles on transparent graphene electrodes has only been investigated for simultaneous electrical recording and optical imaging of neural activity [28]. There is currently no quantitative evidence of the extent to which platinum nanoparticles can impact the stimulating properties of transparent graphene electrodes and any indication of the stability of the coating.

3

Methodology

This chapter presents the device design and the complete fabrication process of the graphene electrodes, including the nanoparticle synthesis and deposition process. The methodology used for the material characterization is also presented. It details the optimization procedure of the nanoparticle deposition used to acquire distinct surface densities of the nanoparticles and the methods used for the optical transmittance and the roughness characterization tests. The last part of the section describes the electrochemical characterization tests. This subsection includes the three-electrode setup, EIS, CV, VT, and the stability and adhesion tests of the graphene and Pt NPs.

3.1. Device Design and Fabrication Process

This section describes the microfabrication process of the graphene electrode. Since this research focuses on improving the electrochemical characteristics of graphene, the devices sit atop a silicon substrate instead of a flexible one like parylene-C, simplifying the fabrication process. However, the full realization of this device design is similar to that of Babaroud's samples where the graphene is released through a deep reactive ion etching process from the backside of the silicon wafer [15].

3.1.1. Fabrication Process and Mask Design

The fabrication process started with a single-side polished, 500 μm thick, four-inch silicon wafer, and all methods used were processed on the wafer's front side. The first part of the fabrication is the creation of the zero layer. In this step, alignment markers on the silicon were etched and can be found at the sides of the wafer. The wafer was coated with Shipley SPR3012 positive resist and then patterned through the ASML PAS5500/80 automatic wafer stepper. The zero layer was dry etched through the Trikon Omega 201 plasma etcher.

Once the zero layer is complete, approximately 300 nm thick silicon dioxide is grown on both sides by wet oxidation at 1000°C. Then, the molybdenum is deposited up to 50 nm thick at 50°C through the TRIKON SIGMA sputter coater. It was then coated with the AZ ECI 3027 positive photoresist and the photoresist was patterned with the SUSS MicroTec MA/BA8 mask aligner (also known as a contact aligner). This pattern defines the structure of the molybdenum from which the graphene is grown. Hence, the mask used is called the **BE2325-GRAPHENE**, a bright-field chromium mask [63]. The final pattern of the molybdenum was revealed after a 30-second dry etching process and the remaining photoresist layer was stripped off through an oxygen plasma exposure with the Tepla Plasma 300 system. Following this step, the graphene was grown by a low-pressure chemical vapor deposition (LPCVD) process using the AIXTRON BlackMagic Pro at a temperature of 935°C and 1050°C at the bottom and top heating element, respectively. This step started with a 20-minute annealing of the molybdenum, and then the methane (CH_4) precursor flowed into the chamber for 20 minutes.

Furthermore, a titanium and aluminum layer was sputtered using the Trikon Sigma coater. The metal layer was coated manually with the AZ ECI 3027 photoresist and exposed with the contact aligner using

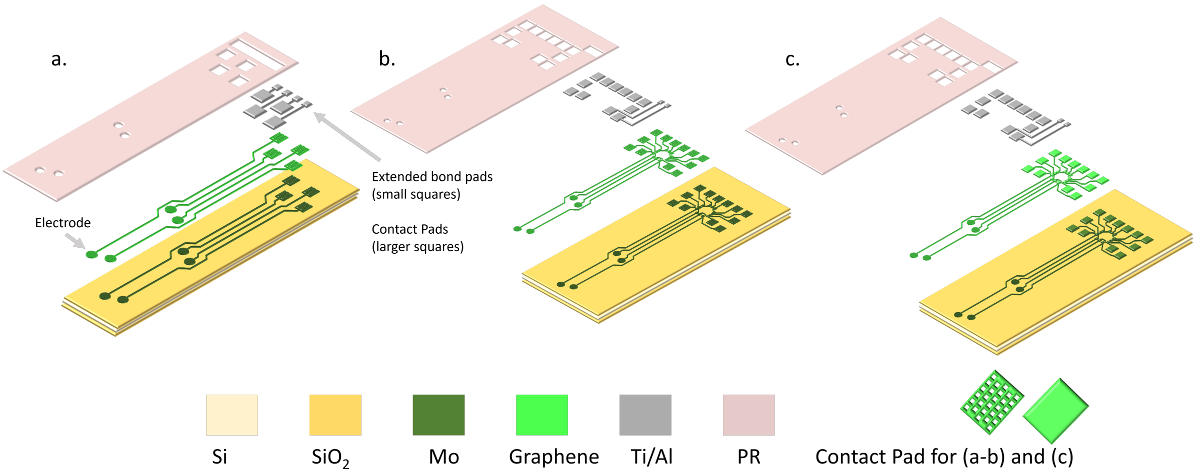

Figure 3.1: All layers of the graphene electrode devices. Device (a) has an extended bond pad connection to all four electrodes, and (b-c) to only two electrodes

a bright-field foil mask labeled **METAL**. This mask is a modified version of the same name originally designed by Velea [63]. The pattern for the metal layer on top of the graphene electrode was removed on this modified mask, and the pattern of the contact pads of the device and their extended bond pads were added, which were used for wire-bonding. A hard bake of 30 minutes at 115°C was performed on the process wafers before etching the metal in 0.55% hydrofluoric (HF) acid for approximately 13 minutes.

The last layer of the device is the insulation layer which was patterned through a dark-field foil mask called **PDMS openings**. Despite the mask's name, the insulation layer used for these devices is the AZ ECI 3027 photoresist, simplifying the patterning process with a contact aligner exposure and manual development process using the Shipley MF322 developer. The insulation layer protects the bulk of the device while the graphene, contact pads, and extended bond pads are exposed for further processing. Figure 3.1 presents each layer of the device from the SiO_2 up to the PR insulation. Figure B.1 and Figure B.2, found in the appendix, show the complete wafer-level fabrication process.

Further processing was performed at the die-level, such as etching away the molybdenum underneath the exposed graphene, printing Pt NPs on some graphene electrodes, and wire-bonding the devices onto a PCB for a stable connection throughout the electrochemical measurements. Only the electrode end of the device was submerged into the hydrogen peroxide (H_2O_2) solution. Immediately after the etching process, the devices were submerged in water to rinse and then set aside to dry. Illustrated in Figure 3.2 and Figure 3.3 are the top and cross-sectional view of the graphene electrode before and after etching the Mo.

3.1.2. Settings and Parameters for Platinum Nanoparticle Printing

Following the fabrication of the graphene devices, Pt NPs were printed on some of the exposed electrodes using the VSP-G1 nanoparticle generator connected to the VSP-P0 nanostructured material printer (VS Particle). The Pt NPs were printed at five different speeds to get four distinct surface densities: 137 mm/min, 67 mm/min, 38.3 mm/min, and 21.5 mm/min, printed through one pass, and some samples had similar surface density with 67 mm/min but printed through 2 passes with a higher speed, 141 mm/min. The final settings used for the samples are presented in Table 3.1, and these settings were results from an optimization procedure described in subsection 3.2.3.

Printing over the electrode was performed one electrode at a time, and the x-y planes were calibrated for each print. Additionally, the z-axis, which affects the printing height, was calibrated at the start of the batch printing process. The z-axis calibration was performed by determining the touch point, which is the height from the tip of the nozzle to the chamber stage. It can also be described as the

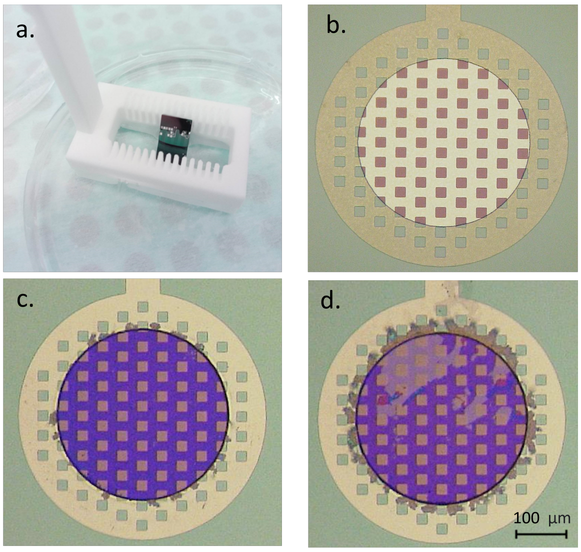

Figure 3.2: (a) Setup of die-level Mo etching with H_2O_2. *Only the electrode-end is submerged,* (b) An electrode before Mo etch. *Pink squares are exposed* SiO_2. *Negative space is graphene on Mo* (c) An electrode after a successful Mo etch and (d) A damaged graphene layer after the etch, which was discarded

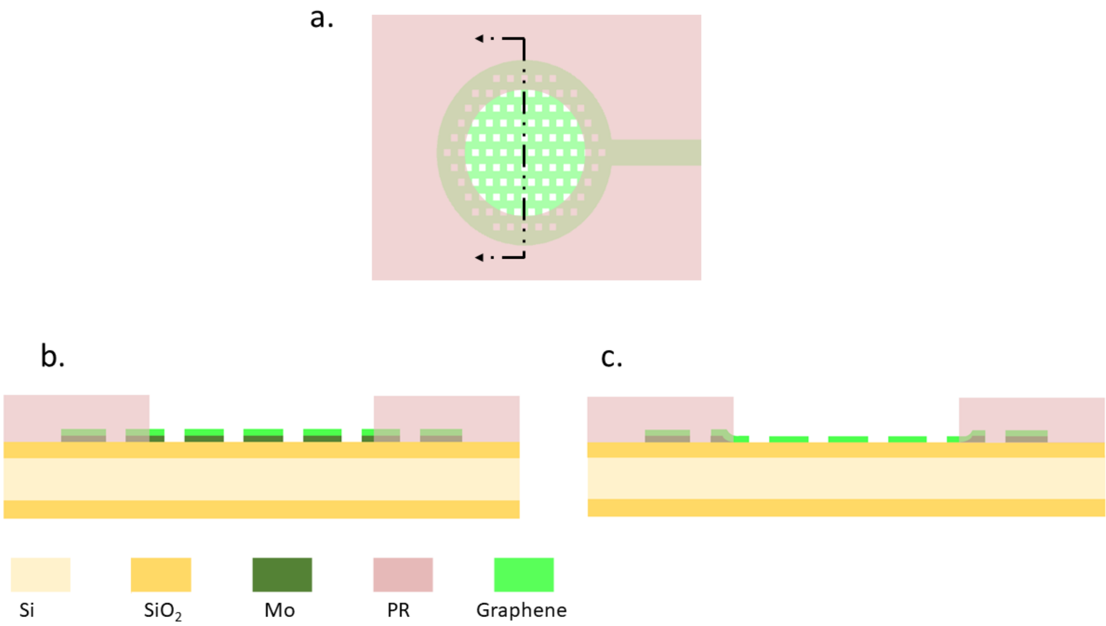

Figure 3.3: (a) Reference of the cross-sectional view of image b and c (b) Schematic of a cross-sectional view of the electrode with molybdenum and (c) cross-sectional view of the electrode after Mo etching. *PR-photoresist*

distance at which the stage is in focus with the connected camera. The nozzle is moved to a distance of 0.925 mm above the touch point, providing a consistent starting point for all samples. As the printing script is executed, the nozzle moves down from the starting point to the printing height before any release of NPs.

In some cases, the nozzle had to be cleaned and removed between sample printing, possibly altering the z-axis calibration for that batch printing when the nozzle is not returned at the same height relative to the chamber stage. Hence, another z-axis calibration is performed after every declogging procedure of the nozzle. The z-axis calibration is critical for the precise deposition between each batch and sample printing. For every attempt at calibrating the z-axis, lines according to the desired density were printed on a bare silicon die. Each density was verified via SEM imaging and image thresholding described in Section 3.2.2.

Before the start of the printing process, the devices were placed laterally along the x-axis, shown in Figure 3.4. After all the necessary calibration procedures are completed, a 3 mm line was printed, going over the approximate center of the graphene electrode. The line started and ended on the PR insulation layer. Figure 3.4 also presents an example of a printed electrode. Furthermore, attempts to print only on the electrode sites were unsuccessful because starting the print process resulted in a large burst of NP deposits due to the gas build-up in the spark generator, resulting in densities higher than desired. For this reason, line printing was chosen, where the sudden burst is offset from the electrode site. Section 3.2.4 describes the techniques for calculating the deposition width. This procedure confirmed that the width of each printing speed (for the necessary density) was greater than the diameter of the exposed graphene electrode, further establishing the practicality of line printing as it can fully cover the graphene through one line pass.

Moreover, some printing lines deviated, and the full graphene coverage with NP was not achieved, likely due to the x-y axis misalignment or the machine's motor control error. Only the electrodes fully deposited with Pt NPs were used for the electrochemical characterization. Full coverage of the graphene electrodes with NP can be observed in two ways: confocal microscopy (Keyence VK-X250), and SEM imaging (SEM Hitachi Regulus 8230). There is a visible color difference between the exposed graphene and SiO_2, shown in Figure 3.5, but this was difficult to verify at lower NP densities. On the other hand, the SEM confirmed all NP deposition over the electrode. At a low-magnified view, the print path is visible, and a high-magnified view was used for NP verification when the print path is not centered over the electrode site.

Table 3.1: Parameters and Settings Used for Pt NP Printing

Printing Height	0.5 mm	
Nozzle Size	0.35 mm	
Carrier Gas Flow	1.5 L/min	
Carrier Gas	Nitrogen	
Gap Voltage	1 kV	
Spark Current	3 mA	
Printing Speed (mm/min)	**No. of Passes**	**Deposition Width (μm)**
137	1	526
67	1	554
141	2	542
38.3	1	637
21.5	1	680

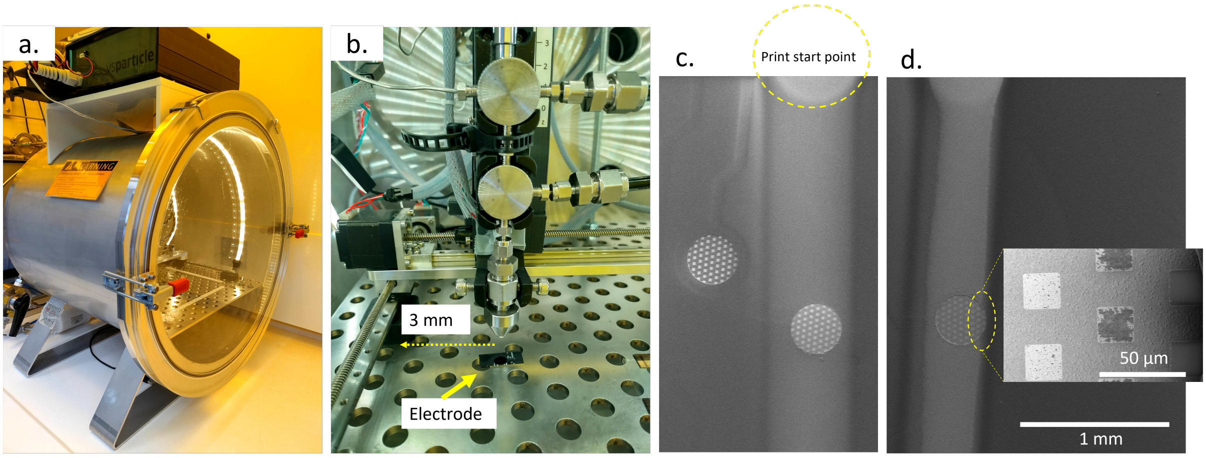

Figure 3.4: (a) Printer chamber (b) The setup inside the chamber for the Pt NP printing process. The printer nozzle head moves 3 mm and goes over the electrode, (c) A graphene electrode without (left) and with (right) Pt NPs, and (d) a graphene electrode not fully covered with Pt NPs. The inset shows a magnified view of the electrode where the darker areas do not have Pt NPs

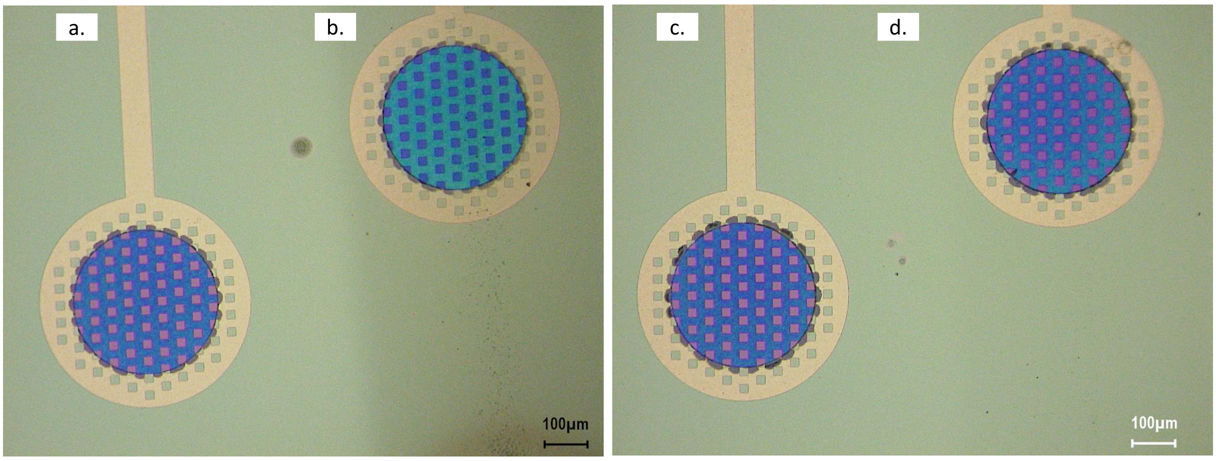

Figure 3.5: (a,c) Electrodes with only graphene, graphene with Pt NPs printed at (b) 21.5 mm/min, and (d) 38.3 mm/min

3.1.3. Preparation for wire bonding

One of this research's challenges is getting a stable electrical connection from the device to the potentiostat (Autolab) used for the electrochemical measurements. Previous attempts to characterize the electrodes used pasted silver wire over the contact pads [55]. This method had a more complicated sample preparation process, and the interfacial wire contact caused large variations in data. For this reason, aluminum wire bonding was utilized to make an electrical interconnection from the device to a right-angle male pin header (Harwin) soldered onto a printed circuit board (PCB). The pin header extended to four gold rectangular contact pads, one for each pin, as shown in Figure 3.6. Additionally, about 9.15 mm of free space was below the contact pads, and the device was mounted in that area using epoxy glue (Loctite Hysol M-31CL Medical Epoxy glue). Only the top part of the device was glued, while the electrodes stuck out from the PCB to be immersed into the electrolyte for testing.

Furthermore, wire bonding uses a capillary and ultrasound to bond the wire to the contact pads. It is necessary that these contact pads were flat and leveled. Since the pin header was mounted through the hole, the PCB could not be placed flat on a surface, leading to the device sliding up to the contact pad with uncured glue and in some cases covering the pads. These PCBs were then discarded. Because of this, a mount was designed where the PCB could sit flat, and the device had the support that brought it leveled onto the PCB, as shown in Figure 3.7. The structure has two final versions: single-device mounting and three-device mounting.

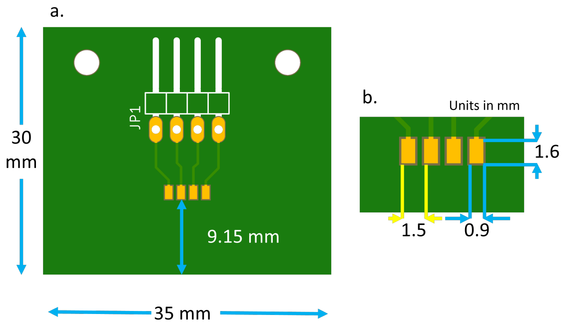

Figure 3.6: Schematic diagram of the (a) PCB and (b) contact pads for wire bonding on the PCB

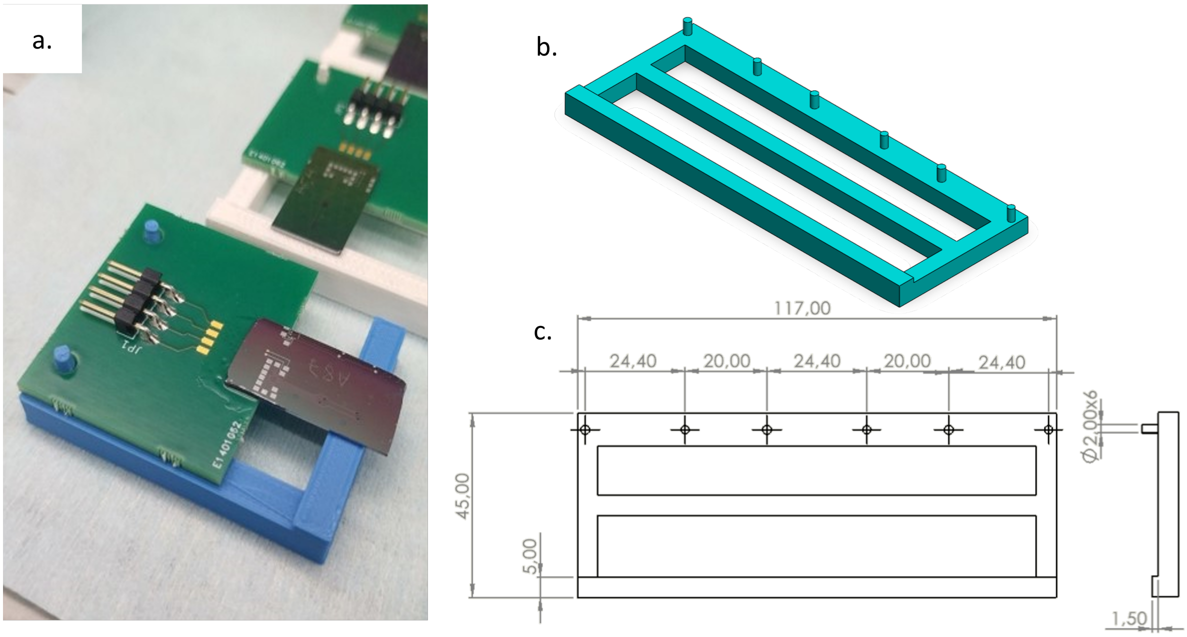

Figure 3.7: (a) Single-device mounting setup, (b) Three-dimensional model of the setup of the three-device mount and (c) Top view and side view technical drawing of the model, respectively. The units are in mm, and the image is not scaled

3.1.4. Tools and Parameters for wire bonding

Once the epoxy has cured, the device is ready for wire bonding. Aluminum wires (33 μm diameter) were bonded using the TPT semi-automatic wedge bonder. The first bond is on the contact pads of the PCB and the second is on the device. Bond 1 used an ultrasound power of 350 mW with a force of 400 mN for 400 ms, while bond 2 used 400 mW ultrasound power, 350 mN force for 350 ms. The bond pads of the device are shown in Figure 3.9. Figure 3.8 presents an SEM image of the wire bond. The lengths of the wire varied depending on the distance of the contact pads. After wire bonding, the whole length of the wires and the bond pads were insulated with PDMS by cautiously drop-casting over them. The devices used in this research have 2 or 4 electrodes that are each connected to an extended bond pad for wire bonding. Hence these devices can be measured electrochemically.

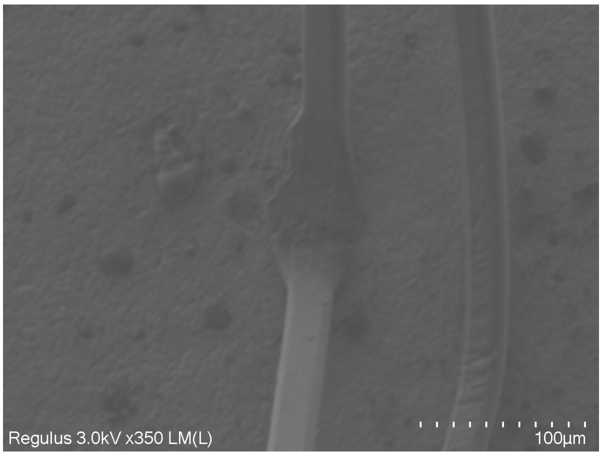

Figure 3.8: SEM image of the aluminum wire bonded (left) on the PCB contact pad and an aluminum wire not bonded (right)

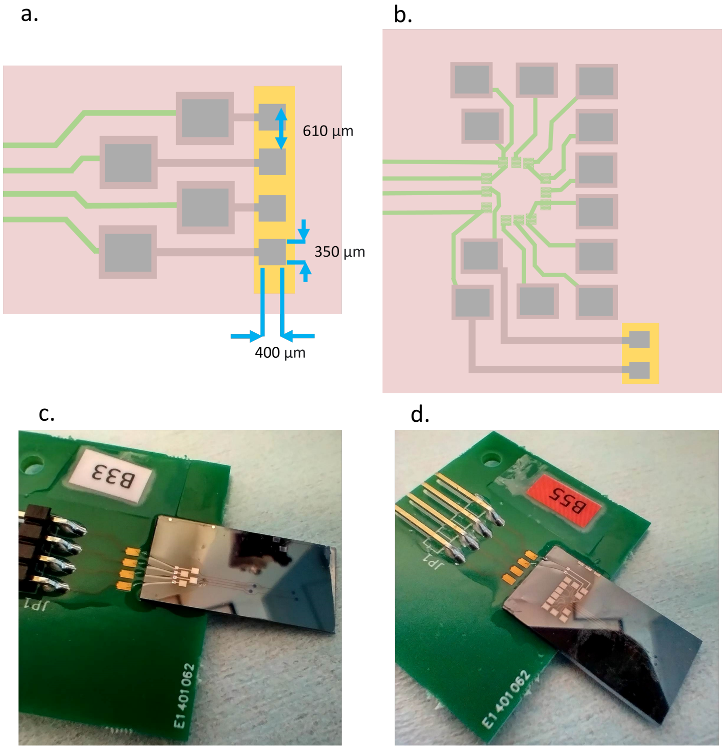

Figure 3.9: (a-b) Schematic diagram of the bond pads. *Measurements of (a) is the same for (b)*, (c-d) Examples of the wire bonded devices insulated with PDMS

3.2. Material Characterization

This section describes the various material characterization methods used in this research, both for the Pt NPs and the graphene electrode. The first part of this section is the image thresholding method which was used for the calculation of the nanoparticle surface density, which was then used for the optimization of the nanoparticle printer settings and z-calibration of the printer tool (as mentioned in Section 3.1.2). The same image processing and thresholding method was used for the calculation of the deposition width of the Pt NPs, which verified that the width was large enough to cover the electrode, and also the width was used for preparing samples of the optical transmittance test. Furthermore, atomic force microscopy (AFM) characterized the surface profile of the Pt NPs, and the results from the Raman spectroscopy confirmed the presence of graphene after Mo etch.

3.2.1. Raman Spectroscopy

Raman spectroscopy is a spectroscopy method that offers information on the composition and structure of molecules. It is mainly used to examine the vibrational, rotational, and other low-frequency modes of a material. When a sample is exposed to a specific wavelength of light (such as a laser), the light interacts with the sample molecules and is either absorbed or scattered. Most of the light will be scattered in a way called Rayleigh scattering, which doesn't change the wavelength. Only one photon (a unit of light) in 105–107 photons will be scattered inelastically, which does change the wavelength (Raman scattering). This change in wavelength of the photon scattered by the sample's molecule is referred to as the ”Raman shift” and is unique to the molecules with which the incident light interacts. During Raman Scattering, the incident photon interacts with the molecule of the specimen under examination, resulting in an energy exchange; hence, the scattered photon might have more or less energy than the incident photon. This photon energy change is directly related to the vibrational and rotational energies of the molecule. Because these vibrational and rotational energies are particular to a chemical bond of the molecule, they can provide a unique spectrum of that molecule. Since Raman spectroscopy require little sample preparation and the measurements are performed non-destructively, it is a versatile tool for studying the properties of low-dimensional materials like graphene [64].

The graphene Raman spectrum has three distinct bands: the G-band, the D-band, and the 2D-band. The G-band peaks at approximately 1580 cm^{-1} (from a 532 nm excitation laser), representing the in-plane stretching vibrations of the sp2-bonded carbon atoms. The intensity of the G-band increases linearly as the number of graphene layers increases. The peak position of the D-band is ≈ 1350 cm^{-1}, and the 2D is observed at 2690 cm^{-1}. The peak intensity ratio of the 2D and G bands (I$_{2D}$ /I$_{G}$) can indicate the number of layers. For monolayer graphene, this ratio must be more than 1. The peak intensity ratio of the D and G bands (I$_{D}$ /I$_{G}$) characterizes the level of disorder in the graphene sample. The peak of the D-band highlights the defects in the sample, and higher observed intensity means a higher level of disorder [64].

For this research, the Raman spectrum of graphene was measured with a 514 nm argon laser using the Renishaw inVia Raman microscope. The measurement was taken from 1100 cm^{-1} to 3200 $^{-1}$ with a laser power of 10% and exposure time of 10 seconds. Raman spectroscopy was performed after Mo etch of the electrode to confirm the presence of graphene.

3.2.2. Image Processing and Thresholding for the Calculation of Nanoparticle Density

The densities were calculated using the images of the nanoparticles printed in a line, on a clean silicon die. The images were captured from a scanning electron microscope (SEM) (Hitachi Regulus 8230) and were taken with a 2 kV beam at 50,000x magnification. These were then processed using a custom MATLAB script in which they were loaded as an 8-bit image. The processed images are 1280 pixels wide and 880 pixels high, cropped from the original image of 1280 x 960, thus removing the embedded text and scale. The intensity range of an 8-bit data matrix is from 0 (black) to 255 (white); thus, it is in greyscale. Consequently, there is a frequency distribution of these intensity values, blurring the lines between the nanoparticles (foreground) and the silicon (background). Ultimately, needing an intensity limit to identify the boundaries of the nanoparticles.

One of the critical aims of image processing is the demarcation of objects in digital images. For this research, it is achieved with image segmentation which can be done through thresholding. Through this process, grayscale images can be converted into binary images by replacing the pixels with white whose value is above a threshold or set to black when it is below it. Otsu's method was used to achieve this.

Otsu's method is an algorithm that assumes that the image contains two classes of pixels: the foreground and the background. It then searches for the threshold intensity, which maximizes the between-class variance (σ_B^2) of the two using Equation 3.1 [65].

$$\sigma_B^2 = W_b W_f (\mu_b - \mu_f)^2 \tag{3.1}$$

In Equation 3.1, $W_{b,f}$ are the weights that are represented by the number of pixels in the background (or foreground) over the total number of pixels; while $\mu_{b,f}$ is the mean intensity of the background or foreground. Figure 3.10 shows the montage of an image of the nanoparticles before and after thresholding.

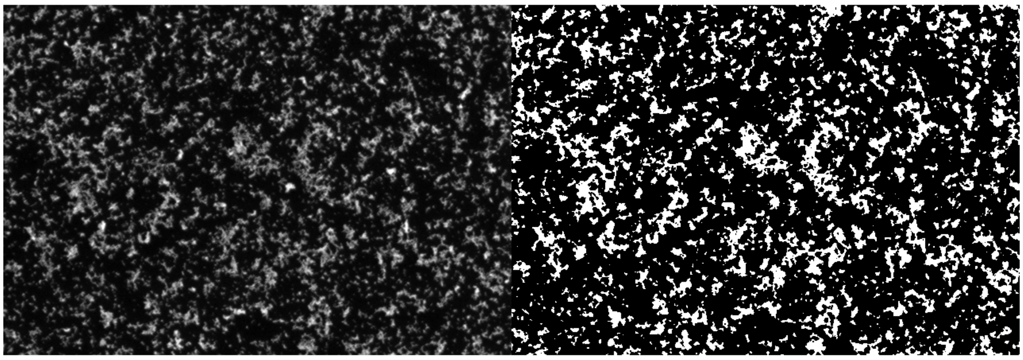

Figure 3.10: Grayscale image of platinum nanoparticles on silicon (left) and binarized image according to a threshold (right), where the nanoparticles are shown as white

The gray threshold intensity was determined using MATLAB's built-in function called graythresh(*I*), which computes the global threshold from a grayscale image *I* [66]. Another built-in function called imbinarize(*I*) creates the binary images from the grayscale image *I* according to the computed threshold [66]. The values exceeding the threshold are replaced with 1, representing the nanoparticles. The values less than the threshold are assigned as 0, and it represents the background. The custom MATLAB script uses the binarized data matrix of the images as it computes the percent area of white pixels (nanoparticles) over the total area of pixels which is then defined as the surface density.

Additionally, multiple images can be processed with the script where the thresholding is specific to every image's frequency distribution of intensity values. It is shown in Figure 3.11 that two similar images but with slightly different brightness and contrast changed the frequency distribution of the grayscale intensity values, resulting in a 130 and 113 threshold value, respectively. After processing the images, the surface density was calculated as 14.6% and 13.7%, with a minimal difference between the two. Hence, thresholding specific to every photo is essential to get a more precise representation of the surface density. Additionally, two images taken at different locations of the printed area also have a different frequency distribution of grayscale values because of the random deposition of nanoparticles. The gray threshold of the photo on the left of Figure 3.12 is 124, and the right is 133, unique to each. As a result, their surface densities are 21.3% and 21.6%, respectively, verifying the surface densities as comparable throughout the deposited area. This is shown in Figure 3.12.

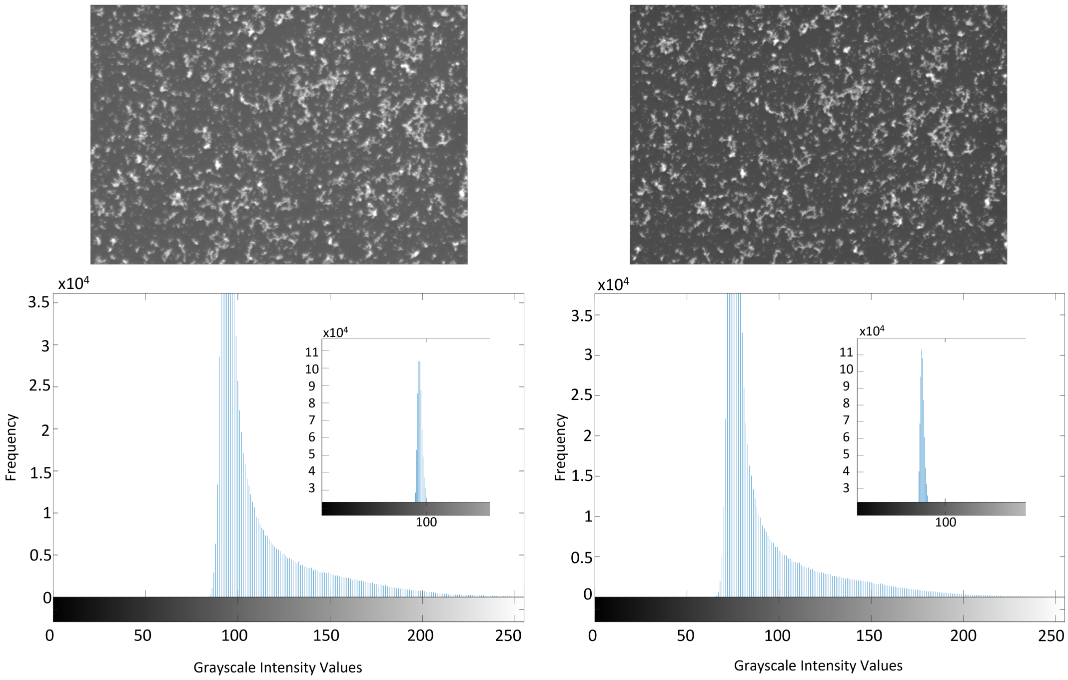

Figure 3.11: A comparison of the histograms of the same photo with slight brightness variation. The inset shows the maximum frequency.

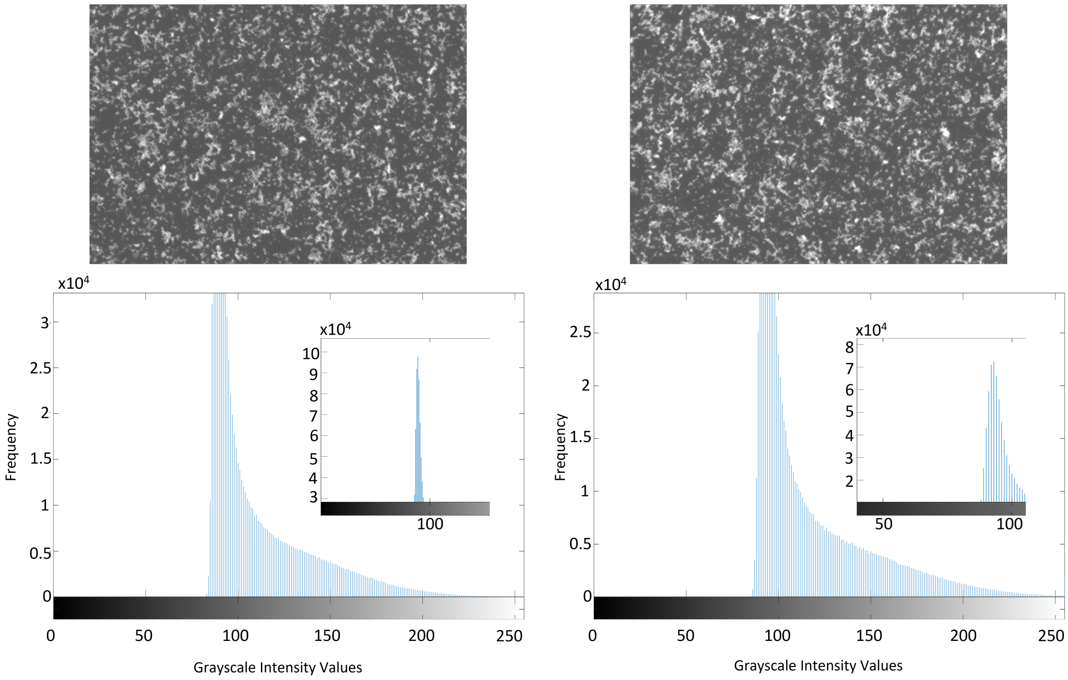

Figure 3.12: Two different images of platinum nanoparticles on silicon and their corresponding pixel histogram. The inset shows the maximum frequency.

3.2.3. Optimization of Nanoparticle Printer Settings

Through the spark ablation method mentioned in section 2.6, nanoparticles can be deposited in a dry process through the VSP-G1 nanoparticle generator connected to the VSP-P0 nanostructured material printer (VS Particle). This equipment offers planar control of the deposition through a moving nozzle. The nozzle is connected to motors that can navigate in the x,y, and z directions, creating a local printing process. The printer settings were optimized to get distinct Pt NPs surface densities according to the printing speeds.

Many settings and parameters can be changed to achieve the desired densities (e.g., gap voltage, spark current, printing speed, carrier gas flow, printing height, etc.). However, this will lead to a large number of permutations. Therefore, it was opted to observe the deposition of varying printing speeds while the other settings and parameters were kept constant. To achieve this, a series of single lines were printed on a die silicon substrate, each with varying speeds. Figure 3.13 shows a sample of the die with single-line depositions. The first top line was printed with the slowest speed of 5 mm/min and then randomized between 25 mm/min to 200 mm/min at 25 mm/min intervals. Moving along the x-direction started approximately 15 seconds after the start command of printing, hence a visible and similar circular deposition shown in Figure 3.13, creating a distinct marker for SEM imaging. Furthermore, the density of the nanoparticles of a defined printer setting was determined by averaging the surface density of three photos taken from the same deposition. Each photo taken for every line was approximately at the center but in different x-locations (see Figure 3.14). The same approach was used for understanding the Pt NPs deposition of two overlapping line passes (2-layers), and three overlapping lines. Presented in Figure 3.15 are the depositions of Pt NPs at different printing speeds.

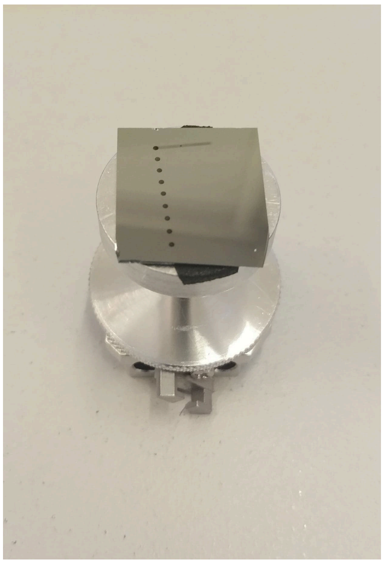

Figure 3.13: Single line deposition of Pt NPs with varying printing speeds placed on top of a die holder used for SEM imaging

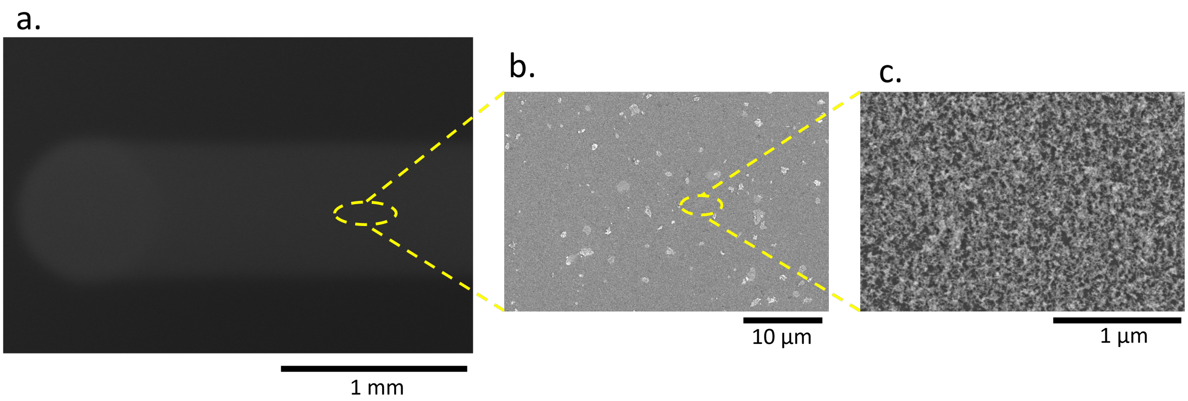

Figure 3.14: SEM image of single line deposition of Pt NPs deposition with increasing magnification. The yellow circle of (a) shows the approximate center of the line

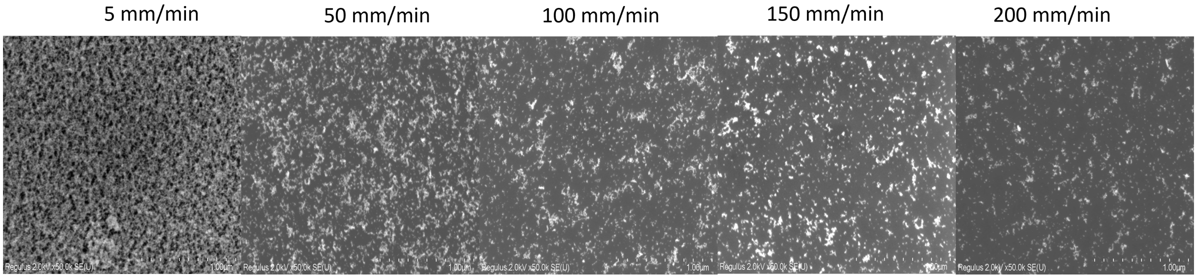

Figure 3.15: Single-layer deposition of Pt NPs at different speeds

3.2.4. Calculation of the Deposition Width

The calculation of deposition width can be achieved through the image processing method similar to subsection 3.2.2, except the SEM images were taken at low magnification (x 50) at a 2 kV accelerating voltage. Shown in Figure 3.16 are two SEM images of the printed line at different speeds. Although there is a visible difference between the widths of the lines, it is difficult to determine these widths through a digital ruler tool, only arbitrarily setting the points of measurements along a blurred outline of nanoparticles. Hence, there is a need to process the images to quantify the widths better.

The images were processed at a data matrix of 411 x 880, removing the circular starting point and the embedded white text. The images were turned binary, creating data matrix columns of 0s and 1s in which 1 represents white. The longest series of 1 s across a column is considered the width. The average length of that data matrix is then used as the width of the printed line. Figure 3.17 shows the image before and after thresholding. The pixel-to-millimeter scale was determined through the image processing program called ImageJ, where the image scale from the original image was used as a reference for the pixel-to-mm conversion, shown in Figure 3.16. **Deposition widths for Pt NPs printed at 137 mm/min, 67 mm/min, 38.3 mm/min, 21.5 mm/min with one layer, and 141 mm/min with 2 layers were calculated to be 0.526 mm, 0.554 mm, 0.637 mm, 0.680 mm, and 0.542 mm, respectively.**

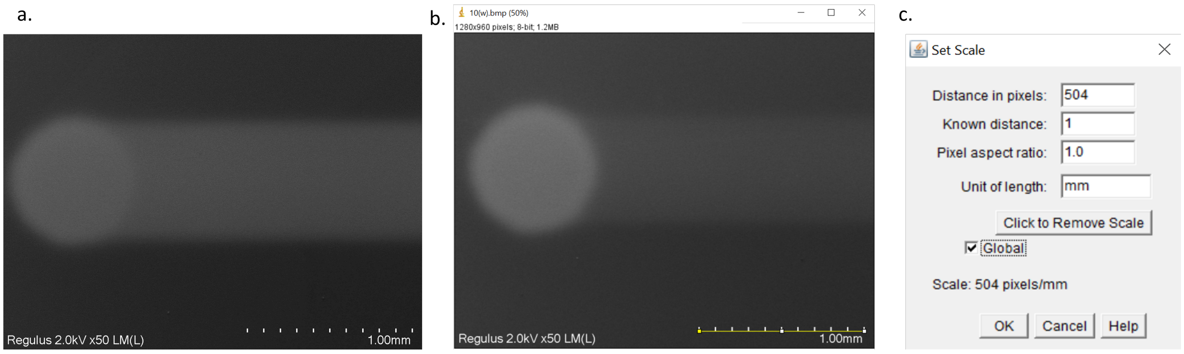

Distance in pixels: 504
Known distance: 1
Pixel aspect ratio: 1.0
Unit of length: mm
☑ Global
Scale: 504 pixels/mm

Figure 3.16: SEM images of a Pt NPs printed line at (a) a slow and (b) fast printing speed and (c) ImageJ window for setting scale according to the yellow line in (b)

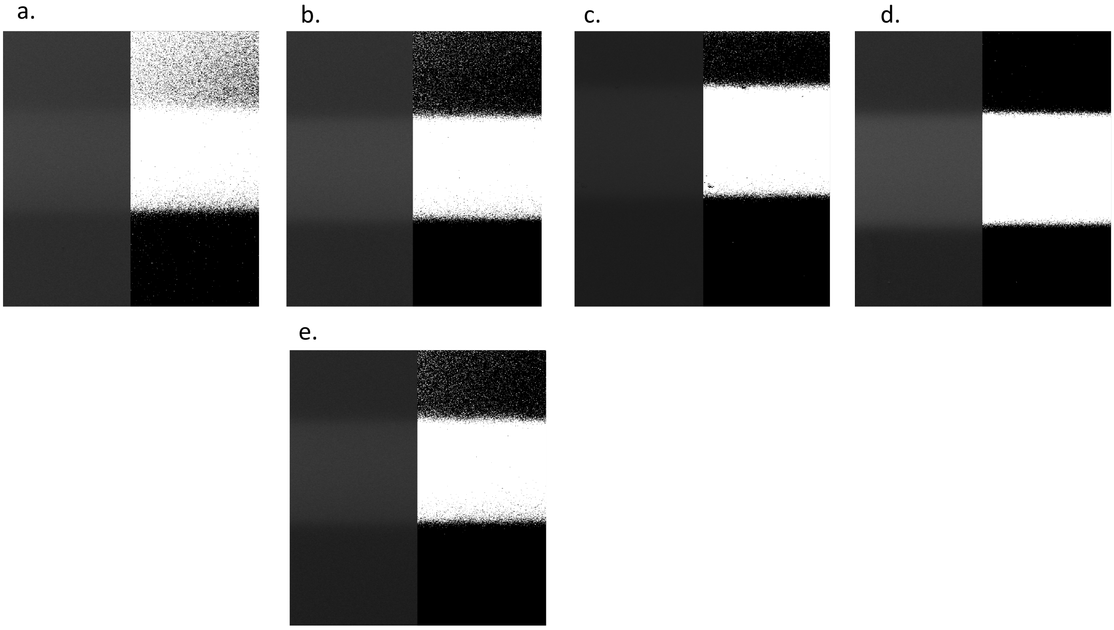

Figure 3.17: 411 x 880 pixel image thresholding of the printed line (left) before (right) after. One-line pass Pt NPs print with printing speed (a) 137.0 mm/min (b) 67.0 mm/min (c) 38.3 mm/min (d) 21.5 mm/min, and (e) Two-line pass of printing Pt NPs at 141.0 mm/min. Deposition width is 265, 279, 321, 343, and 272 pixels, respectively.

3.2.5. Optical Transmittance Test

The samples used for the optical transmittance tests were prepared by depositing nanoparticles on a glass slide. The sample size for the measurement was approximately 2 x 1 cm. To achieve that size, the printer's nozzle followed a laddered path in which a line is printed along the x-direction followed by a step at the y-direction. By determining the width of the line through the method discussed in subsection 3.2.4, there is a logical step height that ideally does not overlap with the previous line. The step height used were 500 μm, 600 μm, 700 μm for the Pt NP printing at 137 mm/min, 67 mm/min, and 21.5 mm/min. The step height of 500 μm was also used for Pt printing at 141 mm/min with two layers.

The optical transmittance of graphene was also tested. The sample was prepared by depositing molybdenum over a silicon wafer and growing graphene after. A die from that wafer of approximately 2 x 1 cm was submerged in H_2O_2 to etch the molybdenum. Eventually, the graphene fully detached from the substrate. The graphene was then transferred carefully onto a glass slide.

The optical transmittance of the nanoparticles and the graphene were evaluated using the PerkinElmer Lambda 1050+ UV/VIS/NIR spectrometer. The measurements were taken from 300 to 900 nm. In addition to the samples with metal nanoparticles and that of graphene, the optical transmittance of a pristine glass slide was measured. This data was then used in post-processing with a custom MATLAB script as a reference to remove its effect on the samples' transmittance.

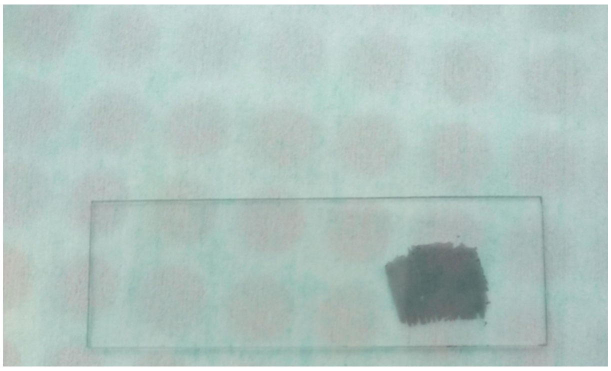

Figure 3.18: Graphene on glass

3.2.6. Atomic Force Microscopy

The surface topography of the Pt NPs was investigated through atomic force microscopy (AFM; Ntegra). Line samples of the Pt NPs were printed on a silicon die. The topography of the Pt NPs printed at 137 mm/min, 67 mm/min, 38.3 mm/min, 21.5 mm/min with one layer, and 141 mm/min with 2 layers were tested at a frequency of 0.50 Hz semi-contact mode and a scan size of 10 μm x 10 μm. Five scans were performed for each line at the lines' approximate center. The AFM data were further processed using Gwyddion.

3.2.7. Platinum Nanoparticle Conductivity Test

Since the Pt NPs were printed as a line that goes from the insulating layer to the exposed electrode, the printed line may create a conducting path. To better understand this behavior, a four-point probe measurement test was performed by passing a current through two outer probes and measuring the voltage between two inner probes. This test was performed using Cascade Microtech's probe station. Line samples were printed over vertical metal tracks (100 nm gold with 10 nm chromium). The test was conducted twice for each printed line at different locations. However, the distance between the inner probes was kept constant at 25 μm. The measurement was conducted from -500 mV to 500 mV with 8 mV steps.

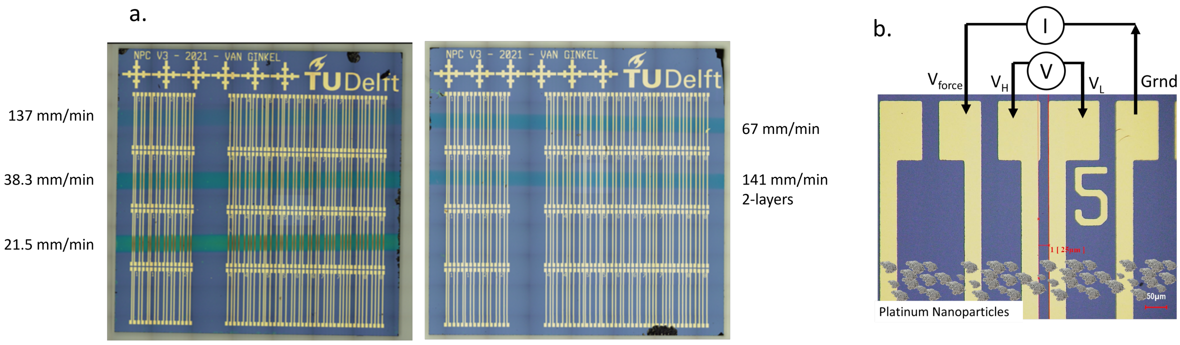

Figure 3.19: (a) Samples for the four-point probe measurement with the corresponding printing speed. (b) A schematic of the four-point probe measurement

3.3. Electrochemical Characterization

This section describes the test setup, settings, and parameters used for the electrochemical measurements (EIS, CV, VT) and the procedures for investigating the stability of the nanoparticles on graphene. Seven graphene electrodes were tested with EIS, CV, and VT. While for each Pt NP surface density, five graphene electrodes with nanoparticles were investigated for the same tests. Three electrodes under each sample category (graphene only, graphene with Pt NPs printed at 137 mm/min, 67 mm/min, 38.3 mm/min, 21.5 mm/min with one layer, and 141 mm/min with 2 layers) were tested for stability through a continuous CV cycle. Lastly, a comparison of graphene and graphene with Pt NPs (38.3 mm/min) was performed with an ultrasonic stability test.

3.3.1. Three-electrode Setup

The three-cell configuration was used for all the electrochemical measurements (EIS, CV, and VT). A 3 mm platinum electrode served as the counter electrode (CE), a silver/silver chloride (Ag/AgCl) electrode was used for the reference (RE), and the graphene electrode (with or without Pt NPs) was the working electrode (WE) (see Figure 3.21). All the electrodes were submerged in phosphate-buffered saline (PBS) during the measurements. In an effort to minimize the variability in the location of the electrodes when performing a test, a holder was designed with SolidWorks and 3D-printed with an Ultimaker2$^+$. There are two slots designed: one is for the counter electrode and the other is for the working electrode, which is made to clip the PCB. The holder did not have a slot for the reference, but this electrode was positioned close to the working electrode. Metal clips were used to secure the PCB in place. The holder for the counter electrode was made tall so it goes into the electrolyte vertically. Figure 3.20 presents the holder design. Moreover, all electrochemical measurements were conducted by a potentiostat (Autolab PG-STAT302N), and the setup was inside a Faraday cage.

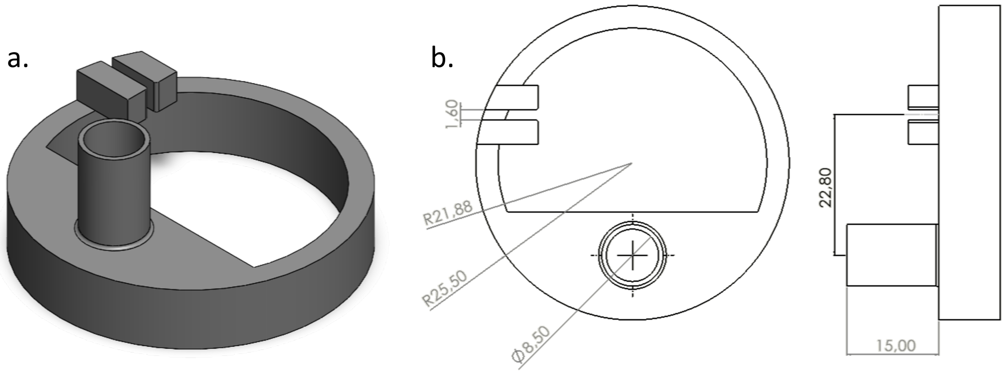

Figure 3.20: (a) Three dimensional model of the holder used for EIS and CV and (b) Top view and side view technical drawing of the model, respectively. The units are in mm, and the image is not scaled

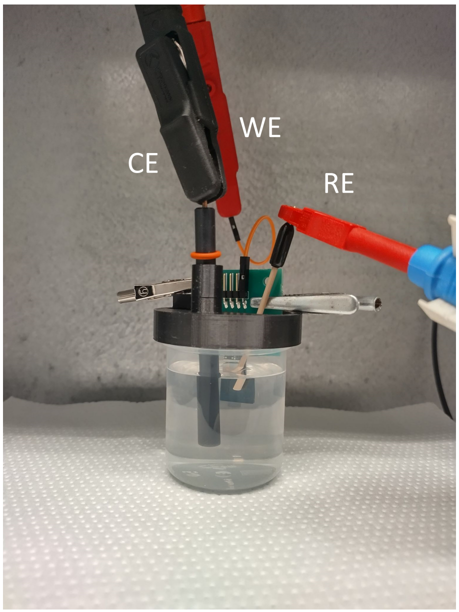

Figure 3.21: Three-electrode setup

3.3.2. Electrochemical impedance spectroscopy

The EIS was performed using the ***Cyto2.0EIS*** program of the potentiostat. The potentiostat applied a 10 mV RMS sinusoidal voltage between the WE and the RE, and the current was measured between the WE and the CE. EIS was conducted throughout a range of frequencies (from 1 Hz to 100 kHz). The impedance values at 1 kHz were used for comparison between the samples.

3.3.3. Cyclic Voltammetry

The CV measurements were performed using the ***Cyclic Voltammetry Linear Scan*** program of the potentiostat. Two potential limits were used, from -0.5 V to 0.5 V and -0.6 V to 0.6 V, at scan rates of 0.1 Vs^{-1}, 0.2 Vs^{-1}, 0.6 Vs^{-1}, and 1 Vs^{-1}, chosen range to compare with the work of Babaroud [15]. At least three scans were performed or until the voltammograms stabilized. Results from the last scan of the CV tests were used to calculate the CSC.

3.3.4. Voltage Transient

The program ***Chronopotentiometry fast*** of the potentiostat was used for the VT measurements. A biphasic current pulse with 1 ms pulse width and 100 μs interphase delay was applied between the WE and the CE. The amplitude of the current pulse is incrementally increased until the negative polarization of the WE reached -0.6 V, also considering that the positive polarization did not exceed 0.6 V. The largest current pulse recorded from the VT tests was used to calculate the CIC.

3.3.5. Stability and Adhesion

It is critical to investigate the stability and integrity of electrodes and their coating, especially for chronic applications. Any material degradation or coating delamination may contribute to the device's failure and, possibly, cause biological harm. The stability of the graphene and the graphene with Pt NPs were investigated in 2 ways: continuous CV tests and ultrasonic stability tests.

A continuous CV test was performed for 500 cycles from -0.6 V to 0.6 V at a scan rate of 1 Vs^{-1}. Confocal optical images with the Keyence VK-X250 and impedance measurements of the electrodes were taken immediately before and after the continuous CV test. For the ultrasonic stability tests, a digital ultrasonic cleaner (HBM Machines) was used on two electrodes with graphene and two with 40% Pt NPs. The electrode end of the devices was submerged in a water bath of $\approx$250 mL at 30 W, 22 kHz, and alternating time intervals of 2 and 3 minutes. Optical images of the electrodes were taken before and after the ultrasonic stability tests. Impedance measurements were performed on the electrode with 40% Pt NPs after every time interval.

4

Results and Discussion: Material Characterization

This section describes the results from the material characterization of the graphene electrodes and the platinum nanoparticles printed in a line on a silicon die. The deposition of the Pt NP was observed at various print speeds, and further characterization methods like roughness, optical transmittance, and conductivity tests were performed for print speeds 137 mm/min, 67 mm/min, 38.3 mm/min, 21.5 mm/min one-layer print and 141 mm/min with two layers.

4.1. Raman Spectroscopy

The Raman spectrum of a graphene electrode is shown in Figure 4.1. The corresponding D, G, and 2D intensity peaks are observed at 1356 cm^{-1}, 1586 cm^{-1}, and 2706 cm^{-1}, respectively. Their corresponding peaks are 780 au, 3068 au, and 1900 au, respectively. The I_D /I_G is 0.25, indicating defects in the graphene. While the I_{2D} /I_G is 0.62, indicating that the graphene sample is multilayered. These characteristic ratios are different compared to previously reported ratios from similar graphene samples made with the same recipe (I_D /I_G = 0.38 and I_{2D} /I_G = 0.74) [15]. The I_D /I_G of the graphene electrodes used in the research have improved from previous attempts to prepare graphene electrodes which were met with some growth issues [55]. The 2D peak measured is also in the same bandwidth as other transfer-free graphene samples [67].

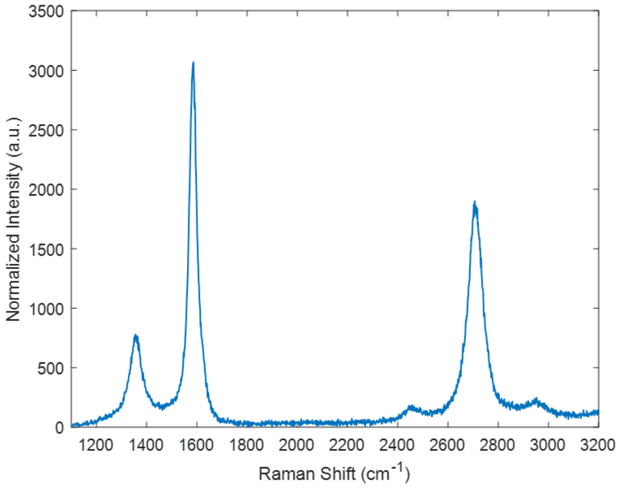

Figure 4.1: Raman spectrum of the graphene electrode

4.2. Platinum Nanoparticle Density Characterization

As mentioned in Section 3.1.2, the Pt NP deposition was optimized to get distinct densities by varying the printing speed over 1- 2 printing layers. Additionally, three overlapping layers were characterized by their surface densities and speed to better understand the Pt NP deposition. Shown in Figure 4.2 (left graph) are the results of the surface density versus the varying speeds of one to three printing layers. Printing at the same speed with increasing layers increases the surface density. Therefore, to achieve the same surface density of overlapping layers compared to a single layer, the printing speed must increase.

The desired surface densities were 10%, 25%, 40%, 50% printed as one layer and 25% printed with 2 layers. This was based on the negative exponential correlation of the surface density and the printing speeds, as achieving these densities would require unique printing speeds and would avoid any confusion and overlap when preparing the samples. The right graph of Figure 4.2 presents a comparison between the desired densities interpolated from the data of the 1-layer curve (in blue) and the actual densities taken from two batch printing sessions (in orange and yellow). There is a large difference between the data from the printer setting optimization and the batch printing due to varying machine states and printer start points.

At the time of printer setting optimization, the spark generator was only partially wiped. While the spark generator was thoroughly cleaned with isopropanol for the batch printing sessions. Since the generator was thoroughly cleaned at the start of the first batch printing session, the printing speeds taken from the interpolated data resulted in higher densities than expected which had been an interesting discovery. The desired surface density of 10% increased to 27%, 25% to 45%, and 50% to 53%. This meant that the speed must significantly increase to achieve the originally desired surface density. To avoid using speeds closer to the maximum capabilities of the motor control unit because its precision in movement might be compromised, the height of the start point was increased for the batch printing sessions. The start point of the printing during the NP printer setting optimization process was set to 0.825 mm above the touch point, while the two batches were performed at a starting point of 0.925 mm above the touch point.

Therefore, results from the optimization of NP printer settings have become unreliable in achieving the desired surface density from the interpolated speeds. Hence, it was eventually opted to use printing speeds that lead to different surface densities regardless of the initially desired surface density values. **Thus, the printing speeds of 137 mm/min, 67 mm/min, 38.3 mm/min, and 21.5 mm/ min were used for the one-layer printing. A speed of 141 mm/min was used for the two-layer printing with comparable surface densities from the printed layer using 67 mm/min.**

There are also differences, although smaller, in surface densities between the two batch printing sessions (Shown in Figure 4.2 and Figure 4.3), despite a thorough spark generator clean at the start of each session. This suggests that electrochemical results from this research may vary between the batches. Thus, a two-sample t-test was performed to compare the means of the impedance (at 1 kHz), total CSC, and CIC between the two batches. Shown in Table 4.1 is the number of sample sizes (n) at each batch of each electrode type which varies minimally (only 2 or 3 sample sizes for some). Hence, a simulated dataset (n=5) was created by getting a randomized number based on the means and the standard deviation of their original dataset. P-values of the EIS and CIC data show no statistically significant difference between batches ($p>0.05$). However, some of the p-values of the CSC (in blue) show otherwise. **Therefore, EIS and CIC data are further analyzed into a combined dataset of the batches, while the batch variation between the CSC data is also considered upon further analysis.**

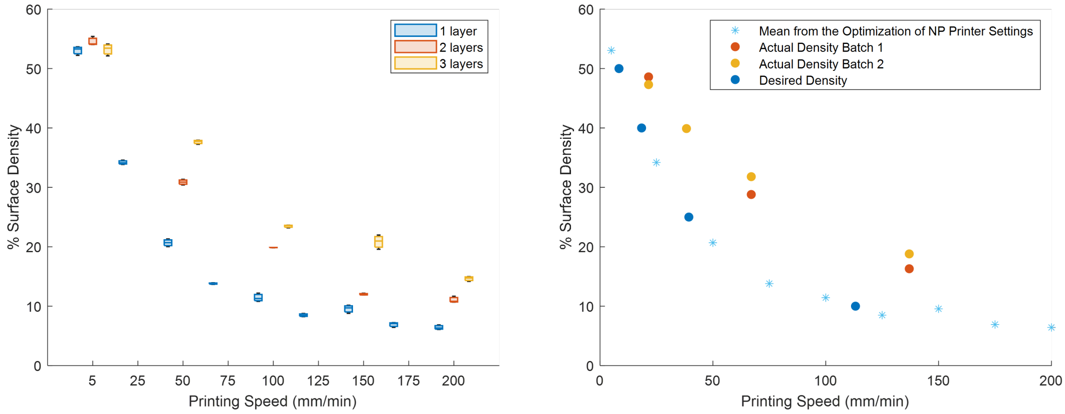

Figure 4.2: (Left) Boxplot data (n=3) of the % surface density versus the printing speed of one printing layer and overlapping layers. (Right) Comparison of % surface densities at different printing sessions

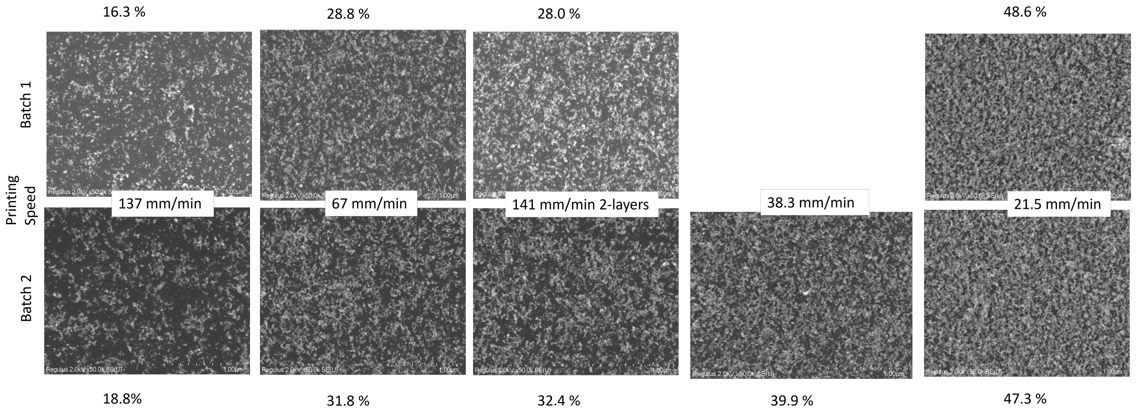

Figure 4.3: SEM images of the printed Pt NP taken from line samples of a silicon die (at 50,000 magnification) before the start of the batch printing session. The percentages shown are the % surface densities

Table 4.1: Two-Sample T-test results between Batch 1 and Batch 2 NP printing

			Sample Size (n)		**P-values**		
Electrode Type		**No of Print Layer**	**Batch 1**	**Batch 2**	**Impedance Magnitude at 1 kHz**	**Total CSC (-0.5 V to 0.5 V; 0.1 V/s)**	**CIC**
Graphene only		1	4	3	0.35	0.04	0.41
Pt NPs on graphene printed at	137 mm/min	1	3	2	0.13	0.06	0.9
	67 mm/min	1	3	2	0.19	0.37	0.29
	141 mm/min	2	2	3	0.43	1	0.06
	38.3 mm/min	1	0	5			
	21.5 mm/min	1	2	3	0.07	0.03	0.06

P-values in blue are < 0.05

4.3. Optical Transmittance

Shown in Figure 4.4 are the optical transmittance measurements of graphene and the printed Pt NPs, but not the combination of both. From a little over 300 nm wavelength, the transmittance of the Pt NPs remains relatively stable until 900 nm. The optical transmittance of the Pt NPs also corresponds to the printing speeds used. Since higher printing speeds result in lower surface density, its optical transmittance is also higher compared to slower print speeds. Moreover, the results of the Pt NPs printed at 67 mm/min over one layer, and 141 mm/min over two layers show comparable results, suggesting minimal optical transmittance differences between 1-layer or 2-layer printing for the same surface densities.

There is also an observable steep rise (> 100%) because the transmittance measurement of glass as it approaches 300 nm wavelength is lower than that of the Pt NPs on glass. In contrast, graphene's optical transmittance at shorter wavelengths is significantly reduced because of its increased ultraviolet (UV) absorption.

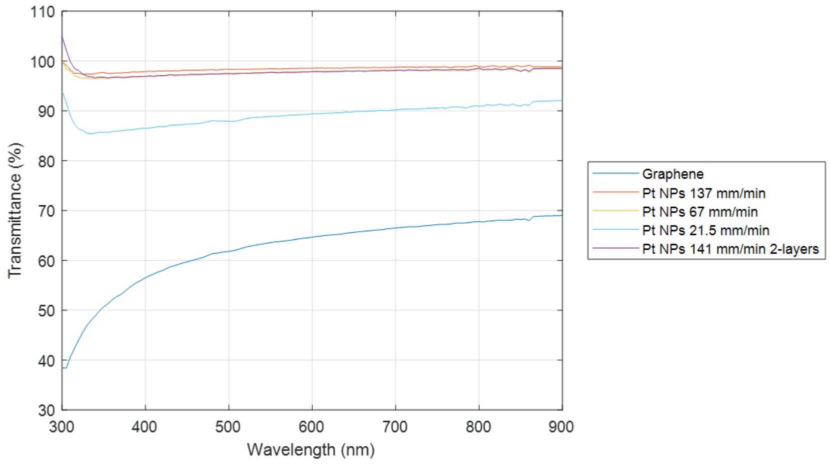

Figure 4.4: Optical transmittance measurements of graphene and Pt NPs printed with different speeds

4.4. Platinum Nanoparticle Roughness

This section presents the mean and RMS roughness measurements of Pt NP line samples printed with different speeds, shown in Figure 4.5. Despite the large spread of the measurements, there is still an observable trend in the print speed. Slower print speeds result in higher roughness values for the one-layer samples. The roughness of the 141 mm/min 2-layer sample is slightly higher than that of the 67 mm/min 1-layer print, despite similar surface density values (See also Figure 4.6). The roughness of each print line was also observed through the SEM at a magnification of 3,000. Slower print speeds result in more Pt NP deposits. Additionally, despite similar surface densities measured at a magnification of 50,000, the 67 mm/min print speed sample had significantly more large metal deposits than the 141 mm/min 2-layer sample at a 3,000 magnified view.

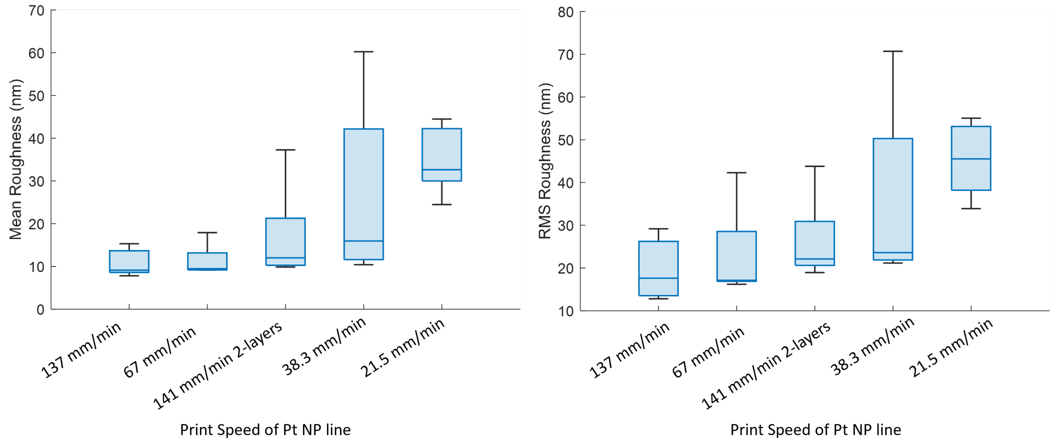

Figure 4.5: Roughness data versus print speeds

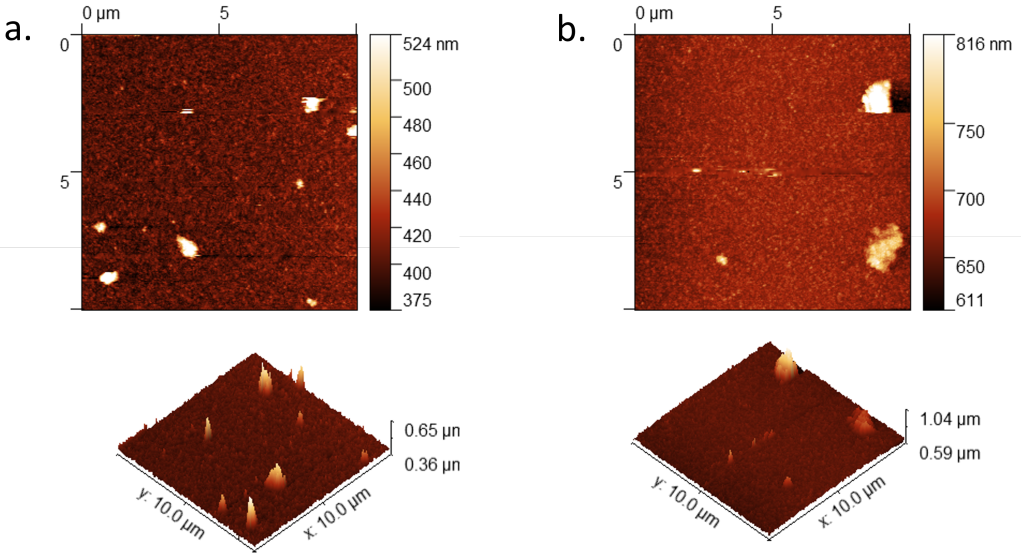

Figure 4.6: AFM plots in 2D (top) and 3D (bottom) of the (a) 67 mm/min printed Pt NPs and (b) 141 mm/min 2-layer printed Pt NPs

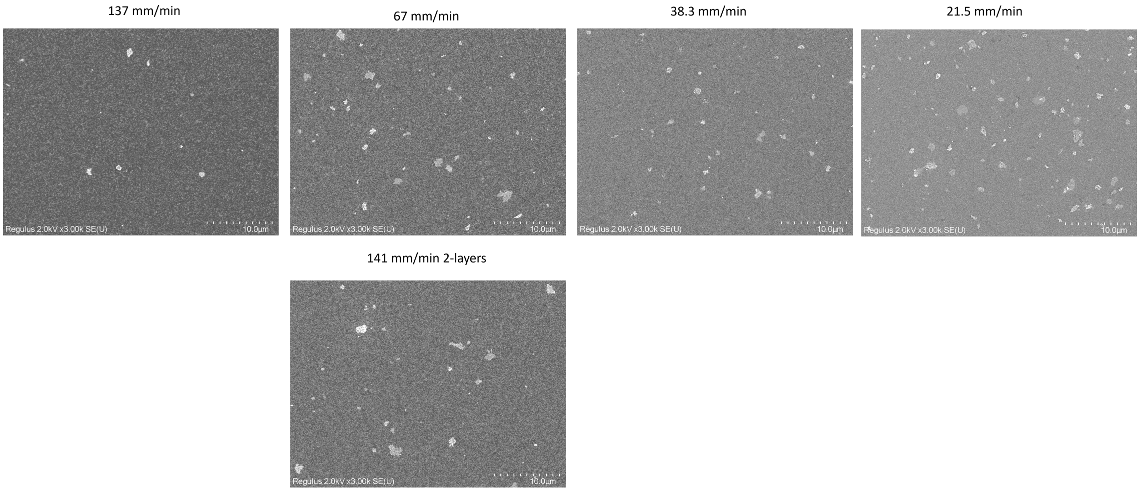

Figure 4.7: SEM images of the printed Pt NPs taken from line samples of a silicon die at 3,000 magnification

4.5. Platinum Nanoparticle Conductivity Test

Using a probe station and semiconductor parameter analyzer, the electrical conductivity of the sparse Pt layers was tested. It is expected that a layer with low density should show no conductance. Of the ten measurement attempts (2 tests for each line sample), only 3 samples showed a current above the noise floor of the instrument. Hence, there is a conducting path along those measured areas. One test for the print sample of 67 mm/min and two for the print sample of 21.5 mm/min show a conductive circuit. Presented in Figure 4.8 are the current-voltage curves measured for these closed circuits. The curve of the 67 mm/min line show noisier data than the 21.5 mm/min line, and it also has significantly higher sheet resistance. Additionally, the 38.3 mm/min line did not have any current flowing on both tests, and the height difference between the exposed graphene electrode and the insulating layer (310 μm) likely severs any connecting path for print speeds of 38.3 mm/min and higher. Although, this is likely not the case for the 21.5 mm/min print line with stable linear current-voltage characteristic curves.

This means that the surface area of the graphene electrodes with Pt NPs produced at this speed has likely expanded from the length of the printed line, possibly invalidating the electrochemical tests and any quantitative comparative analysis with other samples.

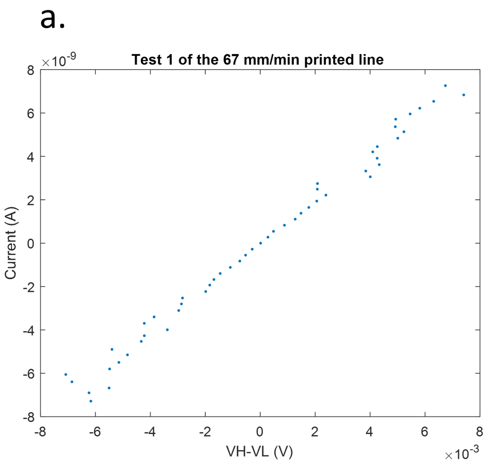

Ave Sheet Resistance = 453 5233 ± 500 949.1 Ω/□

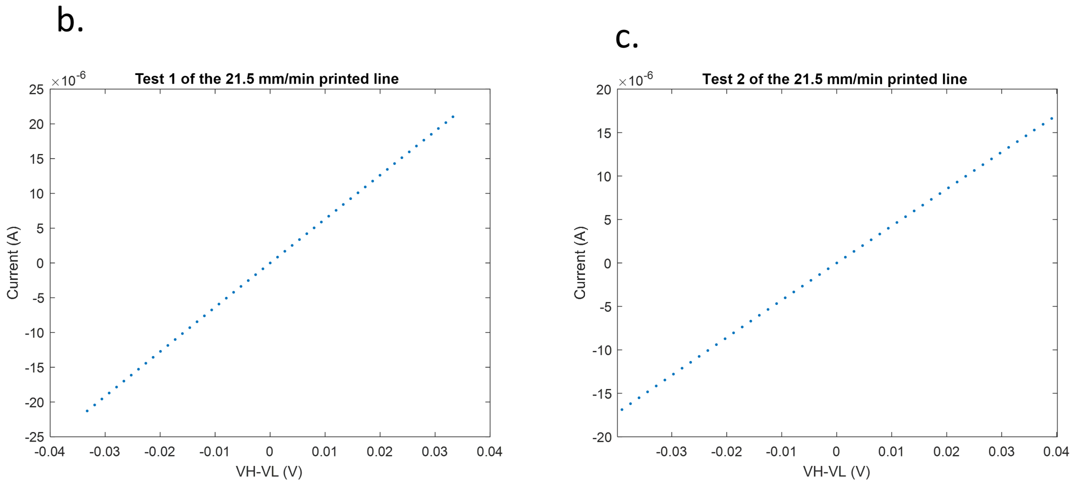

Ave Sheet Resistance = 7 143.97 ± 38.37 Ω/□

Ave Sheet Resistance = 10 608.48 ± 60.21 Ω/□

Figure 4.8: Results of the four-point probe measurements of (a) 67 mm/min and (b-c) 21.5 mm/min Pt NP printed lines

4.6. Summary of the Material Characterization

Understanding the complete calibration process of the nanostructured material printer (VSP-P0) is crucial for improving the precision of the nanoparticle deposition. A consistent print start point and a clean nanoparticle generator reduce the unpredictability of batch printing. For subsequent optimization attempts to achieve the appropriate surface densities, these steps must be taken into consideration.

Moreover, increasing the print speed affects the surface density with a negative exponential correlation. The Pt NP line of one-layer print at 137 mm/min, 67 mm/min, 38.3 mm/min, and 21.5 mm/min show increasing and distinct surface densities. Other characterization methods also correspond to their distinct densities. Roughness increases with higher surface densities. While the opposite is observed for their optical transmittance. It is also observed that there is a batch variation between these densities that may have affected the variance of the electrochemical results within each electrode type, especially for CV measurements.

Additionally, the two-layer print at 141 mm/min showed that its surface density is similar to that of the 67 mm/min printed line when viewed at 50k magnification with the SEM. Characterization results also show comparable optical transmittance, despite more metal deposits (viewed at 3k magnification at the SEM) at the one-layer 67 mm/min line. Therefore, it may be possible to create multilayer Pt NP on graphene neural electrodes that are still suitable for optogenetics and fluorescence imaging; leveraging this added roughness may improve the recording and stimulating capabilities of the one-layer Pt NP on graphene electrodes.

Furthermore, conductivity tests of the Pt NP lines show current flow for the 21.5 mm/min line. This suggests that the surface area of the graphene electrodes printed with this speed has likely increased significantly from the length of the printed line unless severed by the height difference between the graphene and insulation layer.

5

Results and Discussion: Electrochemical Characterization

This section details the results of the electrochemical tests, such as the EIS, CV, and VT tests. It also includes the results from the adhesion and stability tests, which incorporate EIS and CV measurements. EIS, CV, and VT tests were performed on 7 graphene electrodes and 25 electrodes with Pt NPs on graphene (Gr-Pt NPs) (5 samples each for the 137 mm/min, 67 mm/min, 38.3 mm/min, 21.5 mm/min with 1-layer, and 141 mm/min with 2-layers). Three from each electrode category were tested for their electrochemical stability through continuous CV tests. Separate samples of graphene electrodes and graphene electrodes with 38.3 mm/min Pt NP were used for the ultrasonic stability tests.

5.1. Electrochemical Impedance

Figure 5.1 presents the average impedance magnitude and phase angle of the combined dataset of batches 1 and 2, measured from 1 Hz to 100 kHz. Figure 5.2 visualizes the impedance values at 1 kHz, where the median is shown as the line inside the box. The upper and lower quartiles are the top and bottom edges of the box, respectively. The uppermost and lowermost lines of each plot represent the highest and lowest impedance values, respectively. The dataset also shows only one outlier (represented by the circle), found in the plot of the graphene electrode with Pt NPs printed at the speed of 67 mm/min (Gr-Pt NPs 67 mm/min).

EIS analysis shows capacitive behavior for the electrodes in this dataset. Further analysis shows that the graphene electrodes' impedance (at 1 kHz) improved by at least 19 kΩ compared to the impedance of Gr-Pt NPs 137 mm/min—followed by a decreasing trend according to their decreasing print speeds for the one-layer Gr- Pt. This improving impedance trend resulted from the increasing surface density of the Pt NPs. In addition, when comparing the Gr-Pt NPs 67 mm/min one-layer and Gr-Pt NPs 141 mm/min two-layers, there is a slight impedance decrease in favor of the latter. This is likely due to the higher roughness of the two-layer print, although its effect is not significant. Also, the variance of the graphene is significantly reduced when deposited with Pt NPs.

Shown in Table 5.1 is the mean impedance values of each electrode type. The standard deviation of graphene electrodes is at least three times that of Gr-Pt NPs, revealing that Pt NP dominates the electrochemical processes during EIS measurements. The standard deviation of the two-layer print is also higher than the one-layer prints, implying higher uncertainty with increasing print layers. The mean impedance of Gr-Pt NPs 38.3 mm/min is also slightly lower than that of planar platinum electrodes of the same geometric surface area, reported as 8.7 kΩ [15]. The outcome of this test is promising for the use of recording electrodes, as electrodes with impedance values lower than 1.5 MΩ may record neural activity with a good signal-to-noise ratio [28].

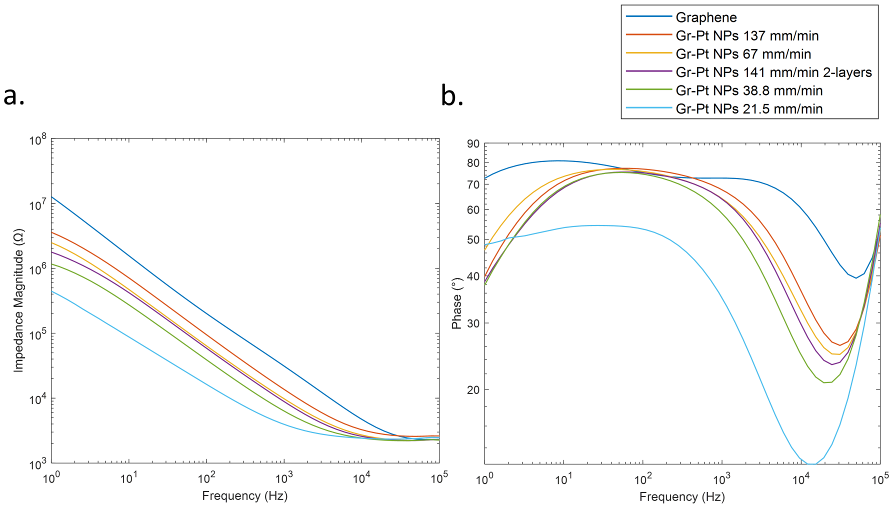

Figure 5.1: Average (a) impedance magnitude and (b) phase angle plots

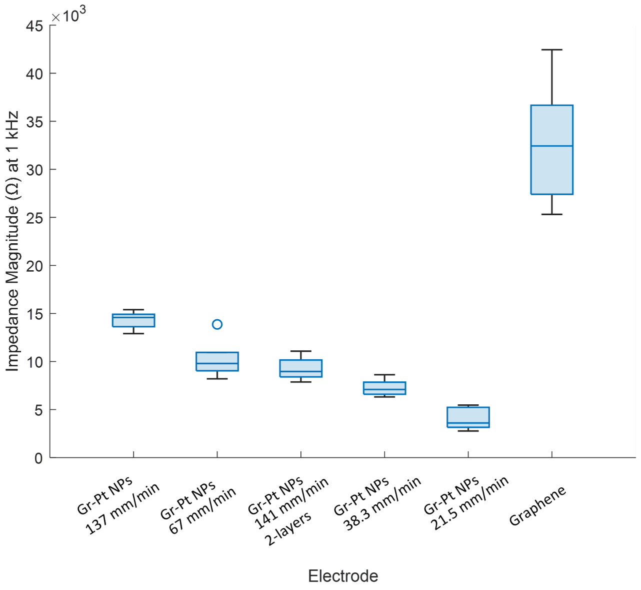

Figure 5.2: Impedance magnitude at 1 kHz of each electrode type

Table 5.1: Mean Impedance at 1 kHz (n=5)

Electrode Type	Impedance (Ω)	Electrode Surface Area (μm^2)	Area-normalized impedance (Ωcm^2)
Graphene*	34078 ± 3394	68320	23.3 ± 2.3
Gr-Pt NPs 137mm/min	14294 ± 951	68320	9.8 ± 0.6
Gr-Pt NPs 67 mm/min **	9318 ± 799	68320	6.4 ± 0.5
Gr-Pt NPs 141 mm/min 2-layers	9263 ± 1239	68320	6.3 ± 0.8
Gr-Pt NPs 38.3 mm/min	7258 ± 897	68320	5.0 ± 0.6
Gr-Pt NPs 21.5 mm/min	4051 ± 1188	68320	2.8 ± 0.8 height

* Extreme upper and lower values removed. ** Outlier removed (n=4). All else are n=5

5.2. Charge Storage Capacity

Figure 5.3 plots the cyclic voltammograms of the electrode types. The data taken are from the median values of the combined dataset of the batches. While Figure 5.4 compares the cyclic voltammograms of two graphene electrodes printed with the slowest speeds (38.3 mm/min and 21.5 mm/min), with the latter having the densest Pt NP coating. There is a significant difference between the CV measurements of graphene and graphene with Pt NPs, with the latter's plots also increasing in size according to the speed of the one-layer print. However, the plots of the 141 mm/min 2-layers are more closely similar to that of Gr-Pt 38.3 mm/min rather than Gr-Pt NPs 67 mm/min. Thus, the CSC of the 2-layer print is higher than the equivalent one-layer print. Additionally, there is a huge difference between the cyclic voltammograms of Gr-Pt NPs 38.3 mm/min and Gr-Pt NPs 21.5 mm/min, despite having only $\approx$ 8% difference between their surface densities. This sudden increase is likely due to the increased surface area of the Gr-Pt NPs 21.5 mm/min, not only from its higher surface density on the graphene electrode but also because the 3 mm print line likely expands the surface area (also proven by the conductivity test at Section 4.5). Therefore, its CSC is not relevant for comparison.

Table 5.2 compares the CSC per electrode type per batch. As per the t-test performed (see Section 4.2), the data between the batches of the graphene electrodes and the Gr-Pt NPs 21.5 mm/min are statistically significant. For the graphene electrodes, this means that the randomly chosen electrodes for each batch cannot be immediately comparable. However, looking into graphene's dataset for batch 1, the sample with the largest CSC (1914 μC/cm^2) has likely affected the results of the t-test. Discarding that data point as an outlier, the mean and standard deviation of batch 1 of the graphene electrodes is 377$\pm$163 μC/cm^2. The p-value from the t-test results to 0.2, thus showing that the CSC of the graphene electrodes is not statistically different between the batches. The same applies to all graphene electrodes with Pt NPs apart from Gr-Pt NPs 21.5 mm/min. Samples of batch 2 of Gr-Pt NPs 21.5 mm/min have high variation between values. Despite removing the highest value (43955 μC/cm^2), the results of the t-test still concluded a large difference between batch average values (p=0.04). This is more evidence that the computed CSC of Gr-Pt NPs 21.5 mm/min should be disregarded since the data cannot be compared between samples.

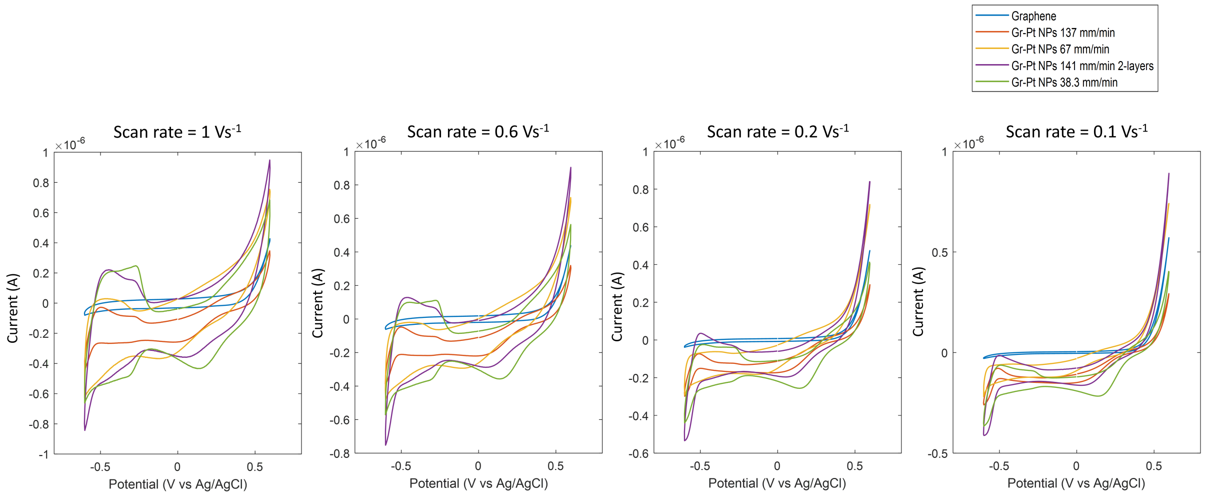

Figure 5.3: Cyclic voltammograms of the electrode types per scan rate

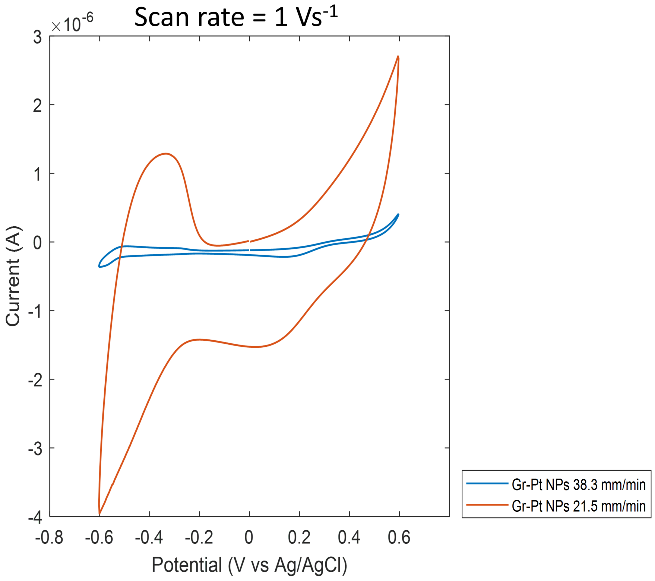

Figure 5.4: A comparison of the cyclic voltammograms of Gr-Pt 38.3 mm/min and Gr-Pt 21.5 mm/min

Table 5.2: Total CSC (μC/cm^2) of each sample per batch

			Gr- Pt NPs									
	Graphene		**137 mm/min**		**67 mm/min**		**141 mm/min 2-layers**		**38.3 mm/min**		**21.5 mm/min**	
	Batch 1	Batch 2	Batch 1	Batch 2	Batch 1	Batch 2	Batch 1	Batch 2	Batch 1	Batch 2	Batch 1	Batch 2
	1914	393	1417	2267	2170	2836	2002	2650		3998	29940	17104
	307	665	1679	2356	2235	2148	1389	3815		2164	29520	43955
	260	803	1117		1056			3850		3068		3598
	563									5320		
										4068		
Mean	761	620	1404	2311	1820	2492	1695	3438		3724	29730	21552
Std	780	208	281	63	663	486	434	683		1184	297	20542

Measured from -0.5 V to 0.5 V 0.1 V/s

Table 5.3 and Table 5.4 shows the average total and cathodic CSC of the electrodes with the combined dataset from batch 1 and 2. As reflected by the cyclic voltammograms, there is an increasing CSC trend with increasing Pt NP surface density. Additionally, at slower scan rates, the Gr-Pt NPs 141 mm/min 2-layers show a comparable CSC with Gr-Pt 38.3 mm/min. While at a scan rate of 1 V/s, CSC of Gr-Pt NPs 141 mm/min 2-layers is more similar to Gr-Pt NPs 67 mm/min. This is reasonable given that their surface densities, when seen one-dimensionally, are comparable (the top view in SEM is used to compute surface density). This means that the information from a scan rate of 1 V/s is solely provided by the exposed nanoparticles. The contribution of the added depth or dimensionality of the 2-layer print increases with decreasing scan rates. However, similar to EIS, the standard deviation of the two-layer print is also higher than the one-layer prints, implying higher uncertainty with increasing print layers.

When the findings of this study are compared to the most recent developments in graphene and platinum electrodes, the CSC of Gr-Pt NPs 137 mm/min and Gr-Pt NPs 67 mm/min is still inferior to the CSC of graphene (with a growth period of 20 minutes) and platinum. However, the CSC of Gr-Pt NPs 38.3 mm/min and Gr-Pt NPs 141 mm/min 2-layers shows comparable data with the state-of-the-art electrodes at faster scan rates, but the impact from the increased surface area provided by the Pt NPs also dominates at slower scan rates.

Table 5.3: Average Total CSC and a comparison with the state-of-the-art graphene and platinum electrodes

	Total CSC (μC/cm^2)					
Electrodes	**1 V/s**	**0.6 V/s**	**0.2 V/s**	**0.1 V/s**	**Water Window (V)**	**Reference**
Graphene	248±185	349±272	817±666	1566±1277	-0.6 to 0.6	This work
Gr-Pt NPs 137mm/min	551±73	778±109	1887±268	3497±495	-0.6 to 0.6	
Gr-Pt NPs 67 mm/min	745±91	959±159	1960±504	3399±1062	-0.6 to 0.6	
Gr-Pt NPs 141 mm/min 2-layers	765±175	1038±258	2382±764	4397±1671	-0.6 to 0.6	
Gr-Pt NPs 38.3 mm/min	954±103	1199±99	2444±368	4365±821	-0.6 to 0.6	
Graphene (20 min growth time)	972	1298	2425	3549	-0.8 to 0.6	Babaroud[15]
Platinum	940	1131	1611	2012	-0.6 to 0.6	

Table 5.4: Average Cathodic CSC and a comparison with the state-of-the-art graphene and platinum electrodes

	Cathodic CSC (μC/cm^2)					
Electrodes	**1 V/s**	**0.6 V/s**	**0.2 V/s**	**0.1 V/s**	**Water Window (V)**	**Reference**
Graphene	78±52	95±63	159±102	233±146	-0.6 to 0.6	This work
Gr-Pt NPs 137mm/min	345±84	496±146	1211±439	2197±849	-0.6 to 0.6	
Gr-Pt NPs 67 mm/min	469±73	625±118	1327±367	2207±746	-0.6 to 0.6	
Gr-Pt NPs 141 mm/min 2-layers	525±124	735±202	1741±620	3145±1248	-0.6 to 0.6	
Gr-Pt NPs 38.3 mm/min	651±45	878±88	1993±429	3614±892	-0.6 to 0.6	
Graphene (20 min growth time)	631	812	1453	2151	-0.8 to 0.6	Babaroud [15]
Platinum	726	919	1396	1765	-0.6 to 0.6	

5.3. Charge Injection Capacity

Figure 5.5 plots the biphasic pulse with the maximum current amplitude that could be applied to the electrodes before exceeding the safe potential window and the voltage transient measurements. The data taken are from the median values of the combined dataset of the batches. While Figure 5.6 compares the voltage transient measurements of Gr-Pt NPs 38.3 mm/min and Gr-Pt NPs 21.5 mm/min. As previously discussed, the results of the Gr-Pt NPs 21.5 mm/min have high variance within its dataset and have an incomparable surface area. Hence, the data of Gr-Pt NPs 21.5 mm/min shall not be used to compute the CIC. However, presenting Figure 5.6 was meant to show the magnitude of the difference between the two Pt NP coatings.

Moreover, similarly to the EIS and CV results, an increasing trend in the maximum current amplitude and CIC exists with increasing surface densities, shown in Table 5.5. Similar CIC values between Gr-Pt NPs 67 mm/min and Gr-Pt NPs 141 mm/min 2-layers are also observed, implying that information on the voltage transient measurements is provided by the top or exposed Pt NPs. However, the CIC values of the graphene electrodes with Pt NPs pale compared to the CIC of the state-of-the-art electrodes.

Additional VT tests were performed on one of the graphene electrodes at an interface polarization of -0.8 V, for better comparison with the state-of-the-art graphene electrode. The maximum current amplitude applied to reach that interface potential was 11.4 μA, only $\approx$ 38% of the maximum current of the state-of-the-art. Consequently, its CIC is 16.6 μC/cm^2. The difference in their CIC may be caused by a difference in the graphene layers, experimental setup, or other factors. The combination of these factors may have also caused it. Regardless, a Pt NP coating still improves the CIC of graphene compared with similar graphene electrodes as a reference, performed under similar experimental conditions.

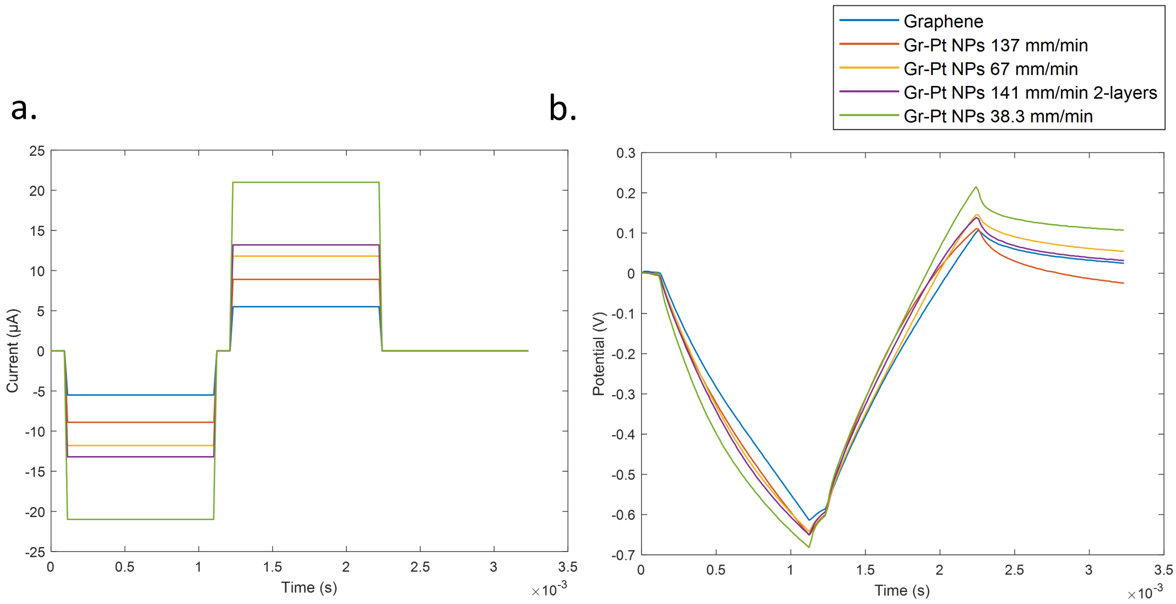

Figure 5.5: (a) Biphasic current pulse and (b) voltage transient measurements per electrode type

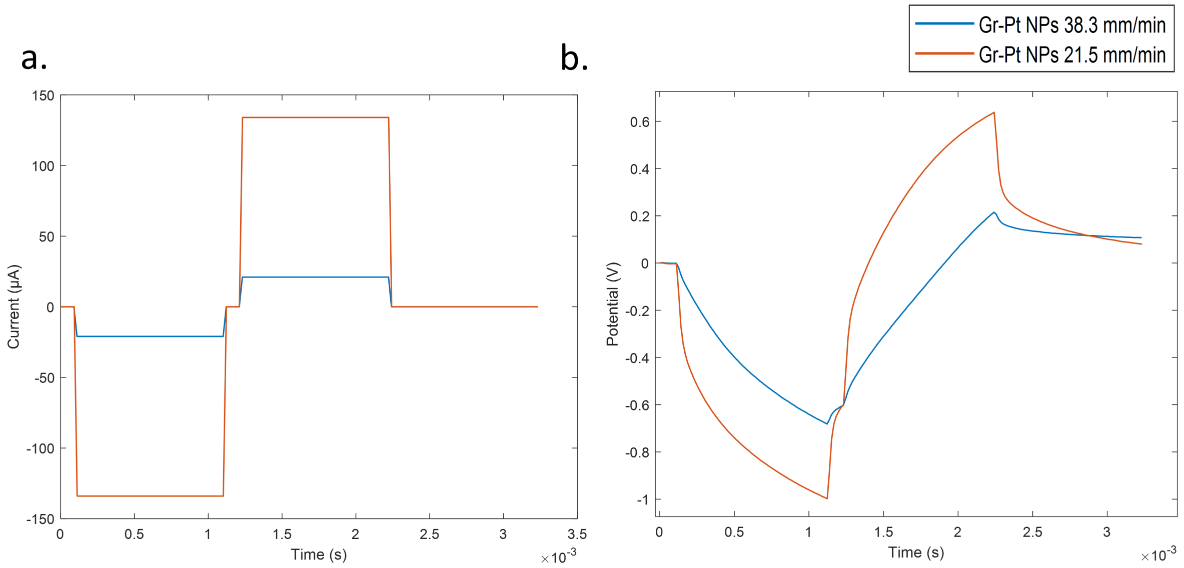

Figure 5.6: A comparison between Gr-Pt NPs 38.3 mm/min and Gr-Pt NPs 21.5 mm/min. (a) Biphasic current pulse and (b) voltage transient measurements

Table 5.5: CIC and a comparison with the state-of-the-art graphene and platinum electrodes

Electrodes	Max Current (μA)	CIC (μC/cm^2)	Interface Polarization (V)	Reference
Graphene	5.7±1.5	8.4±2.1	-0.6	This work
Gr-Pt NPs 137mm/min	8.6±1.3	12.6±1.9	-0.6	
Gr-Pt NPs 67 mm/min	12.5±1.5	18.3±2.2	-0.6	
Gr-Pt NPs 141 mm/min 2-layers	13.6±1.0	19.8±1.5	-0.6	
Gr-Pt NPs 38.3 mm/min	20.9±1.2	30.6±1.8	-0.6	
Graphene (20 min growth time)	30	44	-0.8	[15]
Platinum	46	67.33	-0.6	

5.4. Stability and Adhesion

5.4.1. Continuous Cyclic Voltammetry

This test was performed to investigate the electrochemical stability of the graphene and Pt NP coating through 500 charging and discharging cycles. Three samples were tested for each electrode type. After the tests, six of the electrodes have improved impedance (at 1 kHz): three of which are graphene electrodes and the other three are the Gr-Pt NPs 67 mm/min, Gr-Pt NPs 38.3 mm/min, and Gr-Pt NPs 21.5 mm/min. All six of these electrodes correspondingly had increased CSC. However, this was not the case for the other electrodes tested. Five Gr-Pt NPs electrodes had increased impedance. Hence its CSC decreased. However, seven Gr-Pt NPs electrodes had increased impedance, but their CSC also increased, suggesting some instability in the Pt NP coating. It is likely that some Pt NPs have partially detached and had varying effects on the impedance and CSC.

Figure 5.7 and Figure 5.8 visualize the overall impedance changes and CSC, respectively. Figure 5.7 still presents a trend with increasing surface densities, despite the considerable differences within the samples of the electrode types. One sample of the Gr-Pt NPs 141 mm/min 2-layers shows a similar impedance change with one sample of Gr-Pt NPs 67 mm/min, and two similar changes with Gr-Pt NPs 38.3 mm/min. This indicates that the stability of Gr-Pt NPs 141 mm/min is higher than its one-layer surface density counterpart (Gr-Pt NPs 67 mm/min).

The results of the continuous CV tests are also found in Figure 5.9. The cyclic voltammograms of the 3rd, 250th, and 500th scan cycles of each electrode type are shown in that figure. In all instances with Pt NPs, peaks eventually formed in both the forward and backward scans. These peaks can be attributed to hydrogen and oxygen adsorption when the molecules attach to the electrode surface or desportion when they are removed from it [68], [69]. These peaks contributed to the change in CSC to varying degrees. Some of the peaks were observed above 0 A, causing the cathodic CSC for some electrodes to increase more than others. Gr-Pt NPs 67 mm/min had the smallest increase change in total CSC. Gr-Pt NPs 141 mm/min 2-layers had a much larger cathodic and total CSC increase than the Gr-Pt 67 mm/min, attributed to the larger surface area reflected by the higher mean roughness. Hence, a larger surface area provides more hydrogen and oxygen adsorption and desportion sites. The presence of sodium and chlorine was also observed on the electrode surface, formed in a dendritic pattern (see Figure 5.10). This may provide insights into the electroactive area of the electrode. This was verified through energy-dispersive X-ray spectroscopy (EDX).

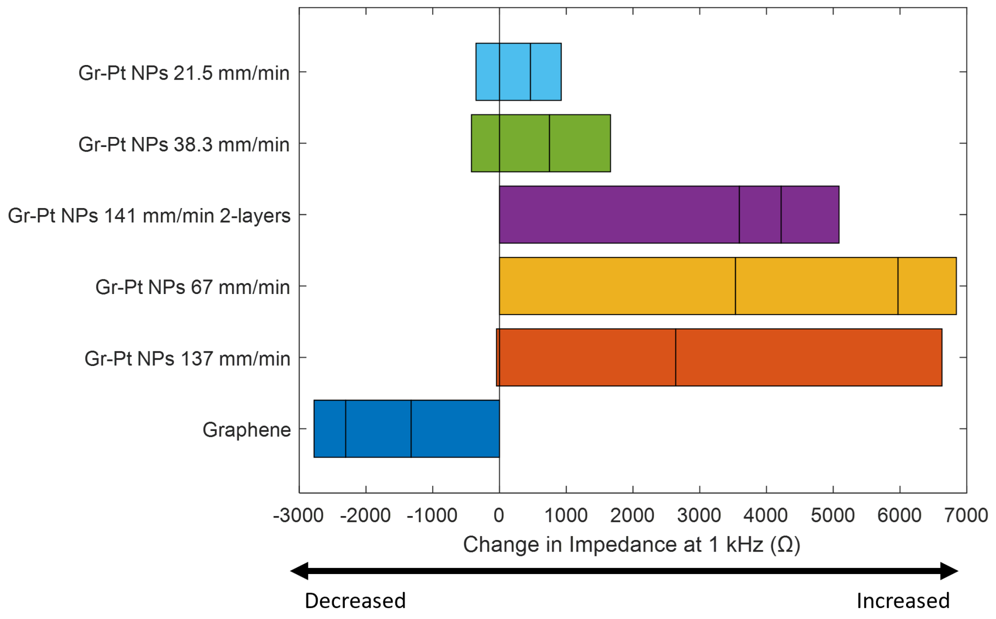

Figure 5.7: Sum of impedance change after 500 CV cycles of three samples (three blocks) per electrode type.

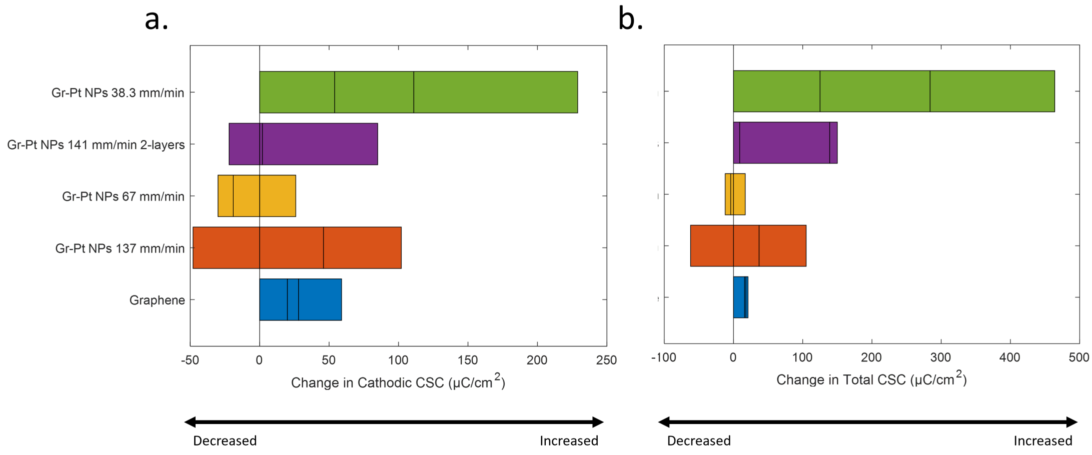

Figure 5.8: Sum of change in (a) cathodic and (b) total CSC of three samples (three blocks) per electrode type.

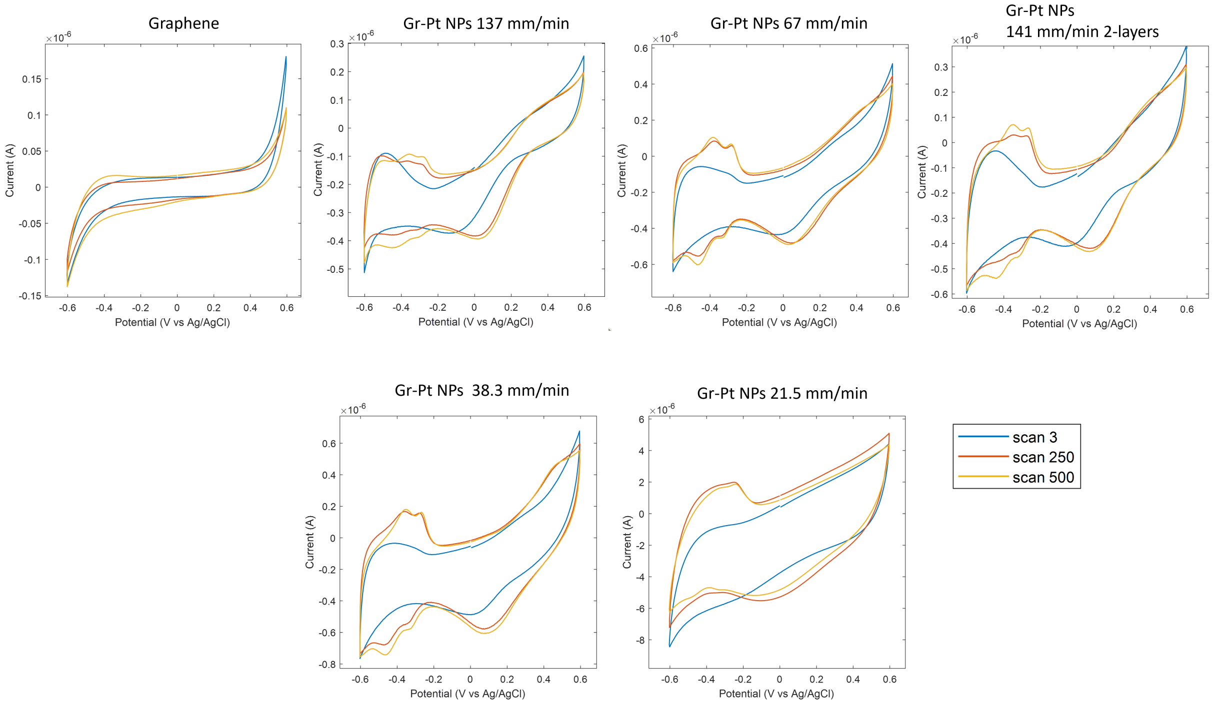

Figure 5.9: Cyclic voltammograms of continuous CV

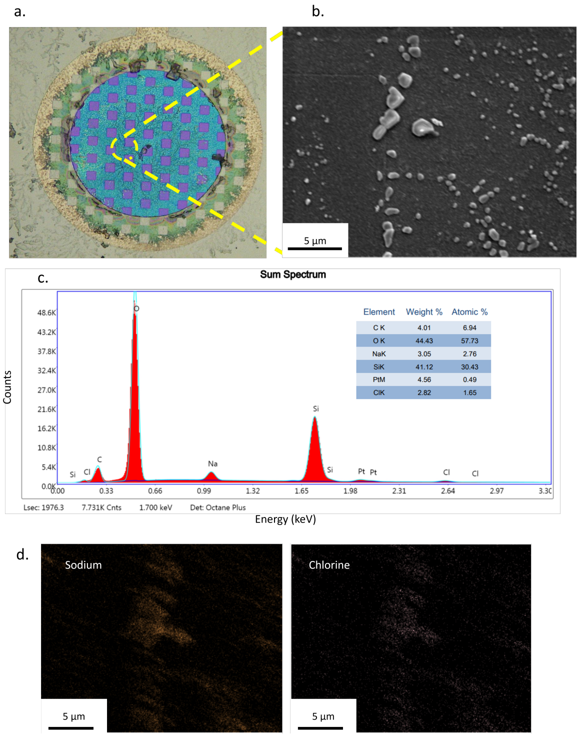

Element	Weight %	Atomic %
C K	4.01	6.94
O K	44.43	57.73
NaK	3.05	2.76
SiK	41.12	30.43
PtM	4.56	0.49
ClK	2.82	1.65

Figure 5.10: (a) Microscopy image of the electrode after the continuous CV, (b) SEM image of the observed deposits. (c) EDX map spectrum and (d) elemental mapping of sodium and chlorine

In addition, out of 15 Gr-Pt NP electrodes tested with the continuous CV scans, only one sample (Gr-Pt NPs 38.3 mm/min) showed unstable charging and discharging behavior. The cause was not further investigated since it was not observed in other tested samples. Its behavior stabilized before the last scan cycle. A comparison between a stable continuous cyclic voltammogram and an unstable one is presented in Figure 5.11.

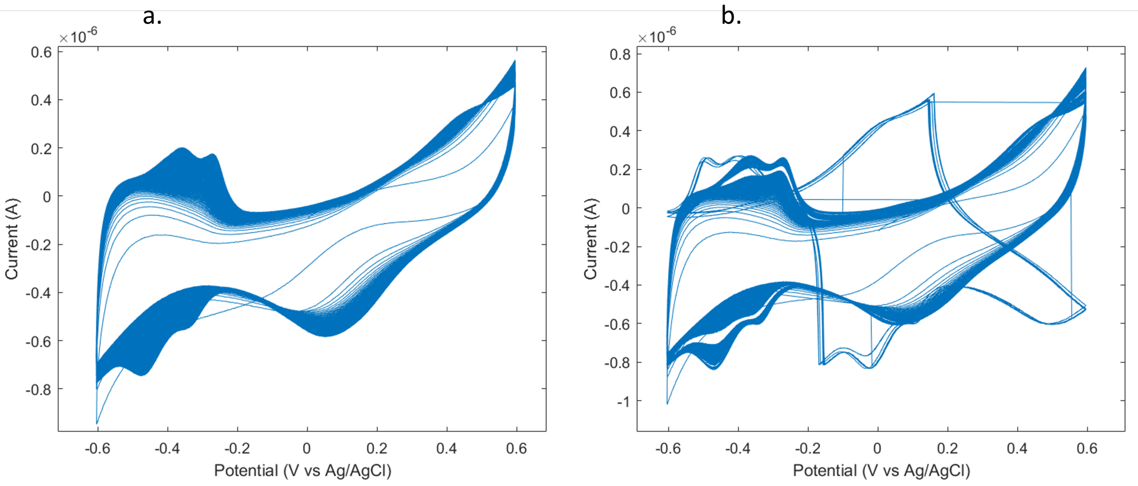

Figure 5.11: A comparison between a (a) stable and (b) unstable continuous cyclic voltammogram. Samples are both Gr-Pt NPs 38.3 mm/min

5.4.2. Ultrasonic Stability Tests

Figure 5.12 presents the results of Sample 1 of the electrodes (Gr-Pt NPs 38.3 mm/min) tested with ultrasound to investigate the mechanical stability of the Pt NPs. After 5 minutes, there was visible delamination of the graphene layer. However, the impedance (at 1 kHz) is 13199 Ω which is still much lower than the average impedance of the graphene (34078 Ω), thus implying that there are still Pt NPs on the test sample. This is the same after 7 minutes at 26247 Ω. However, the Pt NP surface density after this duration is unknown. Attempts to investigate this with the SEM have been unsuccessful due to the inability to focus on the area of interest. After 10 minutes, the sample's impedance increased to 38722 Ω. Despite the substantial delamination of the graphene layer, the impedance only increased by ≈ 4000 Ω. This suggests that there may still be some Pt NPs on what is left of the graphene layer. There was also a color change on the graphene after 12 minutes, possibly caused by substantial delamination of the Pt NPs. Table 5.6 also presents the impedance changes of another sample, of which complete delamination from the bulk was observed after only 7 minutes. In both instances, the graphene layer on the SiO_2 fails first during the ultrasonic tests. Investigating the stability of the Pt NPs on graphene is ineffective if the graphene layer itself easily delaminates from the substrate. Hence, graphene on polymeric substrates like parylene C may be a more appropriate sample for ultrasonic testing as its porous structure may provide a better mechanical anchor for the graphene [70].

Furthermore, additional observations were made during this test. The graphene electrodes showed partial to complete delamination of the layer after only 2 minutes of ultrasonic tests, while the sample with Pt NPs (38.3 mm/min) barely had any visible changes on the layer. This comparison is shown in Figure 5.13. This demonstrates that the Pt NP coating, which extends over the exposed electrode, provides some mechanical protection to the graphene layer beneath.

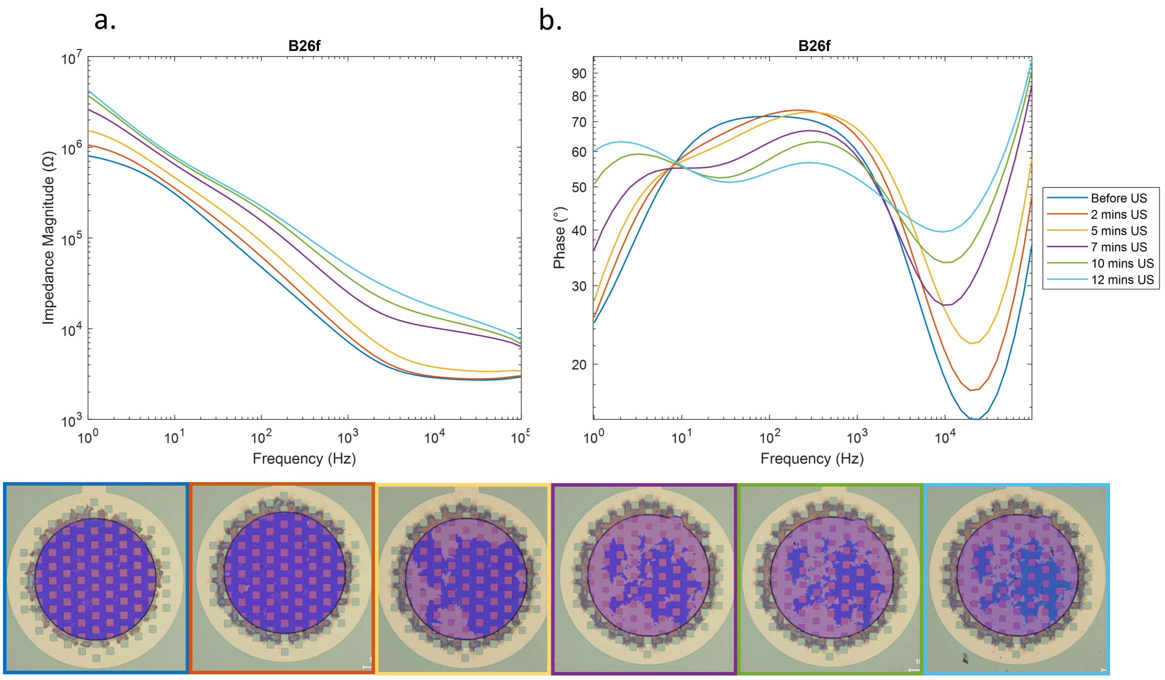

Figure 5.12: (a) Impedance magnitude and (b) phase angle plots between ultrasonic stability tests

Table 5.6: Impedance Magnitude at 1 kHz after Ultrasonic Stability Test

		Ultrasonic Test Duration				
Gr-Pt 38.3 mm/min	**Before US**	**2 mins**	**5 mins**	**7 mins**	**10 mins**	**12 mins**
Sample 1	7 528	8 859	13 199	26 247	38 722	51 825
Sample 2	8 966	10 937	23 533	96 033		

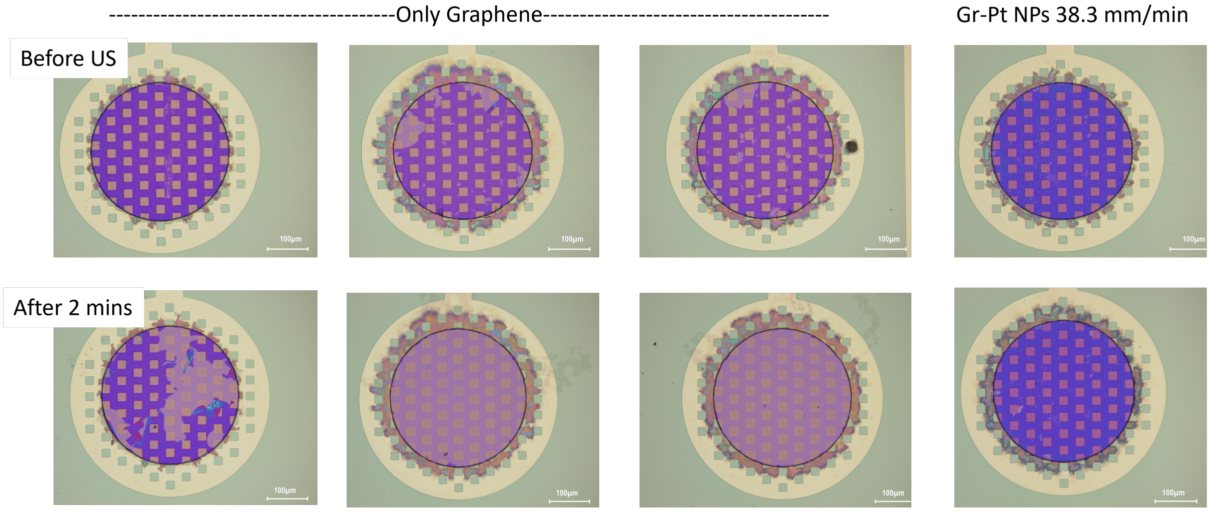

Figure 5.13: A comparison of four electrodes after 2-minute ultrasonic stability tests

5.5. Summary of the Electrochemical Characterization

Interfacing platinum nanoparticles with graphene improved its electrochemical properties such as its impedance, CSC and CIC. The graphene electrodes' impedance (at 1 kHz) improved by at least 19 kΩ compared to the impedance of Gr-Pt NPs 137 mm/min—followed by a decreasing trend according to their decreasing print speeds for the one-layer Gr- Pt NPs. The standard deviation of the two-layer print is also higher than the one-layer prints, implying higher uncertainty with increasing print layers, which was also observed in the CV tests. The CSC of the 141 mm/min 2-layer print provided a broader range of charge-storing capacities compared to its one-layer surface density equivalent (Gr-Pt NPs 67 mm/min). Also, the CSC of Gr-Pt NPs 38.3 mm/min and Gr-Pt 141 mm/min 2-layers shows comparable data with the state-of-the-art electrodes at faster scan rates, but the impact from the increased surface area provided by the Pt NPs also dominates at slower scan rates. Moreover, similarly to the EIS and CV results, an increasing trend in the maximum current amplitude and CIC exists with increasing surface densities. Similar CIC values between Gr-Pt NPs 67 mm/min and Gr-Pt NPs 141 mm/min 2-layers are also observed, implying that information on the voltage transient measurements is provided by the top or exposed P t NPs. However, the CIC values of the graphene electrodes with Pt NPs pale compared to the CIC of the state-of-the-art electrodes. In addition, cyclic voltammograms and VT plots of Gr- Pt NPs 21.5 mm/min had a significant difference from Gr-Pt NPs, suggesting that the Pt NP print line at 21.5 mm/min had been so dense that it is conducting, effectively expanding the electrode area over the insulation layer. Therefore, quantitative analysis of its CSC and CIC were omitted.

Furthermore, a continuous CV test showed an overall impedance increase with Gr-Pt NPs, while the bare graphene electrodes improved their impedance. It also showed an overall increase in both cathodic and total CSC. This indicates stable electrochemical performance during charging and discharging cycles. Lastly, a layer of Pt NPs has some effect on protecting graphene from delamination. Pt NPs have also been shown to be still attached to the graphene layer after 10 minutes of US, but the extent of any NP detachment from the US is unknown due to the faster failure rate of graphene.

6

Conclusion and Recommendations

Graphene electrodes can achieve simultaneous electrophysiological recording, optical imaging, and optogenetic stimulation. However, its impedance is higher, and its CIC is much lower than platinum, a metal used for conventional electrophysiological recording and stimulation. Interfacing graphene electrodes with platinum improved their electrochemical performance compared to the bare graphene counterpart when characterized for neural recording, and stimulation applications [26], although these samples were made into fibers and did not leverage graphene's transparency. Another study has also shown improved impedance of planar graphene electrodes when coated with electrodeposited Pt NPs. However, its CIC and coating stability have not been investigated [28]. Therefore, this research has shown a dry and local Pt NP coating method for transfer-free graphene electrodes, and Gr-Pt NP electrodes were tested for their recording and stimulating capabilities as well as their coating stability.

The material and electrochemical characteristics of Pt NPs can be optimized by the print speed of the NP deposition, achieving different surface densities. By comparing only the one-layer prints, there are significant differences in roughness, optical transmittance, and conductivity. Adding another Pt NP layer still has high optical transmittance and increases its roughness without creating a conducting path beyond the area of interest. When interfaced with graphene, the electrochemical characteristics of the Pt NPs correlate to their distinct densities. The impedance, charge carrying, and charge storing capabilities are unique and improved with slower printing speeds. The impedance of graphene decreased by 58.05% (Gr-Pt NPs 137 mm/min) to 78.70% (Gr-Pt NPs 38.3 mm/min), indicating an improvement for neural recording. Correspondingly, it is a 2.38 to 4.69 times improvement. The cathodic CSC increased from 4.42 (Gr-Pt NPs 137 mm/min) to 8.35 (Gr-Pt NPs 38.3 mm/min) times that of graphene's cathodic CSC at 1 V/s. At a slower scan rate of 0.1 V/s, the cathodic CSC of Gr-Pt NPs is 9.43 to 15.51 times that of graphene's, indicating that the effect of the Pt NP coating on graphene is more prominent at slower scan rates. Lastly, the CIC improved by 1.5 to 3.64 times more than graphene's CIC. These values are significantly better than graphene's, proving that Pt NPs can improve recording and stimulating capabilities.

Additionally, impedance measurement showed no significant difference between one-layer (Gr-Pt NPs 67 mm/min) and two-layer (Gr-Pt NPs 141 mm/min 2-layers) surface density equivalents, having a 55 Ω mean difference between the two. This is also the case for CIC with 1.5 μC/cm^2 mean difference. The effect of the two-layer print is more dominant with CV tests at slower scan rates (0.1 V/s). Their CSC difference is 938 μC/cm^2 in favor of the 2-layer print, as opposed to a 56 μC/cm^2 difference at 1 V/s. Therefore, there is interest in investigating how print layers can maximally increase these electrochemical properties due to their added dimensionality without compromising their optical transmittance and increasing the risks of conductive paths beyond the electrode.

Stability tests from continuous CV have also shown promising results of stable electrochemical performance of the Pt NPs. However, it is recommended to perform long-term testing of the device to understand any coating failure better when it occurs. Soaking tests for simulating stability over chronic implantation and continuous VT tests to simulate chronic stimulation can be performed. It is also necessary to improve the sample preparation for these tests as the graphene layer must stably adhere to its substrate, so the focus of the US tests is only on the stability of the Pt NPs. Implementing these electrochemical and stability tests with the full realization of this device (with parylene-C for polymeric encapsulation) is recommended for future studies. Still, the pitch of the extended bond pads must be checked for compatibility with existing flexible flat cable connectors since wire bonding may not be suitable anymore.

For future studies, it is also essential to perform NP optimization tests to determine the correct settings for the intended surface densities. This is advised immediately before printing over the test samples. It is unlikely that the same print speeds will result in the same surface density because of varying machine states and calibration procedures between each user. These steps are critical to implement for minimizing batch and sample variation.

A

Flowchart

NANOPARTICLES ON GRAPHENE ELECTRODES

FLOWCHART

Version: 1
Valid from: February 2022
Made by: Samantha Rice

Run number: EWI7
Process engineer: Samantha Rice
Mentor: Sten Vollebregt

Start date processing: 10 February 2022
Estimated end date: 30 September 2022
Approved by: Paolo Sberna

Contamination: Yes
Labs: CR100, CR10000

EKL(Else Kooi Laboratory)
DELFT UNIVERSITY OF TECHNOLOGY
Address : Feldmannweg 17, 2628 CT Delft, The Netherlands
P.O. Box : 5053, 2600 GB Delft, The Netherlands
Phone : +31 - (0)15 - 2783868
Fax : +31 - (0)15 - 2622163
Website : http://ekl.tudelft.nl/EKL/Home.php

NANOPARTICLES ON GRAPHENE ELECTRODES

Detailed information about possible contamination:

Place/Clean Rooms used in the process:
- Write the sequence of used labs from start to finish.
- Which (Non-standard) materials or process steps
- Process step number
- What kind of process or machine was used?
- The other materials or wafers that contain non-green metals that are also processed in this machine

Lab/ Clean Room	Non-standard materials	Process step	Machine-process	Other materials used in machine
CR100	none	none	none	none
CR10000	Yes, graphene	20	BlackMagic	Cu, Pt, Ni

If there are custom steps in a standard process or possible cross contamination materials are used: Write down the
- Step number
- Material
- Machine/tool where the process is done
- Pre and past process step numbers that are used to prevent cross contamination.

Step number	Material	Machine/Tool/lab	Process steps to prevent cross contamination
21	Cu	Trikon Sigma	Use the cassette for contaminated wafers. Use transport wafers for red metals for each of the test wafers. Use non-contaminated tweezers for the transport wafers and contaminated tweezers for the test wafers.

GENERAL RULES

CLEANROOM BEHAVIOUR

❶ Always follow the **"Security and Behavior"** rules when working in the EKL laboratories.

❷ Always handle wafers with care during processing. Use cleanroom gloves and work as clean as possible!

❸ Use cleanroom gloves when working with vacuum equipment. Do not touch the inside or carriers with bare hands.

❹ Always check equipment and process conditions before starting a process. Do **NOT** make unauthorized changes!

❺ Always follow the operating instructions from the system manuals when using machines.

❻ Directly notify the responsible staff member(s) when there are problems with the equipment (like malfunction or contamination). Flip the status card on the machine over to **DOWN** to warn other users. Also change the status of the system to **DOWN** in the "Phoenix Living Database" system.

❼ **DO NOT TRY TO REPAIR OR CLEAN EQUIPMENT YOURSELF**, and **NEVER** try to refresh a contaminated etch or cleaning bath! Only authorized staff members are allowed to do this.

WORKING WITH CMOS INCOMPATIBLE MATERIALS

❶ Substrates, layers and chemicals which are not CMOS compatible may cause contamination of bathes, equipment, wafer boxes, etc.. Using these materials in the class 100 and SAL cleanroom without permission is **FORBIDDEN.**

❷ The use of CMOS incompatible materials for processing in the class100 and SAL cleanroom must **ALWAYS BE EVALUATED** and **APPROVED** by your mentor and the EKL contamination officer.

❸ Wafers that are contaminated may **NEVER** be processed in any of the bathes or equipment without permission. Special precautions may be required, like the use of a separate container, a special substrate holder or a wafer carrier.

❹ You **MUST** work according to the rules described in the **Preventive Cross Contamination** (PCC) document, available on the "EKL Sharepoint webpage", and the **Materials** database from the "Phoenix Living Database" system.

CLEANING OF WAFERS

Wafers must always be cleaned before performing a **COATING, FURNACE, EPITAXY** or **DEPOSITION** step if they were stored for 4 hours or more.

Use the correct cleaning bathes:

• Acetone	⇨ To remove photoresist that is not used as a mask for ion implantation or plasma etching.
• Tepla stripper	⇨ To remove ion bombarded photoresist after implantion or plasma etching.
• HNO_3 99% (Si)$^+$	⇨ For importing wafers that were processed outside the class100 or SAL cleanroom, and that were **not** in contact with metal layers. **APPROVAL** for importing is needed.
• HNO_3 99% (Si)	⇨ To remove organic material from wafers which were not in contact with metal layers.
• HNO3 69.5% (Si)	⇨ To remove (possible) metal particles caused by wafer handling. It is **NEVER** allowed to use this bath for wet etching or stripping of metal layers!
• HNO_3 99% (green metals)$^+$	⇨ For importing wafers that were processed outside the class100 or SAL cleanroom, and that were in contact with "green" metals. **APPROVAL** for importing is needed.
• HNO_3 99% (green metals)	⇨ To remove organic material on wafers which are or have been in contact with "green" metals (e.g.: Al, Al(1%Si), Ti, Mo, Zr, …).

Note:
- The above described cleaning procedures are only valid for CMOS compatible wafers with CMOS compatible materials on them. **For all other wafers follow the PCC rules and check the Phoenix Materials database.**
- Wafers do **NOT** have to be cleaned **after** a furnace, epitaxy or deposition step if the next process step will be performed immediately, unless the wafers are covered with particles.

FURNACE RESTRICTIONS

Wafers that are covered with photoresist or a metal layer may **NEVER** be processed in any of the furnaces. This also applies for wafers from which a metal layer has been removed by etching. Only alloying in tube C4 is allowed for wafers with an aluminium layer.

MEASUREMENTS

Always perform all the measurement and inspection steps, and **write down the results in your journal and in the logbooks that can be found at some of the equipment**. The results are used to monitor the processes and/or equipment.

It is possible to measure directly on your (CMOS compatible) process wafers with the following Class 100 equipment:

- The Leitz MPV-SP, the WOOLLAM and the KEYENCE microscope. The first 2 systems are used for thickness measurements of transparent layers, and the third system is used for 3D surface metrology. The measurements are non-destructive and without contact to the wafer surface.
- The Dektak 8 surface profilometer. This system is used for step height measurements. In this case a needle will physically scan over the wafer surface, which can be destructive for structures. It is a contact measurement.
- The XL50 or Hitachi SEM. They can be used for inspection of your wafers and for width, depth or thickness measurements.

Note:
- After certain measurements **cleaning of your wafers** may be required for further processing.
- An extra wafer must be processed when other measurements are required (like sheet resistance and junction depth measurements). These wafers can not be used for further processing.

NANOPARTICLES ON GRAPHENE ELECTRODES

STARTING MATERIAL

Use **SINGLE SIDE** polished **LOW RESISTIVITY (LRES)** wafers,
with the following specifications:

Type:	p-type, boron
Orientation:	<100>
Resistivity:	2-5 Ωcm
Thickness:	500 ± 5 µm
Diameter:	100 mm

PROCESS DESCRIPTION

The aim of the current process is to develop functionalized graphene structures for electrical characterization. Graphene is grown on a Mo layer. After graphene growth, gold nanoparticle or platinum nanoparticle deposition will follow. After graphene growth, post-processing is required to achieve the final structure. Therefore, cross-contamination might occur. The required process steps to prevent cross-contamination are mentioned at the beginning of the document.

The process consists of 8 parts:

Part 1: Cleaning step
Part 2: Creation of zero layer
Part 3: Oxide deposition
Part 4: Molybdenum deposition, patterning, and graphene growth
Part 5: Metal deposition, and patterning
Part 6: Photoresist deposition and patterning
Part 7: Molybdenum removal
Part 8: Nanoparticle Printing

NANOPARTICLES ON GRAPHENE ELECTRODES

PART 1: CLEANING STEP

Perform this step ONLY when wafers are taken out of an already opened box!

1. CLEANING: HNO_3 99% and 69.5% • Front side

Clean	10 minutes in fuming nitric acid (Merck: HNO_3 99%) at ambient temperature. This will dissolve organic materials. Use wet bench "HNO_3 99% (Si)" and the carrier with the white dot.
Rinse	Rinse in the Quick Dump Rinser with the standard program until the resistivity is 5 MΩ.
Clean	10 minutes in concentrated nitric acid (Merck: HNO_3 69.5%) at 110 °C. This will dissolve metal particles. Use wet bench "HNO_3 69,5% 110C (Si)" and the carrier with the white dot.
Rinse	Rinse in the Quick Dump Rinser with the standard program until the resistivity is 5 MΩ.
Dry	Use the Semitool rinser/dryer with the standard program, and the white carrier with a red dot.

PART 2: CREATION OF ZERO LAYER

2. COATING AND BAKING • Front side

Use the coater station of the EVG120 system to coat the wafers with photoresist. The process consists of:
- a treatment with HMDS (hexamethyldisilazane) vapor, with nitrogen as a carrier gas
- spin coating of Shipley SPR3012 positive resist, dispensed by a pump
- a soft bake at 95 °C for 90 seconds

Always check the relative humidity (48 ± 2 %) in the room before coating, and follow the instructions for this equipment.

Keep the main flat side of the wafers up
Use program **Co – 3012 – 1,4um – no EBR** (resist thickness: 1.400 μm)

3. ALIGNMENT AND EXPOSURE • Front side

Processing will be performed on the ASML PAS5500/80 automatic wafer stepper. Follow the operating instructions from the manual when using this machine.

Expose **mask COMURK,** die-size 10x10 mm, with job **litho/Zefwam**. Exposure energy: **120 mJ/cm^2**

4. DEVELOPMENT • Front side

Use the developer station of the EVG120 system to develop the wafers. Always check the temperature of the hotplates first. The process consists of:
- a post-exposure bake at 115 °C for 90 seconds
- developing with Shipley MF322 with a single puddle process
- a hard bake at 100 °C for 90 seconds

Keep the main flat side of the wafers up
Use program "**1-Dev-SP**".

5. INSPECTION • Front side

Visually inspect the wafers through a microscope:
- No resist residues are allowed.
- Check the linewidth of the structures.
- Check the overlay of the exposed pattern if the mask was aligned to a previous pattern on the wafer.

6. WAFER NUMBERING • Front side

Use the glass pen in the lithography room to mark the wafers with the **BATCH** and **WAFER** numbers.
Write the numbers in the photoresist, just above the wafer flat. Always do this after exposure and development!
It is **NOT** allowed to use a metal pen or a scriber (pen with a diamond tip) for this purpose.

NANOPARTICLES ON GRAPHENE ELECTRODES

7. PLASMA ETCHING: Alignment markers (URK's) into Silicon • Front side

Use the Trikon Ωmega 201 plasma etcher, and follow the operating instructions from the manual when using this machine
It is **not** allowed to change the process conditions and times from the etch recipe!

Use sequence **URK_NPD** (with a platen temperature of **20 °C**) to etch 120 nm (1200 Å) deep ASM URK's into the Si.

8. LAYER STRIPPING: Photoresist • Front side

Strip resist Use the Tepla Plasma 300 system to remove the photoresist in an oxygen plasma.
Follow the instructions specified for the Tepla stripper, and use the quartz carrier.

Use **program 1**

NANOPARTICLES ON GRAPHENE ELECTRODES

9. CLEANING: HNO_3 99% and 69.5% • Front side

Before starting, check if the HNO_3 69.5% bath is at 110 deg. C and if all the baths are at a sufficient level.

Clean	10 minutes in fuming nitric acid at ambient temperature. This will dissolve organic materials. Use wet bench "HNO_3 99% (Si)" and the carrier with the white dot.
Rinse	Rinse in the Quick Dump Rinser with the standard program until the resistivity is 5 MΩ.
Clean	10 minutes in concentrated nitric acid (Merck: HNO_3 69.5%) at 110 °C. This will dissolve metal particles. Use wet bench "HNO_3 69,5% 110C (Si)" and the carrier with the white dot.
Rinse	Rinse in the Quick Dump Rinser with the standard program until the resistivity is 5 MΩ.
Dry	Use the Semitool rinser/dryer with the standard program, and the white carrier with a red dot.

PART 3: OXIDE DEPOSITION

10. WET OXIDATION: 300 nm thermal SiO_2 • Front side

Use the C1 furnace tube to deposit 300 nm of wet thermal oxide on the wafer.
Use program **wet1000**.

Use an online oxide growth calculator to calculate the time needed to reach the desired thickness.
Check out cleanroom.byu.edu/OxideTimeCalc, then input the calculated time at the variable command line of the recipe

11. MEASUREMENT: Oxide thickness • Front side

Use the Woollam measurement system for layer thickness measurements.

Use project **DIMES General** and recipe '**SiO2 on Si (Th.ox, LPCVD-TEOS)**'
Edit recipe to expected layer thickness: 300 nm but change it back to the previous number
Use data acquisition parameters '**dimes 70'**
Use data analysis strategy '**DIMES oxide (0-1um)**'

NANOPARTICLES ON GRAPHENE ELECTRODES

12. CLEANING • Front side

Before starting, check if the HNO_3 69.5% bath is at 110 deg. C and if all the baths are at a sufficient level.

Clean	10 minutes in fuming nitric acid at ambient temperature. This will dissolve organic materials. Use wet bench "HNO_3 99% (Si)" and the carrier with the white dot.
Rinse	Rinse in the Quick Dump Rinser with the standard program until the resistivity is 5 MΩ.
Clean	10 minutes in concentrated nitric acid (Merck: HNO_3 69.5%) at 110 °C. This will dissolve metal particles. Use wet bench "HNO_3 69,5% 110C (Si)" and the carrier with the white dot.
Rinse	Rinse in the Quick Dump Rinser with the standard program until the resistivity is 5 MΩ.

PART 4: MOLYBDENUM DEPOSITION, PATTERNING, AND GRAPHENE GROWTH

13. Mo DEPOSITION: 50nm • Front side

Use the TRIKON SIGMA sputter coater for the deposition of the catalyst metal Mo layer on the process and test wafers. Follow the operating instructions from the manual when using this machine.

If necessary perform a target clean with recipe **'_Trgt_Cln_Mo_50C'**.
Use recipe **'Mo_50nm_50C'**.

Visual inspection: the metal layer must look shiny.

14. COATING AND BAKING • Front side

Use the coater station of the EVG120 system to coat the wafers with photoresist. The process consists of:
- a treatment with HMDS (hexamethyldisilazane) vapor, with nitrogen as a carrier gas
- spin coating of AZ ECI 3027 positive photoresist, dispensed by a pump
- a soft bake at 95 °C for 90 seconds

Always check the relative humidity (48 ± 2 %) in the room before coating, and follow the instructions for this equipment.

Keep the main flat side of the wafers up
Use coating **'Co –3012 – 2.1um'** (resist thickness: 2.100 μm).

15. ALIGNMENT AND EXPOSURE • Front side

Use the SUSS MicroTec MA/BA8 mask aligner to expose the photoresist.
Use **mask** for device BE2325, layer **GRAPHENE**

Use recipe '**1_FSA_Soft_Contact**'
Calculate the exposure time by consulting the contact aligner exposure energy data log.

16. DEVELOPMENT • Front side

Use the developer station of the EVG120 system to develop the wafers. Always check the temperature of the hotplates first. The process consists of:
- a post-exposure bake at 115 °C for 90 seconds
- developing with Shipley MF322 with a single puddle process
- a hard bake at 100 °C for 90 seconds

Keep the main flat side of the wafers up
Use development program **'1 – Dev – SP'**.

Inspection Visually inspect the wafers through a microscope, and check openings.

17. INSPECTION • Front side

Visually inspect the wafers through a microscope:
- No resist residues are allowed.
- Check the linewidth of the structures.
- Check the overlay of the exposed pattern if the mask was aligned to a previous pattern on the wafer.

NANOPARTICLES ON GRAPHENE ELECTRODES

18. PLASMA ETCHING OF Mo

• Front side

Use the Trikon Ωmega 201 plasma etcher.
Follow the operating instructions from the manual when using this machine.
Check the etching time!

Use sequence **'MoTEST2'** and set the etching time to **t=30s**.

19. LAYER STRIPPING: Photoresist

• Front side

Strip resist	Use the Tepla Plasma 300 system to remove the photoresist in an oxygen plasma. Follow the instructions specified for the Tepla stripper, and use the quartz carrier. Use **program 1**

Visual inspection: the metal layer (protected by the photoresist) must look shiny.

20. GRAPHENE GROWTH

• Front side

Use the AIXTRON BlackMagic Pro to grow graphene using LPCVD at 1050°C.

Use recipe '**Mo_NEW_935C_toph1050C_20min_CH4_preanneal20min**'.

The process wafers are now considered Cu contaminated. Put the wafers in a red process box and use tweezers dedicated to Cu-contaminated processes when handling the wafers.

PART 5: METAL DEPOSITION AND PATTERNING

21. METAL DEPOSITION (Ti/Al)

• Front side

Use the cassette for contaminated wafers. Use transport wafers for red metals for each of the test wafers. Use non-contaminated tweezers for the transport wafers and contaminated tweezers for the test wafers.

Use the TRIKON SIGMA Sputter coater for the deposition of metal interface Ti+Al layer on the test wafers.
If necessary, perform a target clean with recipes '**_Trgt_Cln_Ti_50C**' and '**_Trgt_Cln_AlSi_50'**.

Choose:

Use recipe '**Ti100nmAl675-50C**' for titanium and aluminum with 1% silicon or,
Use recupe '**Ti100nmpAl675-50C**' for titanium and aluminum

Visual inspection: the metal layer must look shiny.

22. MANUAL COATING AND BAKING

• Front side

Prepare the brewer manual spinner with aluminum foil
Keep gloves clean when using the screen. Use chuck for contaminated wafers!

HMDS treatment	Treat wafers with HMDS (hexamethyldisilazane) vapor with nitrogen as a carrier gas for **10 mins**. Use cassette for contaminated wafers.
Photoresist coating	Use photoresist AZ3027. Do a test run with a dummy wafer without photoresist before starting. When using the spinner, press the vacuum then close the lid, otherwise the software will get stuck.
Soft Bake	Soft bake the wafer on a hot plate for contaminated wafers at **95 deg. C for 1 min**. Use carrier wafers for contaminated wafers

Use coating **'AZ_ECI-3027-3100nm'** (resist thickness: 3.10µm).

23. ALIGNMENT AND EXPOSURE

• Front side

Use the SUSS MicroTec MA/BA8 mask aligner to expose the photoresist.
Use **foil mask layer METAL**. Use the contaminated chuck for this step.

Use recipe '**1_FSA_Soft_Contact**'
Calculate the exposure time by consulting the contact aligner exposure energy data log.

24. MANUAL DEVELOPMENT • Front side

Post-exposure baking	Bake at 115 deg. C for 1 min
Photoresist development	Use Shipley MF322 developer for 1 min. Make sure not to overdevelop.
Dry	Spin dry the wafer spin. Use the contaminated chuck for the spin dryer.
Inspection	Visually inspect the wafers through a microscope and check the openings.
Hard baking	Bake **100 deg. C for 1 min.** Use the hot plate for contaminated wafers.
Inspection	Visually inspect the wafers through a microscope and check openings.

25. ETCHING OF Ti+Al • Front side

Perform an extra baking step for **30 mins at 115 deg. C**. Using the Memmert Oven. Use the cassette for contaminated wafers.

Perform this step in SAL. Use HF 0.55% for metal etching for ~15 min, but this differs between wafers and batches. Check the wafer every other minute or so and check the etching rate.

26. MANUAL LAYER STRIPPING: Photoresist • Front side

Submerge the wafers in acetone then followed by IPA for **3 mins each** to remove the remaining photoresist. Manually rinse and then spin dry.

PART 6: PHOTORESIST DEPOSITION AND PATTERNING

27. MANUAL COATING AND BAKING • Front side

Prepare the brewer manual spinner with aluminum foil
Keep gloves clean when using the screen. Use chuck for contaminated wafers!

HMDS treatment	Treat wafers with HMDS (hexamethyldisilazane) vapor with nitrogen as a carrier gas for 10 mins. Use cassette for contaminated wafers.
Photoresist coating	Use photoresist AZ3027. Do a test run with a dummy wafer without photoresist before starting. When using the spinner, press the vacuum then close the lid, otherwise the software will get stuck.
Soft Bake	Soft bake the wafer on a hot plate for contaminated wafers at **95 deg. C for 1 min**. Use carrier wafers for contaminated wafers

Use coating **'AZ_ECI-3027-3100nm'** (resist thickness: 3.10µm).

28. ALIGNMENT AND EXPOSURE • Front side

Use the SUSS MicroTec MA/BA8 mask aligner to expose the photoresist.
Use chuck for contaminated wafers!

Choose:

Option 1: Use **foil mask layer PDMS openings**. *(This is just the label of the mask and for the purpose of this research, photoresist will be used for the polymeric encapsulation instead of PDMS)* or

Option 2: Use **mask** for device BE2325, layer **PDMS. Proceed to Step 29 Development.** Use **foil mask layer PDMS openings2** *(This is just the label of the mask and for the purpose of this research, photoresist will be used for the polymeric encapsulation instead of PDMS).* **Repeat Step 29 Development**. or

Option 3: Use **foil mask layer PDMS openings 25um diam.** *(This is just the label of the mask and for the purpose of this research, photoresist will be used for the polymeric encapsulation instead of PDMS*). or

Option 4: Use **foil mask layer PDMS openings 50x50um square.** *(This is just the label of the mask and for the purpose of this research, photoresist will be used for the polymeric encapsulation instead of PDMS)*

Use recipe ‘**1_FSA_Soft_Contact**’
Calculate the exposure time by consulting the contact aligner exposure energy data log.

29. MANUAL DEVELOPMENT • Front side

Post Exposure Baking	Bake at **115 deg. C for 1 min**
Photoresist Development	Use Shipley MF322 developer for 1 min. Make sure not to overdevelop. Rinse gently since graphene can be fragile and then spin dry. Use the contaminated chuck for the spin dryer.
Hard Baking	Bake **100 deg. C for 1 min.** Use the hot plate for contaminated wafers.
Inspection	Visually inspect the wafers through a microscope and check openings.

Return to Step 28 Option 2 if this was initially chosen

PART 7: MOLYBDENUM REMOVAL

30. CUTTING THE WAFERS • Front side

Manually cut the wafers into separate device structures. Make a scratch with the scriber on the back. Label each device.

31. Mo REMOVAL • Front side

Perform this step in SAL.

Use hydrogen peroxide to remove the Mo layer under graphene. Do not spin dry or blow dry the samples because the graphene can be delicate. Do not directly introduce water over the graphene. Check the device every minute or so and check the etching rate.

PART 8: NANOPARTICLE PRINTING

32. NANOPARTICLE PRINTING • Front side

Use the VS-Particle machine to print nanoparticles (Pt) on the separated device structures.

33. DIE ATTACHMENT

Use epoxy die adhesive to attach one device to the PCB. Do not use it immediately on the die because it is too thin. Wait one hour, so the epoxy is more viscous before applying, otherwise, it might slide up on the PCB’s bond pad. Be sure the device is glued flat on the PCB.

34. WIRE BONDING • Front side

Wirebond	Bond wires using the TPT Al/Au bonder. Use the following settings: YWay Auto: 1100 Loop Height (Looph): 1200
Insulate the Wirebond	Add a drop of PDMS on the bond pad to make it mechanically stable and leave it for several hours to dry.

To make PDMS:

Use SYLGARD 184 Silicone Elastomer
The base (part A) and curing agent (part B) are mixed in 10:1 mass ratio, respectively.
Use the automatic spinner for mixing. Be sure that the container is securely closed and snug inside the automatic spinner’s holder before starting the spin. Clean the work area with acetone afterward. Do not use it immediately on the wire because it is too thin. Wait one hour, so the PDMS is more viscous before applying.

B

Visual Representation of the Flowchart

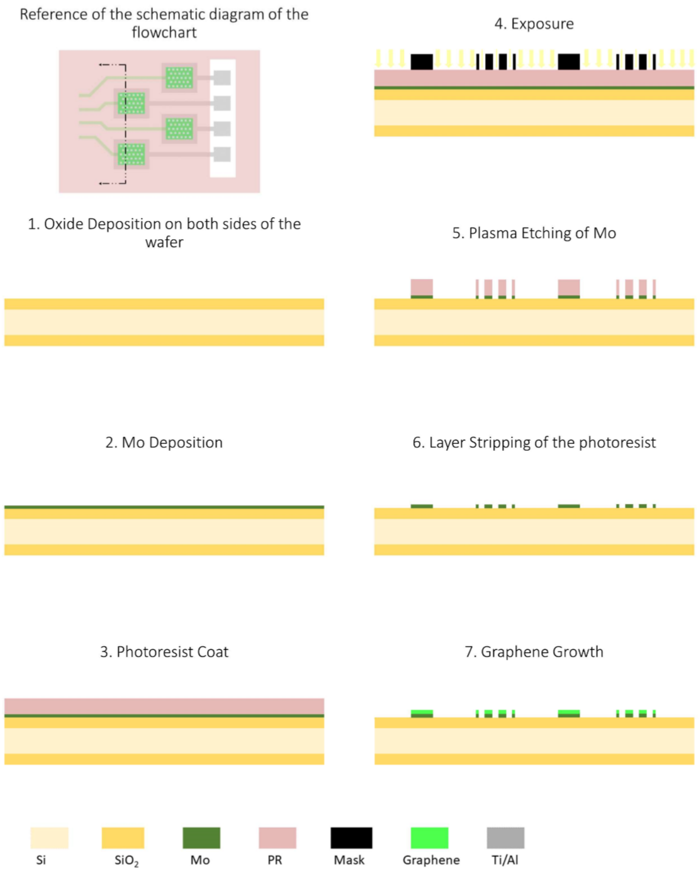

Figure B.1: Part 1 of the schematic diagram of the complete fabrication process represented through the cross-section of the device contact pad. The reference is presented at the top right, where the *white space* is also SiO_2 and the yellow color was removed for better contrast between the structural layers.

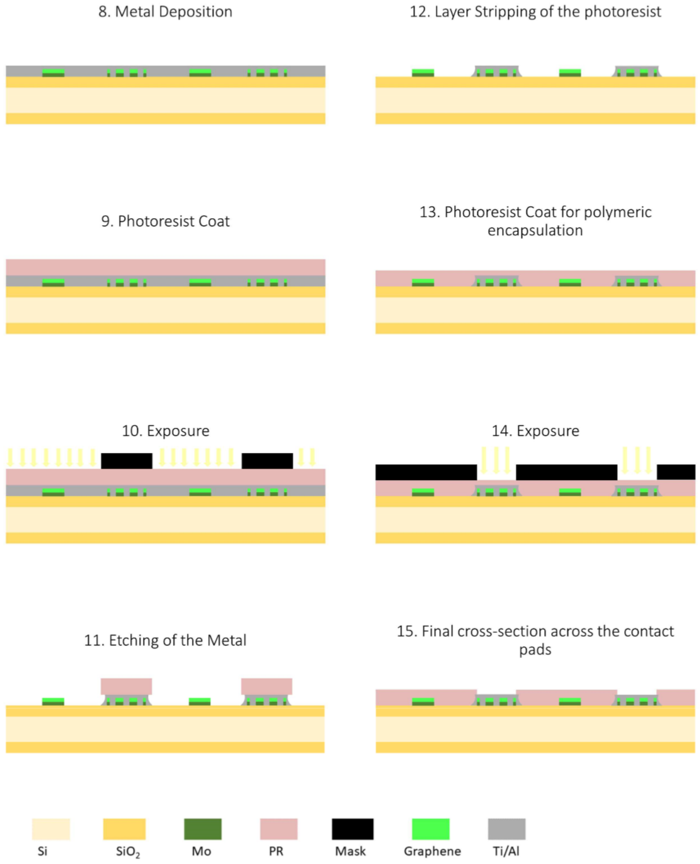

Figure B.2: Part 2 of the schematic diagram of the complete fabrication process represented through the cross-section of the device contact pad

C

Script for calculating Nanoparticle Density

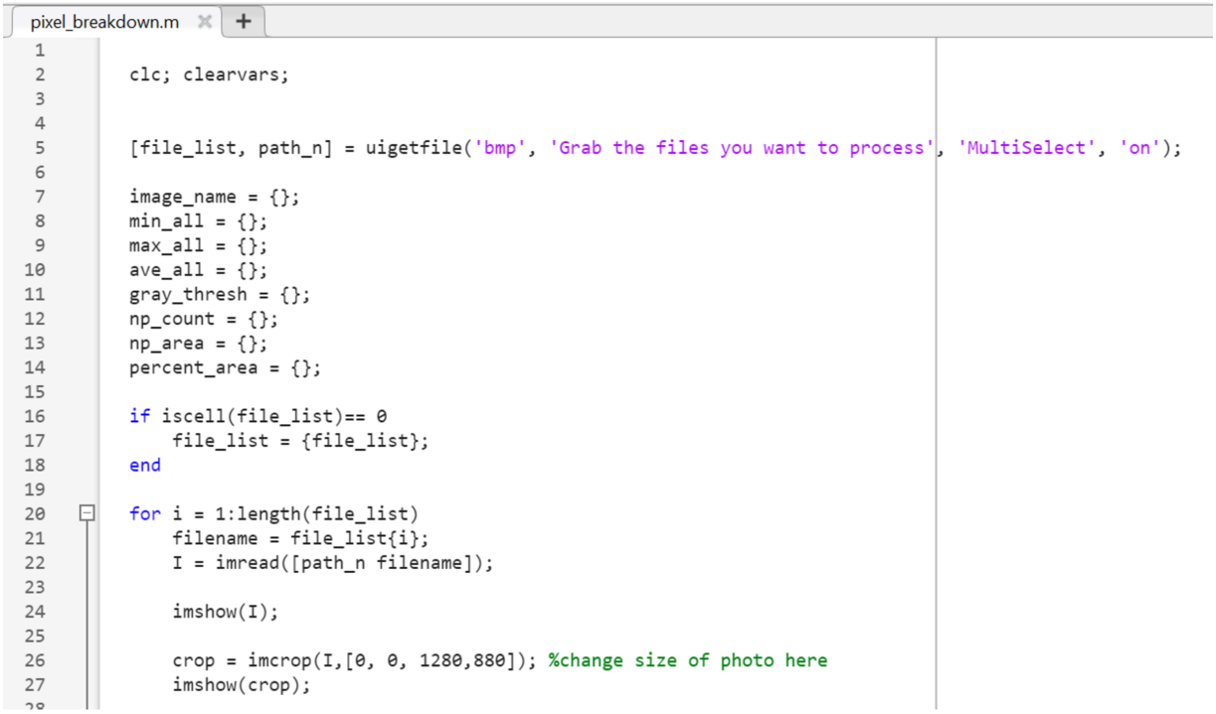

```

clc; clearvars;


[file_list, path_n] = uigetfile('bmp', 'Grab the files you want to process', 'MultiSelect', 'on');

image_name = {};
min_all = {};
max_all = {};
ave_all = {};
gray_thresh = {};
np_count = {};
np_area = {};
percent_area = {};

if iscell(file_list)== 0
    file_list = {file_list};
end

for i = 1:length(file_list)
    filename = file_list{i};
    I = imread([path_n filename]);

    imshow(I);

    crop = imcrop(I,[0, 0, 1280,880]); %change size of photo here
    imshow(crop);
```

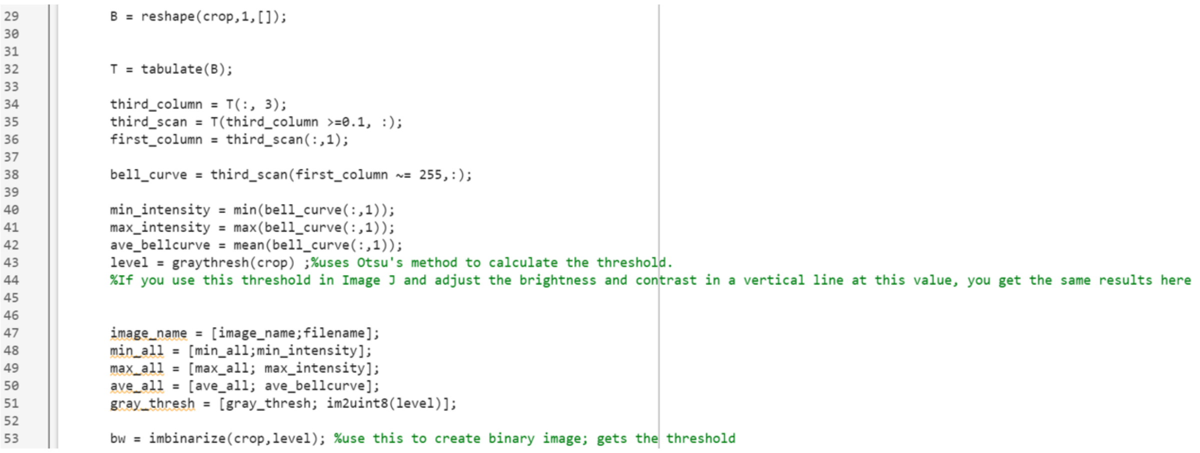

```
    B = reshape(crop,1,[]);


    T = tabulate(B);

    third_column = T(:, 3);
    third_scan = T(third_column >=0.1, :);
    first_column = third_scan(:,1);

    bell_curve = third_scan(first_column ~= 255,:);

    min_intensity = min(bell_curve(:,1));
    max_intensity = max(bell_curve(:,1));
    ave_bellcurve = mean(bell_curve(:,1));
    level = graythresh(crop) ;%uses Otsu's method to calculate the threshold.
    %If you use this threshold in Image J and adjust the brightness and contrast in a vertical line at this value, you get the same results here


    image_name = [image_name;filename];
    min_all = [min_all;min_intensity];
    max_all = [max_all; max_intensity];
    ave_all = [ave_all; ave_bellcurve];
    gray_thresh = [gray_thresh; im2uint8(level)];

    bw = imbinarize(crop,level); %use this to create binary image; gets the threshold
```

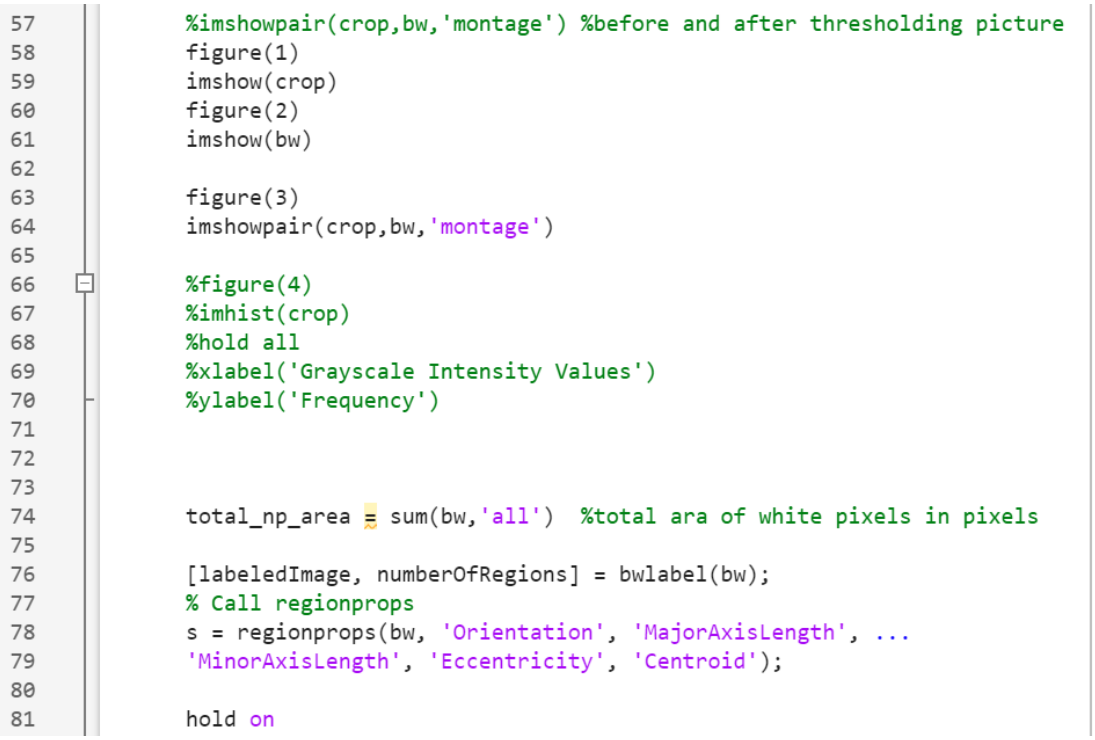

```
    %imshowpair(crop,bw,'montage') %before and after thresholding picture
    figure(1)
    imshow(crop)
    figure(2)
    imshow(bw)

    figure(3)
    imshowpair(crop,bw,'montage')

    %figure(4)
    %imhist(crop)
    %hold all
    %xlabel('Grayscale Intensity Values')
    %ylabel('Frequency')



    total_np_area = sum(bw,'all')  %total ara of white pixels in pixels

    [labeledImage, numberOfRegions] = bwlabel(bw);
    % Call regionprops
    s = regionprops(bw, 'Orientation', 'MajorAxisLength', ...
    'MinorAxisLength', 'Eccentricity', 'Centroid');

    hold on
```

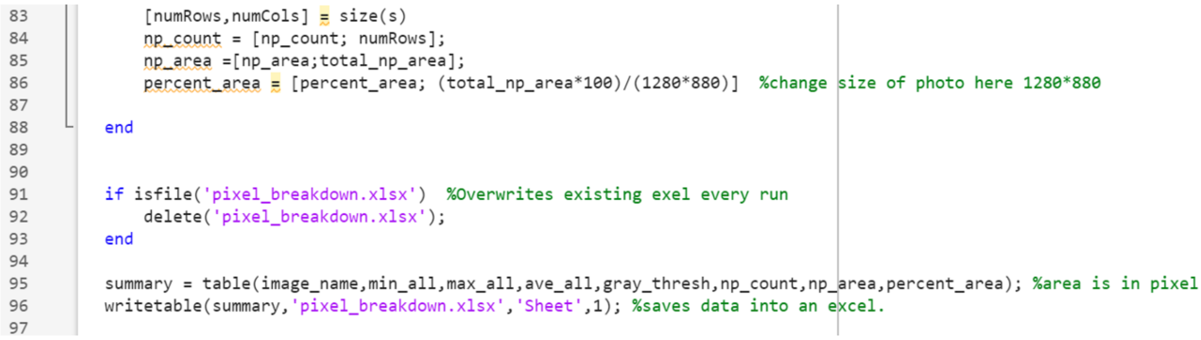

```
    [numRows,numCols] = size(s)
    np_count = [np_count; numRows];
    np_area =[np_area;total_np_area];
    percent_area = [percent_area; (total_np_area*100)/(1280*880)]  %change size of photo here 1280*880

end


if isfile('pixel_breakdown.xlsx')  %Overwrites existing exel every run
    delete('pixel_breakdown.xlsx');
end

summary = table(image_name,min_all,max_all,ave_all,gray_thresh,np_count,np_area,percent_area); %area is in pixel
writetable(summary,'pixel_breakdown.xlsx','Sheet',1); %saves data into an excel.

```

D

Script for calculating Nanoparticle Deposition Width

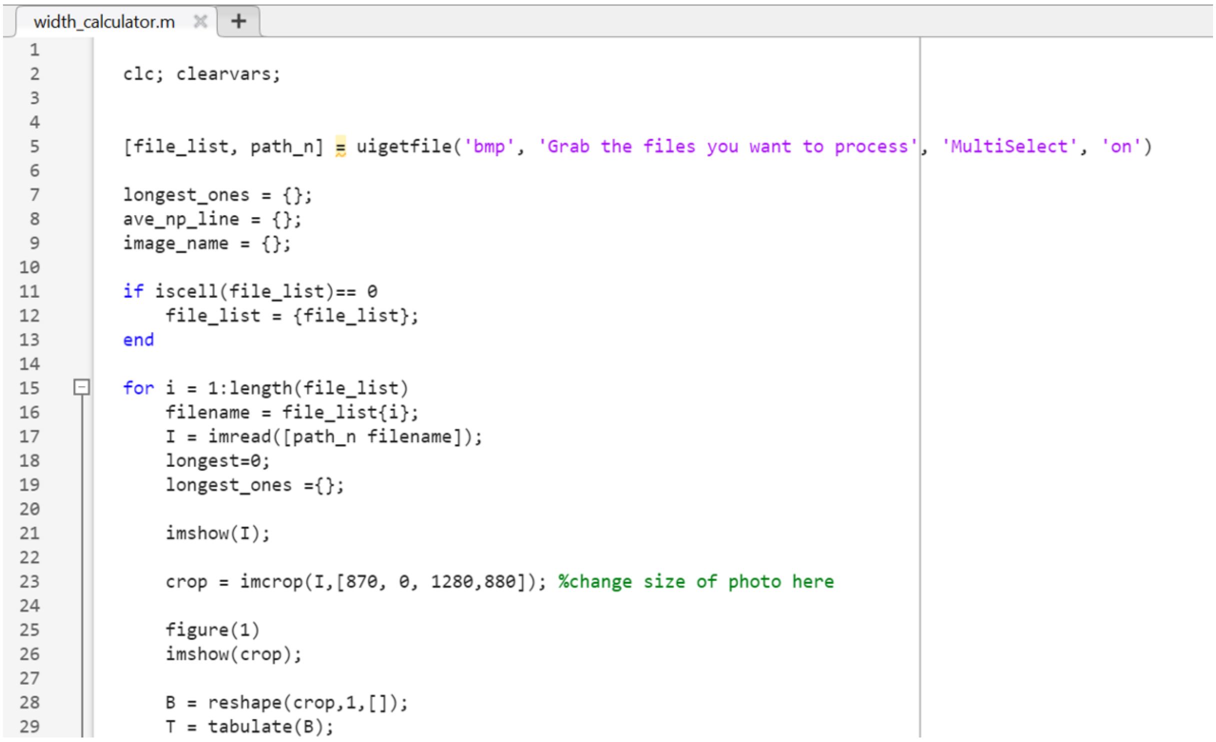

```
clc; clearvars;


[file_list, path_n] = uigetfile('bmp', 'Grab the files you want to process', 'MultiSelect', 'on')

longest_ones = {};
ave_np_line = {};
image_name = {};

if iscell(file_list)== 0
    file_list = {file_list};
end

for i = 1:length(file_list)
    filename = file_list{i};
    I = imread([path_n filename]);
    longest=0;
    longest_ones ={};

    imshow(I);

    crop = imcrop(I,[870, 0, 1280,880]); %change size of photo here

    figure(1)
    imshow(crop);

    B = reshape(crop,1,[]);
    T = tabulate(B);
```

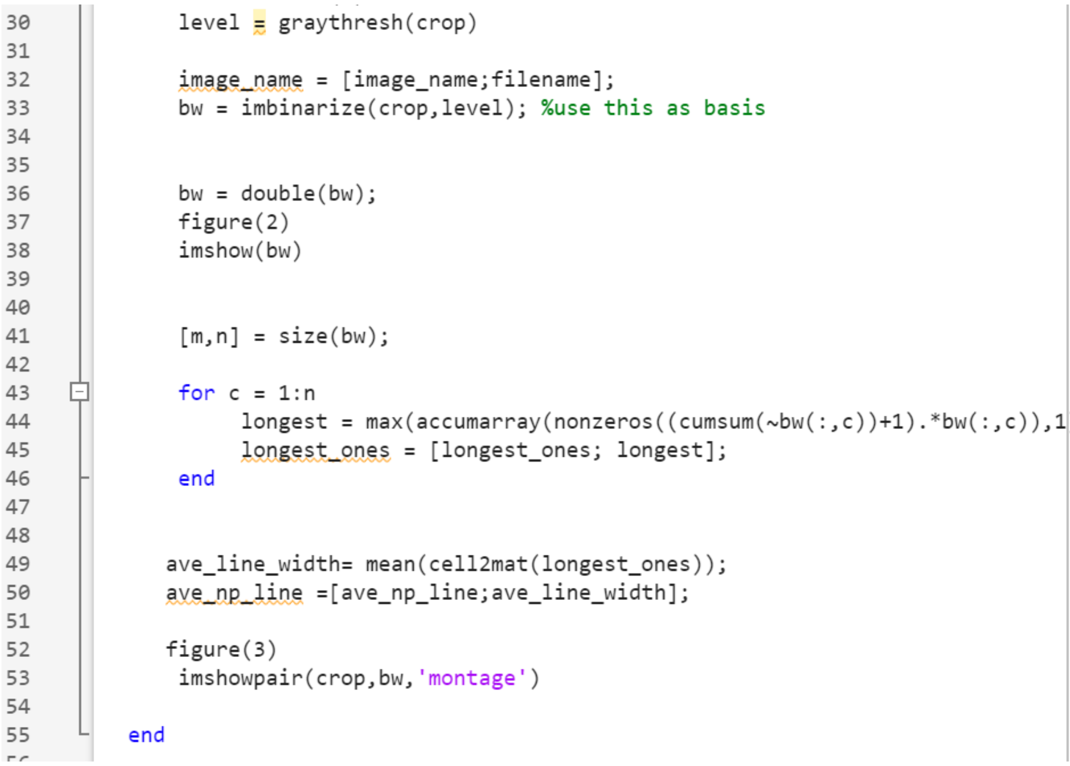

```
        level = graythresh(crop)

        image_name = [image_name;filename];
        bw = imbinarize(crop,level); %use this as basis


        bw = double(bw);
        figure(2)
        imshow(bw)


        [m,n] = size(bw);

        for c = 1:n
             longest = max(accumarray(nonzeros((cumsum(~bw(:,c))+1).*bw(:,c)),1));
             longest_ones = [longest_ones; longest];
        end


       ave_line_width= mean(cell2mat(longest_ones));
       ave_np_line =[ave_np_line;ave_line_width];

       figure(3)
        imshowpair(crop,bw,'montage')

    end
```

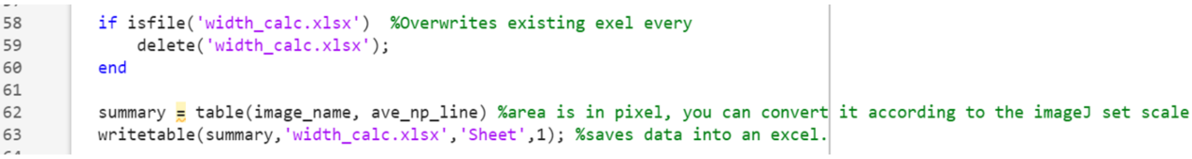

```
if isfile('width_calc.xlsx')  %Overwrites existing exel every
    delete('width_calc.xlsx');
end

summary = table(image_name, ave_np_line) %area is in pixel, you can convert it according to the imageJ set scale
writetable(summary,'width_calc.xlsx','Sheet',1); %saves data into an excel.
```

E

Script for calculating Charge Storage Capacity

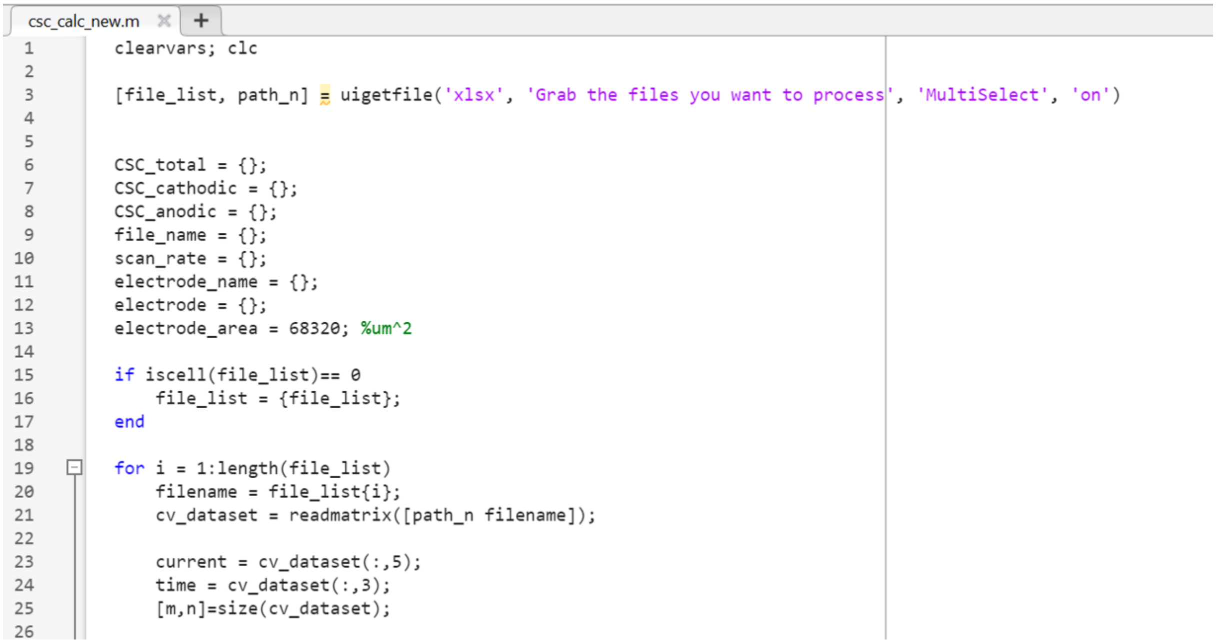

```
clearvars; clc

[file_list, path_n] = uigetfile('xlsx', 'Grab the files you want to process', 'MultiSelect', 'on')


CSC_total = {};
CSC_cathodic = {};
CSC_anodic = {};
file_name = {};
scan_rate = {};
electrode_name = {};
electrode = {};
electrode_area = 68320; %um^2

if iscell(file_list)== 0
    file_list = {file_list};
end

for i = 1:length(file_list)
    filename = file_list{i};
    cv_dataset = readmatrix([path_n filename]);

    current = cv_dataset(:,5);
    time = cv_dataset(:,3);
    [m,n]=size(cv_dataset);

```

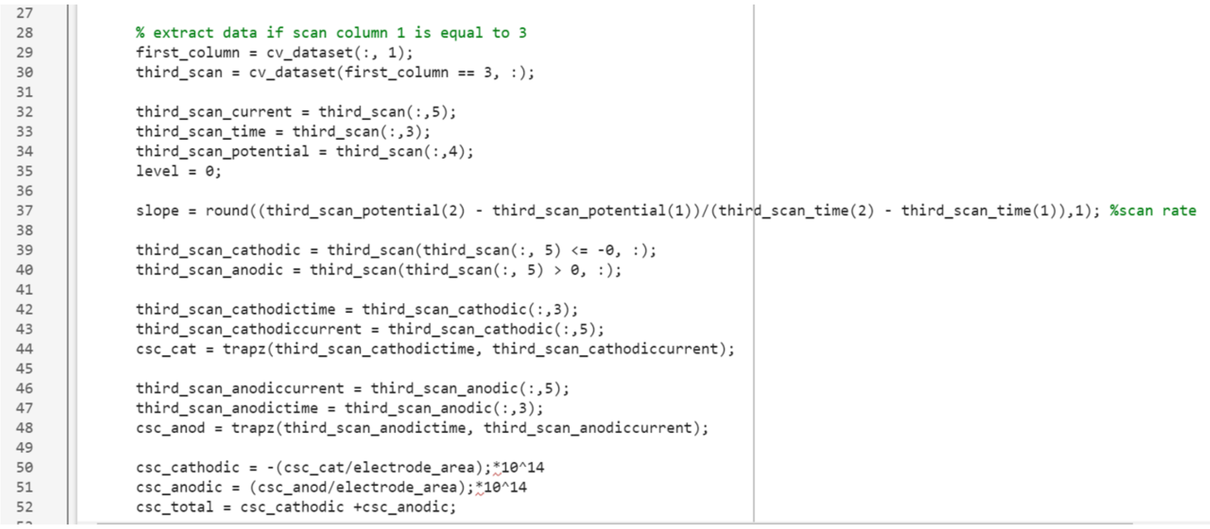

```
    % extract data if scan column 1 is equal to 3
    first_column = cv_dataset(:, 1);
    third_scan = cv_dataset(first_column == 3, :);

    third_scan_current = third_scan(:,5);
    third_scan_time = third_scan(:,3);
    third_scan_potential = third_scan(:,4);
    level = 0;

    slope = round((third_scan_potential(2) - third_scan_potential(1))/(third_scan_time(2) - third_scan_time(1)),1); %scan rate

    third_scan_cathodic = third_scan(third_scan(:, 5) <= -0, :);
    third_scan_anodic = third_scan(third_scan(:, 5) > 0, :);

    third_scan_cathodictime = third_scan_cathodic(:,3);
    third_scan_cathodiccurrent = third_scan_cathodic(:,5);
    csc_cat = trapz(third_scan_cathodictime, third_scan_cathodiccurrent);

    third_scan_anodiccurrent = third_scan_anodic(:,5);
    third_scan_anodictime = third_scan_anodic(:,3);
    csc_anod = trapz(third_scan_anodictime, third_scan_anodiccurrent);

    csc_cathodic = -(csc_cat/electrode_area);*10^14
    csc_anodic = (csc_anod/electrode_area);*10^14
    csc_total = csc_cathodic +csc_anodic;
```

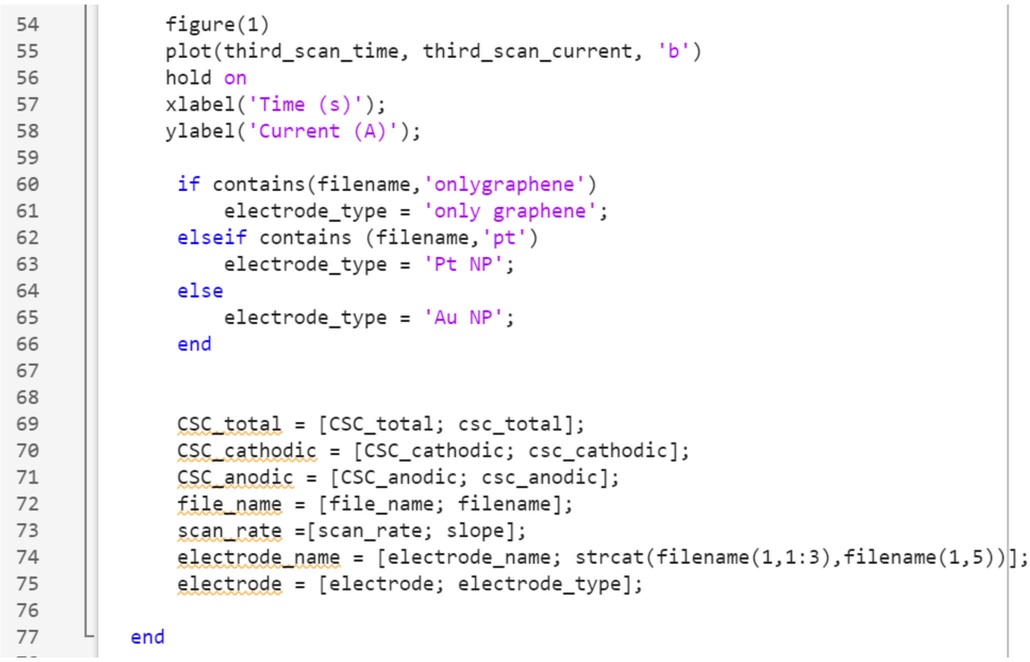

```
   figure(1)
   plot(third_scan_time, third_scan_current, 'b')
   hold on
   xlabel('Time (s)');
   ylabel('Current (A)');

    if contains(filename,'onlygraphene')
        electrode_type = 'only graphene';
    elseif contains (filename,'pt')
        electrode_type = 'Pt NP';
    else
        electrode_type = 'Au NP';
    end


    CSC_total = [CSC_total; csc_total];
    CSC_cathodic = [CSC_cathodic; csc_cathodic];
    CSC_anodic = [CSC_anodic; csc_anodic];
    file_name = [file_name; filename];
    scan_rate =[scan_rate; slope];
    electrode_name = [electrode_name; strcat(filename(1,1:3),filename(1,5))];
    electrode = [electrode; electrode_type];

end
```

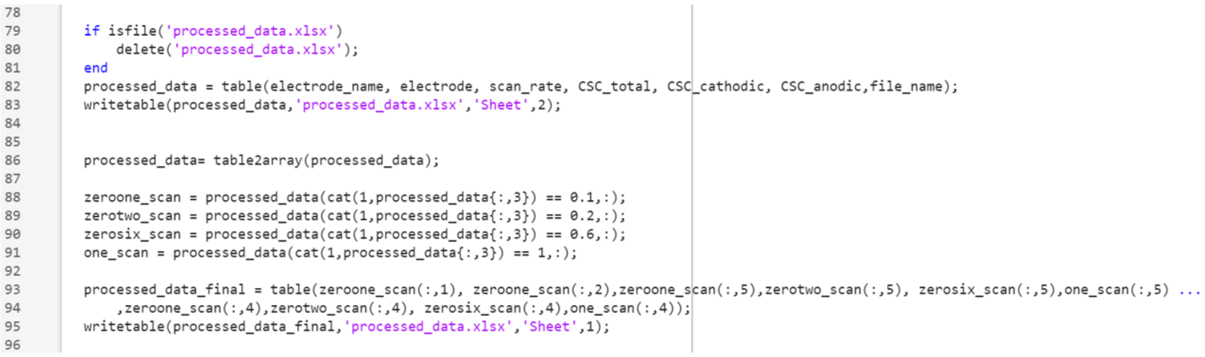

```
if isfile('processed_data.xlsx')
    delete('processed_data.xlsx');
end
processed_data = table(electrode_name, electrode, scan_rate, CSC_total, CSC_cathodic, CSC_anodic,file_name);
writetable(processed_data,'processed_data.xlsx','Sheet',2);


processed_data= table2array(processed_data);

zeroone_scan = processed_data(cat(1,processed_data{:,3}) == 0.1,:);
zerotwo_scan = processed_data(cat(1,processed_data{:,3}) == 0.2,:);
zerosix_scan = processed_data(cat(1,processed_data{:,3}) == 0.6,:);
one_scan = processed_data(cat(1,processed_data{:,3}) == 1,:);

processed_data_final = table(zeroone_scan(:,1), zeroone_scan(:,2),zeroone_scan(:,5),zerotwo_scan(:,5), zerosix_scan(:,5),one_scan(:,5) ...
    ,zeroone_scan(:,4),zerotwo_scan(:,4), zerosix_scan(:,4),one_scan(:,4));
writetable(processed_data_final,'processed_data.xlsx','Sheet',1);
```

Bibliography

[1] M. Raghavan, D. Fee, and P. E. Barkhaus, “Generation and propagation of the action potential,” *Clinical Neurophysiology: Basis and Technical Aspects*, pp. 3–22, 2019. DOI: `10.1016/b978-0-444-64032-1.00001-1`.

[2] *Overview of neuron structure and function - khan academy*. [Online]. Available: `https://www.khanacademy.org/science/biology/human-biology/neuron-nervous-system/a/overview-of-neuron-structure-and-function`.

[3] D.-W. Park, A. A. Schendel, S. Mikael, *et al.*, “Graphene-based carbon-layered electrode array technology for neural imaging and optogenetic applications,” *Nature Communications*, vol. 5, 2014. DOI: `10.1038/ncomms6258`. [Online]. Available: `www.nature.com/naturecommunications`.

[4] D. Kuzum, H. Takano, E. Shim, *et al.*, “Transparent and flexible low noise graphene electrodes for simultaneous electrophysiology and neuroimaging,” *Nature Communications*, 2014. DOI: `10.1038/ncomms6259`. [Online]. Available: `www.nature.com/naturecommunications`.

[5] E. S. Boyden, F. Zhang, E. Bamberg, G. Nagel, and K. Deisseroth, “Millisecond-timescale, genetically targeted optical control of neural activity,” *Nature Neuroscience*, vol. 8, no. 9, pp. 1263–1268, Aug. 2005. DOI: `10.1038/nn1525`. [Online]. Available: `http://dx.doi.org/10.1038/nn1525`.

[6] J. Mattis, K. M. Tye, E. A. Ferenczi, *et al.*, “Principles for applying optogenetic tools derived from direct comparative analysis of microbial opsins,” *Nature Methods*, vol. 9, no. 2, pp. 159–172, 2011. DOI: `10.1038/nmeth.1808`.

[7] J. Nakai, M. Ohkura, and K. Imoto, “A high signal-to-noise ca2+ probe composed of a single green fluorescent protein,” *Nature Biotechnology*, vol. 19, no. 2, pp. 137–141, 2001. DOI: `10.1038/84397`.

[8] A. Muto, M. Ohkura, T. Kotani, S.-i. Higashijima, J. Nakai, and K. Kawakami, “Genetic visualization with an improved gcamp calcium indicator reveals spatiotemporal activation of the spinal motor neurons in zebrafish,” *Proceedings of the National Academy of Sciences*, vol. 108, no. 13, pp. 5425–5430, 2011. DOI: `10.1073/pnas.1000887108`.

[9] L. Tian, S. A. Hires, T. Mao, *et al.*, “Imaging neural activity in worms, flies and mice with improved gcamp calcium indicators,” *Nature Methods*, vol. 6, no. 12, pp. 875–881, 2009. DOI: `10.1038/nmeth.1398`.

[10] G. Eichhoff, M. A. Busche, and O. Garaschuk, “In vivo calcium imaging of the aging and diseased brain,” *European Journal of Nuclear Medicine and Molecular Imaging*, vol. 35, no. S1, pp. 99–106, 2008. DOI: `10.1007/s00259-007-0709-6`.

[11] J. P. Hamm, D. S. Peterka, J. A. Gogos, and R. Yuste, “Altered cortical ensembles in mouse models of schizophrenia,” *Neuron*, vol. 94, no. 1, 2017. DOI: `10.1016/j.neuron.2017.03.019`.

[12] T. J. Richner, S. Thongpang, S. K. Brodnick, *et al.*, “Optogenetic micro-electrocorticography for modulating and localizing cerebral cortex activity,” *Journal of Neural Engineering*, vol. 11, no. 1, p. 016 010, 2014. DOI: `10.1088/1741-2560/11/1/016010`.

[13] S. Bae, H. Kim, Y. Lee, *et al.*, “Roll-to-roll production of 30-inch graphene films for transparent electrodes,” 2010. DOI: `10.1038/NNANO.2010.132`. [Online]. Available: `www.nature.com/naturenanotechnology`.

[14] Z. Jia, C. Peng, J. Lou, and T. Li, “A map of competing buckling-driven failure modes of substrate-supported thin brittle films,” *Thin Solid Films*, vol. 520, no. 21, pp. 6576–6580, 2012. DOI: `10.1016/j.tsf.2012.07.011`.

[15] N. Bakhshaee Babaroud, M. Palmar, A. I. Velea, *et al.*, “Multilayer cvd graphene electrodes using a transfer-free process for the next generation of optically transparent and mri-compatible neural interfaces,” *Microsystems amp; Nanoengineering*, vol. 8, no. 1, 2022. DOI: `10.1038/s41378-022-00430-x`.

[16] X. Liu, Y. Lu, E. Iseri, Y. Shi, and D. Kuzum, “A compact closed-loop optogenetics system based on artifact-free transparent graphene electrodes,” *Frontiers in Neuroscience*, vol. 12, 2018. DOI: `10.3389/fnins.2018.00132`.

[17] Y. U. Cho, J. Y. Lee, U.-J. Jeong, *et al.*, “Ultra□low cost, facile fabrication of transparent neural electrode array for electrocorticography with photoelectric artifact□free optogenetics,” *Advanced Functional Materials*, vol. 32, no. 10, p. 2 105 568, 2021. DOI: `10.1002/adfm.202105568`.

[18] H. Teixeira, C. Dias, R. Veloso, A. Apolinário, and J. Ventura, “Tuning pedot:pss low-impedance thin films with high charge injection for microelectrodes applications,” *Progress in Organic Coatings*, vol. 168, p. 106 894, 2022. DOI: `10.1016/j.porgcoat.2022.106894`.

[19] A. Ambrosi, C. K. Chua, A. Bonanni, and M. Pumera, “Electrochemistry of graphene and related materials,” *Chemical Reviews*, vol. 114, no. 14, pp. 7150–7188, 2014, PMID: 24895834. DOI: `10.1021/cr500023c`. eprint: `https://doi.org/10.1021/cr500023c`. [Online]. Available: `https://doi.org/10.1021/cr500023c`.

[20] M. Thunemann, Y. Lu, X. Liu, *et al.*, “Deep 2-photon imaging and artifact-free optogenetics through transparent graphene microelectrode arrays,” 2018. DOI: `10.1038/s41467-018-04457-5`. [Online]. Available: `www.nature.com/naturecommunications`.

[21] D.-W. Park, J. P. Ness, S. K. Brodnick, *et al.*, “Electrical neural stimulation and simultaneous in vivo monitoring with transparent graphene electrode arrays implanted in gcamp6f mice,” 2017. DOI: `10.1021/acsnano.7b04321`. [Online]. Available: `www.acsnano.org`.

[22] A. Urban, A. Rancillac, L. Martinez, J. Rossier, Y. Zilberter, and E. Sanna, “Deciphering the neuronal circuitry controlling local blood flow in the cerebral cortex with optogenetics in pv::cre transgenic mice,” 2012. DOI: `10.3389/fphar.2012.00105`. [Online]. Available: `www.frontiersin.org`.

[23] C. Boehler, S. Carli, L. Fadiga, T. Stieglitz, and M. Asplund, “Tutorial: Guidelines for standardized performance tests for electrodes intended for neural interfaces and bioelectronics,” *Nature Protocols*, vol. 15, no. 11, pp. 3557–3578, 2020. DOI: `10.1038/s41596-020-0389-2`.

[24] J. K. Niparko, R. A. Altschuler, J. A. Wiler, X. Xue, and D. J. Anderson, “Surgical implantation and biocompatibility of central nervous system auditory prostheses,” *Annals of Otology, Rhinology & Laryngology*, vol. 98, no. 12, pp. 965–970, 1989, PMID: 2589766. DOI: `10.1177/000348948909801209`. eprint: `https://doi.org/10.1177/000348948909801209`. [Online]. Available: `https://doi.org/10.1177/000348948909801209`.

[25] Y. T. Kim, R. W. Hitchcock, M. J. Bridge, and P. A. Tresco, “Chronic response of adult rat brain tissue to implants anchored to the skull,” *Biomaterials*, vol. 25, pp. 2229–2237, 12 May 2004, ISSN: 0142-9612. DOI: `10.1016/J.BIOMATERIALS.2003.09.010`.

[26] K. Wang, C. L. Frewin, D. Esrafilzadeh, *et al.*, “High-performance graphene-fiber-based neural recording microelectrodes,” 2019. DOI: `10.1002/adma.201805867`. [Online]. Available: `https://doi.org/10.1002/adma.201805867.`.

[27] V.-D. Dao, L. V. Nang, E.-T. Kim, J.-K. Lee, and H.-S. Choi, “Pt nanoparticles immobilized on cvd-grown graphene as a transparent counter electrode material for dye-sensitized solar cells,” *ChemSusChem*, vol. 6, no. 8, pp. 1316–1319, 2013. DOI: `10.1002/cssc.201300353`.

[28] Y. Lu, X. Liu, R. Hattori, *et al.*, “Ultralow impedance graphene microelectrodes with high optical transparency for simultaneous deep two□photon imaging in transgenic mice,” *Advanced Functional Materials*, vol. 28, no. 31, p. 1 800 002, 2018. DOI: `10.1002/adfm.201800002`.

[29] G. Schiavone, X. Kang, F. Fallegger, J. Gandar, G. Courtine, and S. P. Lacour, “Guidelines to study and develop soft electrode systems for neural stimulation,” *Neuron*, vol. 108, no. 2, pp. 238–258, 2020, ISSN: 0896-6273. DOI: `https://doi.org/10.1016/j.neuron.2020.10.010`. [Online]. Available: `https://www.sciencedirect.com/science/article/pii/S0896627320308060`.

[30] N. P. Aryan, H. Kaim, and A. Rothermel, “Stimulation and recording electrodes: General concepts,” in *Stimulation and Recording Electrodes for Neural Prostheses*. Cham: Springer International Publishing, 2015, pp. 1–9, ISBN: 978-3-319-10052-4. DOI: `10.1007/978-3-319-10052-4_1`. [Online]. Available: `https://doi.org/10.1007/978-3-319-10052-4_1`.

[31] D. R. Merrill, M. Bikson, and J. G. Jefferys, “Electrical stimulation of excitable tissue: Design of efficacious and safe protocols,” *Journal of Neuroscience Methods*, vol. 141, no. 2, pp. 171–198, 2005. DOI: `10.1016/j.jneumeth.2004.10.020`.

[32] Feb. 2001. [Online]. Available: `https://www.palmsens.com/knowledgebase-article/bode-and-nyquist-plot/`.

[33] N. Elgrishi, K. J. Rountree, B. D. McCarthy, E. S. Rountree, T. T. Eisenhart, and J. L. Dempsey, “A practical beginner’s guide to cyclic voltammetry,” *Journal of Chemical Education*, vol. 95, no. 2, pp. 197–206, 2017. DOI: `10.1021/acs.jchemed.7b00361`.

[34] S. F. Cogan, “Neural stimulation and recording electrodes,” *Annual Review of Biomedical Engineering*, vol. 10, no. 1, pp. 275–309, 2008, PMID: 18429704. DOI: `10.1146/annurev.bioeng.10.061807.160518`. eprint: `https://doi.org/10.1146/annurev.bioeng.10.061807.160518`. [Online]. Available: `https://doi.org/10.1146/annurev.bioeng.10.061807.160518`.

[35] W. M. Grill, S. E. Norman, and R. V. Bellamkonda, “Implanted neural interfaces: Biochallenges and engineered solutions,” *Annual Review of Biomedical Engineering*, vol. 11, no. 1, pp. 1–24, 2009, PMID: 19400710. DOI: `10.1146/annurev-bioeng-061008-124927`. eprint: `https://doi.org/10.1146/annurev-bioeng-061008-124927`. [Online]. Available: `https://doi.org/10.1146/annurev-bioeng-061008-124927`.

[36] S. F. Cogan, A. A. Guzelian, W. F. Agnew, T. G. Yuen, and D. B. McCreery, “Over-pulsing degrades activated iridium oxide films used for intracortical neural stimulation,” *Journal of Neuroscience Methods*, vol. 137, no. 2, pp. 141–150, 2004, ISSN: 0165-0270. DOI: `https://doi.org/10.1016/j.jneumeth.2004.02.019`. [Online]. Available: `https://www.sciencedirect.com/science/article/pii/S0165027004000913`.

[37] S. M. Lee, H. J. Byeon, B. H. Kim, *et al.*, “Flexible and implantable capacitive microelectrode for bio-potential acquisition,” *BioChip Journal*, vol. 11, no. 2, pp. 153–163, 2017. DOI: `10.1007/s13206-017-1304-y`.

[38] N. Lago and A. Cester, “Flexible and organic neural interfaces: A review,” *Applied Sciences*, vol. 7, no. 12, p. 1292, 2017. DOI: `10.3390/app7121292`.

[39] K. Wise, D. Anderson, J. Hetke, D. Kipke, and K. Najafi, “Wireless implantable microsystems: High-density electronic interfaces to the nervous system,” *Proceedings of the IEEE*, vol. 92, no. 1, pp. 76–97, 2004. DOI: `10.1109/jproc.2003.820544`.

[40] M. M. Kohonen, M. E. Karaman, and R. M. Pashley, “Debye length in multivalent electrolyte solutions,” *Langmuir*, vol. 16, no. 13, pp. 5749–5753, 2000. DOI: `10.1021/la991621c`.

[41] K. S. Novoselov, A. K. Geim, S. V. Morozov, *et al.*, “Electric field effect in atomically thin carbon films,” *Science*, vol. 306, no. 5696, pp. 666–669, 2004. DOI: `10.1126/science.1102896`.

[42] W. Choi, I. Lahiri, R. Seelaboyina, and Y. S. Kang, “Synthesis of graphene and its applications: A review,” *Critical Reviews in Solid State and Materials Sciences*, vol. 35, no. 1, pp. 52–71, 2010. DOI: `10.1080/10408430903505036`.

[43] M. Birowska, K. Milowska, and J. Majewski, “Van der waals density functionals for graphene layers and graphite,” *Acta Physica Polonica A*, vol. 120, no. 5, pp. 845–848, 2011. DOI: `10.12693/aphyspola.120.845`.

[44] “Structure and properties of graphene,” in *Graphene: An introduction to the fundamentals and industrial applications*. Scrivener Publishing, 2015, pp. 26–48.

[45] S. Vollebregt, B. Alfano, F. Ricciardella, *et al.*, *A transfer-free wafer-scale CVD graphene fabrication process for MEMS/NEMS sensors; A transfer-free wafer-scale CVD graphene fabrication process for MEMS/NEMS sensors*. 2016, ISBN: 9781509019731. DOI: `10.1109/MEMSYS.2016.7421546`.

[46] N. Driscoll, R. E. Rosch, B. B. Murphy, *et al.*, “Multimodal in vivo recording using transparent graphene microelectrodes illuminates spatiotemporal seizure dynamics at the microscale,” *Communications Biology*, vol. 4, no. 1, 2021. DOI: `10.1038/s42003-021-01670-9`.

[47] B. Körbitzer, P. Krauß, S. Belle, J. J. Schneider, and C. Thielemann, “Electrochemical characterization of graphene microelectrodes for biological applications,” *ChemNanoMat*, vol. 5, no. 4, pp. 427–435, 2019. DOI: `10.1002/cnma.201800652`.

[48] J. Park, J. Bong, Y. H. Jung, *et al.*, “Design and fabrication of blue led-integrated graphene electrodes for neural stimulation and signal recording,” *ACS Applied Electronic Materials*, vol. 3, no. 10, pp. 4308–4316, 2021. DOI: `10.1021/acsaelm.1c00440`.

[49] H. Lyu, X. Liu, N. Rogers, V. Gilja, and D. Kuzum, “Graphene neural interfaces for artifact free optogenetics,” *2016 38th Annual International Conference of the IEEE Engineering in Medicine and Biology Society (EMBC)*, 2016. DOI: `10.1109/embc.2016.7591654`.

[50] P. Kshirsagar, S. Dickreuter, M. Mierzejewski, *et al.*, “Transparent graphene/pedot:pss microelectrodes for electro- and optophysiology,” *Advanced Materials Technologies*, vol. 4, no. 1, p. 1 800 318, 2018. DOI: `10.1002/admt.201800318`.

[51] N. V. Apollo, M. I. Maturana, W. Tong, *et al.*, “Soft, flexible freestanding neural stimulation and recording electrodes fabricated from reduced graphene oxide,” *Advanced Functional Materials*, vol. 25, no. 23, pp. 3551–3559, 2015. DOI: `10.1002/adfm.201500110`.

[52] Y. Lu, T. Li, X. Zhao, *et al.*, “Electrodeposited polypyrrole/carbon nanotubes composite films electrodes for neural interfaces,” *Biomaterials*, vol. 31, no. 19, pp. 5169–5181, 2010. DOI: `10.1016/j.biomaterials.2010.03.022`.

[53] S. Park, Y. J. Song, H. Boo, and T. D. Chung, “Nanoporous pt microelectrode for neural stimulation and recording: In vitro characterization,” *The Journal of Physical Chemistry C*, vol. 114, no. 19, pp. 8721–8726, 2010. DOI: `10.1021/jp911256h`.

[54] M. A. Gonzalez-Gonzalez, G. S. Bendale, K. Wang, G. G. Wallace, and M. Romero-Ortega, “Platinized graphene fiber electrodes uncover direct spleen-vagus communication,” *Communications Biology*, vol. 4, no. 1, 2021. DOI: `10.1038/s42003-021-02628-7`.

[55] M. Palmar, “Improving electrical characteristics of graphene neural electrode,” M.S. thesis, Delft University of Technology, 2021. [Online]. Available: `http://resolver.tudelft.nl/uuid:d9de4476-fcc1-4279-a4d5-cad1acd8d787`.

[56] L. Fritea, F. Banica, T. Costea, *et al.*, “Metal nanoparticles and carbon-based nanomaterials for improved performances of electrochemical (bio)sensors with biomedical applications,” *Materials*, vol. 14, no. 21, p. 6319, 2021. DOI: `10.3390/ma14216319`.

[57] C. Boehler, T. Stieglitz, and M. Asplund, “Nanostructured platinum grass enables superior impedance reduction for neural microelectrodes,” *Biomaterials*, vol. 67, pp. 346–353, 2015. DOI: `10.1016/j.biomaterials.2015.07.036`.

[58] E. P. Lee, Z. Peng, D. M. Cate, H. Yang, C. T. Campbell, and Y. Xia, “Growing pt nanowires as a densely packed array on metal gauze,” *Journal of the American Chemical Society*, vol. 129, no. 35, pp. 10 634–10 635, 2007. DOI: `10.1021/ja074312e`.

[59] S. D. Angelov, S. Koenen, J. Jakobi, *et al.*, “Electrophoretic deposition of ligand-free platinum nanoparticles on neural electrodes affects their impedance in vitro and in vivo with no negative effect on reactive gliosis,” *Journal of Nanobiotechnology*, vol. 14, no. 1, 2016. DOI: `10.1186/s12951-015-0154-9`.

[60] S. Koenen, C. Rehbock, H. E. Heissler, *et al.*, “Optimizing in vitro impedance and physico-chemical properties of neural electrodes by electrophoretic deposition of pt nanoparticles,” *ChemPhysChem*, vol. 18, no. 9, pp. 1108–1117, 2017. DOI: `10.1002/cphc.201601180`.

[61] A. Schmidt-Ott, M. F. Boeije, G. Biskos, *et al.*, “Nanoparticle production by spark ablation: Principle, configurations, and basic steps toward application,” in *Spark ablation: Building blocks for nanotechnology*. Jenny Stanford Publishing, 2020, pp. 50–57.

[62] F. M. Sapountzi, M. Lavorenti, W. Vrijburg, *et al.*, "Spark ablation for the fabrication of pem water electrolysis catalyst-coated membranes," *Catalysts*, vol. 12, no. 11, p. 1343, Nov. 2022, ISSN: 2073-4344. DOI: `10.3390/catal12111343`. [Online]. Available: `http://dx.doi.org/10.3390/catal12111343`.

[63] M. Palmar, "Flexible graphene-based passive and active spinal cord implants," M.S. thesis, Delft University of Technology, 2019. [Online]. Available: `http://resolver.tudelft.nl/uuid:13f3c500-4edd-4cf3-80ea-a4464279a78e`.

[64] A. Orlando, F. Franceschini, C. Muscas, *et al.*, "A comprehensive review on raman spectroscopy applications," *Chemosensors*, vol. 9, no. 9, p. 262, Sep. 2021. DOI: `10.3390/chemosensors9090262`. [Online]. Available: `http://dx.doi.org/10.3390/chemosensors9090262`.

[65] J. W. Tay, *Otsu's Method*. YouTube, Sep. 2020. [Online]. Available: `https://www.youtube.com/watch?v=jUUkMaNuHP8&t=177s`.

[66] *Graythresh global image threshold using otsu's method*. [Online]. Available: `https://nl.mathworks.com/help/images/ref/graythresh.html`.

[67] R. Pezone, G. Baglioni, P. M. Sarro, P. G. Steeneken, and S. Vollebregt, "Sensitive transfer-free wafer-scale graphene microphones," *ACS Applied Materials Interfaces*, vol. 14, no. 18, pp. 21 705–21 712, Apr. 2022. DOI: `10.1021/acsami.2c03305`. [Online]. Available: `http://dx.doi.org/10.1021/acsami.2c03305`.

[68] Z. Zhang and R. Wang, "Editorial for the special issue: "advanced nanomaterials for electrochemical energy conversion and storage"," *Nanomaterials*, vol. 12, no. 20, p. 3579, Oct. 2022. DOI: `10.3390/nano12203579`. [Online]. Available: `http://dx.doi.org/10.3390/nano12203579`.

[69] E. Hudak, "Electrochemical evaluation of platinum and diamond electrodes for neural stimulation," Ph.D. dissertation, May 2011.

[70] M. Golda-Cepa, K. Engvall, M. Hakkarainen, and A. Kotarba, "Recent progress on parylene c polymer for biomedical applications: A review," *Progress in Organic Coatings*, vol. 140, p. 105 493, Mar. 2020. DOI: `10.1016/j.porgcoat.2019.105493`. [Online]. Available: `http://dx.doi.org/10.1016/j.porgcoat.2019.105493`.